

MINISTRY OF NATIONAL EDUCATION



# THE ANNALS OF “DUNAREA DE JOS” UNIVERSITY OF GALATI

Fascicle IX  
**METALLURGY AND MATERIALS SCIENCE**

YEAR XXXI (XXXVI),  
September 2013, no. 3

ISSN 1453-083X



2013  
GALATI UNIVERSITY PRESS

## **EDITORIAL BOARD**

### **EDITOR-IN-CHIEF**

**Prof. Marian BORDEI** - "Dunarea de Jos" University of Galati, Romania

### **EXECUTIVE EDITOR**

**PhD. Marius BODOR** - "Dunarea de Jos" University of Galati, Romania

### **PRESIDENT OF HONOUR**

**Prof. Nicolae CANANAU** - "Dunarea de Jos" University of Galati, Romania

### **SCIENTIFIC ADVISORY COMMITTEE**

**Lecturer Stefan BALTA** - "Dunarea de Jos" University of Galati, Romania

**Prof. Lidia BENEÄ** - "Dunarea de Jos" University of Galati, Romania

**Acad. Prof. Ion BOSTAN** - Technical University of Moldova, Moldova Republic

**Prof. Bart Van der BRUGGEN** - Katholieke Universiteit Leuven, Belgium

**Prof. Francisco Manuel BRAZ FERNANDES** - New University of Lisbon Caparica, Portugal

**Acad. Prof. Valeriu CANTSER** - Academy of Moldova Republic, Moldova Republic

**Prof. Anisoara CIOCAN** - "Dunarea de Jos" University of Galati, Romania

**Lecturer Alina CIUBOTARIU** - "Dunarea de Jos" University of Galati, Romania

**Prof. Alexandru CHIRIAC** - "Dunarea de Jos" University of Galati, Romania

**Assoc. Prof. Stela CONSTANTINESCU** - "Dunarea de Jos" University of Galati, Romania

**Assoc. Prof. Viorel DRAGAN** - "Dunarea de Jos" University of Galati, Romania

**Prof. Valeriu DULGHERU** - Technical University of Moldova, Moldova Republic

**Prof. Jean Bernard GUILLOT** - École Centrale Paris, France

**Assoc. Prof. Gheorghe GURAU** - "Dunarea de Jos" University of Galati, Romania

**Prof. Iulian IONITA** - "Gheorghe Asachi" Technical University Iasi, Romania

**Prof. Philippe MARCUS** - École Nationale Supérieure de Chimie de Paris, France

**Prof. Vasile MARINA** - Technical University of Moldova, Moldova Republic

**Prof. Rodrigo MARTINS** - NOVA University of Lisbon, Portugal

**Prof. Strul MOISA** - Ben Gurion University of the Negev, Israel

**Prof. Daniel MUNTEANU** - Transilvania University of Brasov, Romania

**Prof. Viorel MUNTEANU** - "Dunarea de Jos" University of Galati, Romania

**Prof. Viorica MUSAT** - "Dunarea de Jos" University of Galati, Romania

**Prof. Maria NICOLAE** - Politehnica University Bucuresti, Romania

**Prof. Petre Stelian NITA** - "Dunarea de Jos" University of Galati, Romania

**Prof. Florentina POTECASU** - "Dunarea de Jos" University of Galati, Romania

**Assoc. Prof. Octavian POTECASU** - "Dunarea de Jos" University of Galati, Romania

**Prof. Cristian PREDESCU** - Politehnica University Bucuresti, Romania

**Prof. Iulian RIPOSAN** - Politehnica University Bucuresti, Romania

**Prof. Antonio de SAJA** - University of Valladolid, Spain

**Prof. Wolfgang SAND** - Duisburg-Essen University Duisburg Germany

**Prof. Ion SANDU** - "Al. I. Cuza" University of Iasi, Romania

**Prof. Georgios SAVAIDIS** - Aristotle University of Thessaloniki, Greece

**Prof. Elisabeta VASILESCU** - "Dunarea de Jos" University of Galati, Romania

**Prof. Ioan VIDA-SIMITI** - Technical University of Cluj Napoca, Romania

**Prof. Mircea Horia TIHEREAN** - Transilvania University of Brasov, Romania

**Assoc. Prof. Petrica VIZUREANU** - "Gheorghe Asachi" Technical University Iasi, Romania

**Prof. Maria VLAD** - "Dunarea de Jos" University of Galati, Romania

**Prof. François WENGER** - École Centrale Paris, France



## Table of Content

<b>1. Mariana (BUȘILĂ) IBĂNESCU, Viorica MUȘAT, Torsten TEXTOR, Boris MAHLTIG</b> - Photocatalytical Activities of Manganese Doped Zinc Oxide Nanoparticles Prepared by Sol-Gel Method.....	5
<b>2. Anisoara CIOCAN, Beatrice TUDOR</b> - Recycling of Integrated Steel Plant Solid Wastes in the Sintering Process and Corresponding Effects on Pollutant Emissions.....	9
<b>3. Adinel GAVRUS, Henri FRANCILLETTE, Duc Thien PHAM</b> - A Two-Step Inverse Analysis Approach Used to Identify the Mechanical Properties of Metallic Materials Subjected to Large Plastic Strains. Applications to Local Investigations of Surface Layer's Behaviour.....	14
<b>4. Liviu Cătălin ȘOLEA, Romică CREȚU</b> - Studies on the Effects of Olive Oil Oxidation.....	21
<b>5. Petre Stelian NITA</b> - Premises in the Design of Computational Algorithms for Refining Slags Applied in Ladle Treatment of Steels. Influence of BOF Slag and of Other Sources of Slag.....	27
<b>6. Tamara RADU, Maria VLAD, Viorel DRAGAN, Vasile BASLIU, Gina Genoveva ISTRATE</b> - Occupational Risk Management in Industry.....	34
<b>7. Mihaela MARIN, Florentina POTECAȘU, Octavian POTECAȘU</b> - Researches Regarding the Influence of Steam Oxidation on Sintered Alloys Properties.....	39
<b>8. D. C. VLADU, C. GHEORGHIES, M. BERCEA, I. STOICA, M. C. POPESCU, B. BITA, M. BORDEI</b> - Influence of Substrate Temperature on Structural and Morphological Properties of SnO <sub>2</sub> Nanostructured Thin Films.....	44
<b>9. Stela CONSTANTINESCU, Lucica ORAC</b> - Characterization of Sintered Hardmetals Coated with TiC.....	50
<b>10. Lavinia Marilena HARCEA, Iulian RIPOSAN</b> - Structure Characterization of Ca/Ba, Ca-FeSi Inoculated, Low Sulphur, Electric Melted, Thin Wall Grey Iron Castings...	55
<b>11. Gina ISTRATE, Florentina POTECAȘU, Vasile BAȘLIU</b> - Corrosion Behavior of Some Materials in 0.5M Ammonium Hydroxide Solution.....	62
<b>12. Marian BORDEI, Stefan DRAGOMIR, Viorel DRAGAN</b> - The Management of Work Risk for a Plate Rolling Mill Machine.....	68
<b>13. Marian-Iulian NEACSU, Elisabeta VASILESCU, Doru HANGANU</b> - Thermomechanical Process Simulation to Predict Processing of Mechanical Properties of Alloys Al-Zn-Mg-Cu.....	73
<b>14. Alina CIUBOTARIU, Lidia BENEĂ, Pierre PONTTHIAUX</b> - Effect of Mean Diameter Size of Disperse Phase on Morphology and Corrosion Resistance of Phenol – Formaldehyde Resin/Zn Coatings.....	78
<b>15. Viorel DRAGAN, Stefan DRAGOMIR, Marian BORDEI</b> - Measures to Optimize Job Security "Crane Machinists to Transport Liquid Steel".....	84





## PHOTOCATALYTICAL ACTIVITIES OF MANGANESE DOPED ZINC OXIDE NANOPARTICLES PREPARED BY SOL-GEL METHOD

Mariana (BUȘILĂ) IBĂNESCU<sup>1</sup>, \*Viorica MUȘAT<sup>1</sup>,  
Torsten TEXTOR<sup>2</sup>, Boris MAHLTIG<sup>3</sup>

<sup>1</sup>Centre of Nanostructures and Functional Materials-CNMF, "Dunărea de Jos" University of Galați,  
111, Domnească Street, 800201, Galați, Romania

<sup>2</sup>Deutsches Textilforschungszentrum Nord-West GmbH, DTNW GmbH, Adlerstr. 1, 47798 Krefeld, Germany  
and CENIDE, Center for Nanointegration Duisburg-Essen

<sup>3</sup>University of Applied Sciences, Faculty of Textile and Clothing Technology, Webschulstr,  
31, 41065 Mönchengladbach, Germany

\*Corresponding author: viorica.musat@ugal.ro.

### ABSTRACT

*In the last period, ZnO and doped ZnO nanoparticles are intensively investigated for their photocatalytic properties. This paper reports on ZnO and Mn-doped ZnO nanoparticles obtained by modified sol-gel method. Were studied the structural and optical properties by using x-ray diffraction (XRD) data and visible absorption spectra.*

*The photocatalytic activity of nanoparticles was investigated based on the degradation of the Methylene Blue (MB) dye solution. The results showed that Mn doping enhanced the photocatalytic activity of ZnO nanoparticles.*

KEYWORDS: ZnO nanoparticles, Mn doping, band gap, photocatalysis

### 1. Introduction

Since the decomposition of water into hydrogen and oxygen on titanium electrode by Fujishima and Honda in 1972, photocatalysis has been established as an efficient process for the mineralization of toxic organic compounds, hazardous inorganic constituents [1] and bacteria disinfection [2] owing to the strong oxidizing agent, i.e., hydroxyl radical (OH•) [3]. Most of these semiconductor photocatalysts have band gap in the ultraviolet (UV) region, i.e., equivalent to or larger than 3.2eV ( $\lambda = 387\text{nm}$ ). Therefore, they promote photocatalysis upon illumination with UV radiation. Unfortunately solar spectrum consists only of 5–7% of UV light, while 46% and 47% of the spectrum has visible light and infrared radiation, respectively [4]. This minimal extent of UV light in the solar spectrum has particularly ruled out the use of natural source of light for photocatalytic decomposition of organic and inorganic contaminants and bacteria disinfection from water and air on large scale. Surface and volumetric charge recombination is an additional obstacle that hinders heterogeneous photocatalysis to be an efficient purification method

[5]. ZnO has emerged to be a more efficient catalyst as far as water detoxification is concerned because it generates H<sub>2</sub>O<sub>2</sub> more efficiently [6], it has high reaction and mineralization rates [7]. Also it has more numbers of active sites with high surface reactivity [8]. ZnO has been demonstrated as an improved photocatalyst as compared to commercialized TiO<sub>2</sub> based on the larger initial rates of activities [9] and its absorption efficacy of solar radiations [10]. However, ZnO has almost the same band gap (3.2eV) as TiO<sub>2</sub>. Surface area and surface defects play an important role in the photocatalytic activities of metal oxide. The reason is that, doping of metal oxide with metal and/or transition metals increases the surface defects [11]. In addition it affects the optical and electronic properties [12] and can presumably shift the optical absorption towards the visible region. To improve the photocatalytic activities was doped ZnO with manganese ion (Mn<sup>2+</sup>) and were carried out studies on photocatalytic activities of Mn-doped ZnO using only UV light as source of radiation and methylene blue as test contaminant. The preliminary results presented in this work show much promise and suggest the need to further explore heterogeneous photocatalysis.

## 2. Experimental details

### 2.1 Preparation of undoped ZnO and Mn-doped ZnO (Mn<sup>2+</sup>:ZnO)

The preparation procedure was basically similar to that of Spanhel [13]. The procedure consists of two major steps. Firstly the suspension of the precursor and secondly the hydrolysis of the precursor to form the zinc oxide nanoparticles. Zinc acetate dihydrate (ZnAc)<sub>2</sub> • 2H<sub>2</sub>O (99%-Sigma Aldrich), manganese (II) sulfate monohydrate (MnSO<sub>4</sub> • xH<sub>2</sub>O-0.1; 5; 15 at%,) (99%-Sigma Aldrich, and isopropanol (99,8%-Fluka), were used to prepare the precursor before lithium hydroxide (LiOH-Merk) was used to hydrolyze the precursor.

For synthesizing the catalyst, 0.035M of (ZnAc)<sub>2</sub> • 2H<sub>2</sub>O in 500 ml 2-propanol was mixed with different concentrations of manganese (II) sulfate by reflux heating 82°C (boiling point) for three hours. Lithium hydroxide dissolved in isopropanol at room temperature was used for nanoparticle precipitation. The ZnO sol was stored at ≤ 4°C for 24 hours.

For separating Mn-doped ZnO nanoparticles, high-speed centrifugation 4000 rpm/20min was used, followed by several washes and drying.

### 2.2 Characterization of Nanoparticles

The crystal structures of the product were identified by X-ray diffraction patterns DRON-3 diffractometer system (Burevestnik, USSR) with CoK $\alpha$  radiation,  $\lambda = 1.789 \text{ \AA}$ .

The crystallite size of the particles was calculated with Debye-Scherrer formula:

$$D = \frac{0.94 \cdot \lambda}{\beta \cos \theta} \quad (1)$$

The value of interplanar distance ( $d$ ) was calculated with Bragg's equation:

$$2d \sin \theta = n \cdot \lambda \quad (2)$$

and lattice parameters:

$$\frac{1}{d^2} = \frac{4(h^2 + h \cdot k + k^2)}{3a^2} + \frac{l^2}{c^2} \quad (3)$$

The calculation is based on the measurement of full-width at half-maximum (FWHM) values in the corresponding XRD pattern.

The morphology and the composition of the product were examined by scanning electron microscopy (SEM, type Hitachi S 3400N with tungsten cathode, coated with gold Emitech K500X sputter coater, Oxford X-Max SDD X-ray Energy Dispersive Spectrometer (EDS)

Band gap energy value for ZnO nanoparticles was calculated with formula [14]:

$$E = h \cdot \frac{c}{\lambda} \quad (4)$$

UV/Vis Absorption measurements for that material are being carried out using a Cary 5E UV-VIS-NIR Spectrophotometer, Varian Deutschland GmbH with integrating sphere.

### 2.3 Photocatalytic measurements

Photocatalytic properties of the samples were investigated by measuring the UV absorption at room temperature using a Cary 5E UV-VIS-NIR Spectrophotometer. The photocatalytic activities of doped and undoped samples were evaluated by measuring photodegradation of Methylene Blue (MB) (20 mg/L added to 40 mL in water) in presence the 0.1g powder of Mn (0.1, 5, 15wt%):ZnO nanoparticles, in Petri dish, under ultraviolet illumination (>251nm) for 1hour.

## 3. Results and discussions

Crystalline structure of the prepared nanoparticles was characterized by the XRD (Figure 1). The peaks at  $2\theta = 37.52^\circ, 40.44^\circ, 42.77^\circ$  were assigned to (100), (002), (101), of ZnO planes, indicating the wurtzite structure. No characteristic peaks of manganese metal or manganese oxides phases were observed in fig 1, indicating that the samples are single crystalline phase.

Using the Debye-Scherrer equation and the halfwidth of the XRD lines, the average values of crystalline size of the samples were calculated based on the (101) crystal plane.

The crystalline phases and the structural parameters as main crystallite size ( $D$ ),  $a$  and  $c$  lattice parameters obtained by quantitative analysis of the XRD patterns shown in Figure 1 are presented in Table 1.

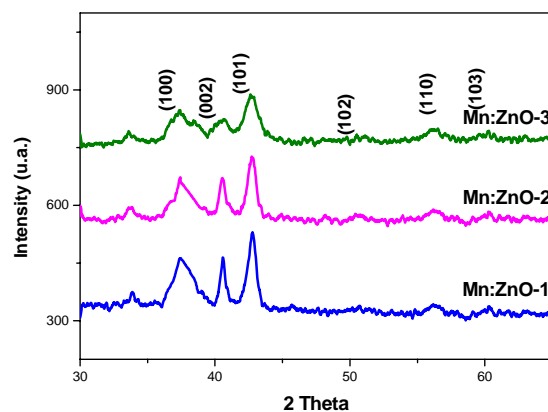


**Fig. 1.** XRD patterns for and Mn:ZnO nanoparticles with different concentration: a). Mn:ZnO-1; b) Mn: ZnO-2; c) Mn:ZnO-3

The crystalline size of photocatalyst decreased with increasing percentage of Mn doping ZnO nanoparticles.

**Table 1.** XRD structural parameters for different concentration of Mn doped ZnO nanoparticles

Sample	Mn	D	c	a
	[at%]	[nm]	[Å]	
Mn:ZnO-1	0.1	12.9	5,21002	3,24992
Mn:ZnO-2	5	11.8	5,20936	3,25007
Mn:ZnO-3	15	4.2	5,21008	3,25036

For the calculation of the band gap was used optic absorption spectrum. When a semiconductor absorbs photons of energy larger than the gap of the semiconductor, an electron is transferred from the valence band to the conduction band, an abrupt increase in the absorbency of the material occurs to the wavelength corresponding to the band gap energy. The UV-vis optical absorption spectra of as-prepared Mn:ZnO nanoparticles are presented in Fig. 3. The optical absorption edge presents a blueshift to the region of higher photon energy, when Mn concentration increases.

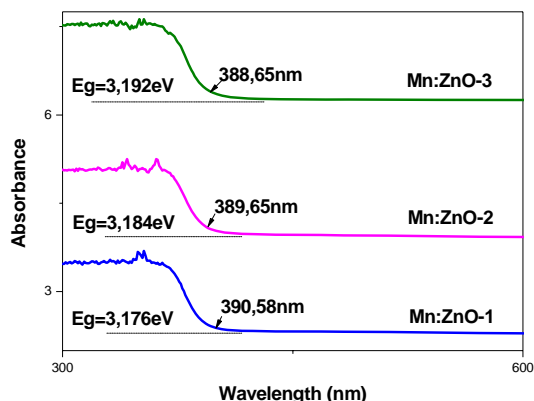


**Fig. 3.** UV-VIS Absorption spectra of Mn:ZnO nanoparticles

These blueshifts confirm preventing the recombination of photoexcited electrons and holes induced by Mn-acceptor doping and so the increase in carrier concentration. The values of optical band gap (Eg) show a widening up to 3.192eV with respect to the values of 3.137eV obtained for ZnO nanoparticles when the Mn – doping concentration increases up to 15at%. In general, according to Burstein–Moss effect, the blueshift of the absorption onset is associated with the increase of the carrier concentration blocking the lowest states in the conduction band [15]. The photocatalytic properties were studied using different concentration of Mn doped ZnO nanoparticles on degradation of methylen blue (MB). The extent of photocatalytic degradation was determined by the reduction in absorbance of the solution. As a result of the reaction between ZnO nanoparticles (through the reactive oxygen species on its surface) and MB dye,

the rate of decolorization was changed as was increased the dopant concentration of ZnO nanoparticles.

UV-vis absorption spectra of the residual blached solution of methylen blue after 60 min UV-irradiation in normal laboratory environment in presence of Mn (different concentration):ZnO as-prepared nanoparticles are shown in Fig.4.

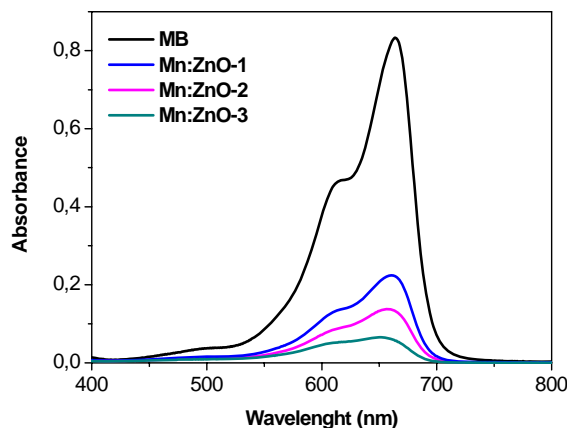


**Fig. 4.** UV-Vis absorption spectra of methylen blue in presence by different concentration of Mn doped ZnO nanoparticles (powder) after UV-irradiation, 1h in normal laboratory environment

Here, was assumed that upon illumination with UV light, Mn:ZnO generates electron–hole pair at the tail states of conduction band and valence band, respectively. The generated electron transfers to the adsorbed MB molecule on the particle surface because it is a cationic dye. The excited electron from the photocatalyst conduction band enters the molecular structure of MB and disrupts its conjugated system which then leads to the complete decomposition of MB. The hole at the valence band generates OH• via reaction with water or OH<sup>-</sup>, might be used for oxidation of other organic compounds. This clearly demonstrates that ZnO doped with manganese (Mn:ZnO) can be used as a potential photocatalyst, which can operate at visible light and it is evident that doping of ZnO with transition metals like Mn enhances photocatalytic activities of ZnO, and hence Mn:ZnO is capable of degrading MB and other organic dyes even with the UV light irradiation. [16].

#### 4. Conclusions

Mn:ZnO nanoparticles were prepared using a sol-gel process at a temperature below 90°C. Mn:ZnO nanoparticles sol has long stability for further processing.



The XRD measurement confirms that all, Mn-doped ZnO, nanoparticles consist of Wurtzite-type nanocrystallites with different crystalline orientation, (101) being the dominating peak. The Mn atoms substitute Zn sites in the lattice without changing the wurtzite structure. No secondary phases were observed.

The photocatalytic activity of Mn-doped ZnO nanoparticles showed decolorization of a Methylene Blue (MB) solution UV light, as a result of the reaction between the reactive oxygen species from the surface of ZnO nanoparticles and MB dye. The rate of decolorization changed when the Mn:ZnO nanoparticles sample changed. Higher Mn - doping concentration, lower intensity of absorption in visible region, are due to higher photocatalytic activities.

### Acknowledgements

The work of Mariana (Busila) Ibanescu was supported by Project SOP HRD – TOP ACADEMIC 78622.

### References

- [1]. J.M. Herrmann - *Heterogeneous photocatalysis: fundamentals and applications to the removal of various types of aqueous pollutants*, J. Catal. Today 53 (1999) 115–129.
- [2]. P.C. Maness, S. Smolinski, D.M. Blake, Z. Huang, E.J. Wolfrum, W.A. Jacoby - *Bactericidal activity of photocatalytic TiO<sub>2</sub> reaction: toward an understanding of its killing mechanism*, Appl. Environ. Microbiol. 65 (1999) 4094–4098.
- [3]. Z. Huang, P.C. Maness, D. Blake, E.J. Wolfrum, S.L. Smolinski, W.A. Jacoby - *Bactericidal mode of titanium dioxide photocatalysis?* J. Photochem. Photobiol. A 130 (2000) 163–172.
- [4]. T. Bak, J. Nowotny, M. Rekas, C.C. Sorrell - *Photo-electrochemical hydrogen generation from water using solar energy*. Materials-related aspects, Int. J. Hydrogen Energy 27 (2002) 1022–27991.
- [5]. X.Z. Li, F.B. Li - *Study of Au/Au<sup>3+</sup>-TiO<sub>2</sub> photocatalysts toward visible photo-oxidation for water and wastewater treatment*, J. Environ. Sci. Technol. 35 (2001) 2381–2387.
- [6]. E.R. Carraway, A.J. Hoffman, M. Hoffmann - *Environ. Sci. Technol.* 28 (1994) 786–793.
- [7]. I. Poullos, D. Makri, X. Prohaska - *Photocatalytic treatment of olive milling waste water, oxidation of protocatechuic acid, global nest*, Int. J. 1 (1999) 55–62.
- [8]. B. Pall, M. Sharon - *Enhanced photocatalytic activity of highly porous ZnO thin films prepared by sol-gel process*, Mater. Chem. Phys. 76 (2002) 82–87.
- [9]. K.Y. Jung, Y.C. Kang, S.B. Park - *Photodegradation of trichloroethylene using nanometre-sized ZnO particles prepared by spray pyrolysis*, J. Mater. Sci. Lett. 16 (1997) 1848–1849.
- [10]. S. Sakthivel, B. Neppolian, M.V. Shankar, B. Arabindoo, M. Palanichamy, V. Murugesan - *Solar Energy Solar Cells* 77 (2003) 65–82.
- [11]. R. Wang, J.H. Xin, Y. Yang, H. Liu, L. Xu, J. Hu - *The characteristics and photocatalytic activities of silver-doped ZnO nanocrystallites*, Appl. Surf. Sci. 227 (2004) 312–317.
- [12]. K. Vanhesuden, W. L. Warren, J. A. Voigt, C. H. Seager, D.R. Tallant - *Impact of Pb doping on the optical and electronic properties of ZnO powders*, Appl. Phys. Lett. 67 (1995) 1280–1282.
- [13]. Spanhel, L., Anderson, M. A. - *J. Am. Chem. Soc.* 1991, 113, 2826
- [14]. \*\*\* - Jayant Dharma-PerkinElmer Technical Center; Aniruddha Pisa-Global Application Laboratory PerkinElmer, Inc. Shelton, CT USA, *Simple Method of Measuring the Band Gap Energy Value of TiO<sub>2</sub> in the Powder Form using a UV/Vis/NIR Spectrometer*.
- [15]. X. Zi-Qiang, D. Hong, L. Yan, C. Hang - *Al-doping effects on structure, electrical and optical properties of c-axis-orientated ZnO:Al thin films*, Materials Science in Semiconductor Processing 9 (2006) 132–135.
- [16]. Ullah R., Dutta J. - *Photocatalytic degradation of organic dyes with manganese-doped ZnO nanoparticles*, Journal of Hazardous Materials 156 (2008) 194–200

## RECYCLING OF INTEGRATED STEEL PLANT SOLID WASTES IN THE SINTERING PROCESS AND CORRESPONDING EFFECTS ON POLLUTANT EMISSIONS

**Anisoara CIOCAN, Beatrice TUDOR**

"Dunărea de Jos" University of Galati, Faculty of Materials Engineering and Environment,  
111, Domnească Street, RO-800201, Galati, Romania  
email: aciocan@ugal.ro

### ABSTRACT

*The new practices in sintering technology allows for the use of a wide range of iron-containing materials in charge with obtaining the agglomerate with necessary characteristics for optimal operation of the blast furnace. The essential modifications in the composition of feed materials have an important impact on the nature and the quantity of pollutant emissions from the sintering plant. In this paper is presented an analysis of emissions and of their mechanism formation for the case of the sintering sector from an integrated steel mills, which transformed into agglomerate a variety of materials as iron ore fines, dust collected from blast furnace, ore concentrates and some fractions of metallurgical slag. These are correlated with operation conditions in sinter strand and of other main sections of the process.*

**KEYWORDS:** sinter plant, recycling, metallurgical wastes, pollutant emissions

### 1. Introduction

In ferrous metallurgy sintering is the thermal preparing process that permits the conversion of fine

particles of iron ores under the action of heat into a material suitable for use in blast furnace (Figure 1).

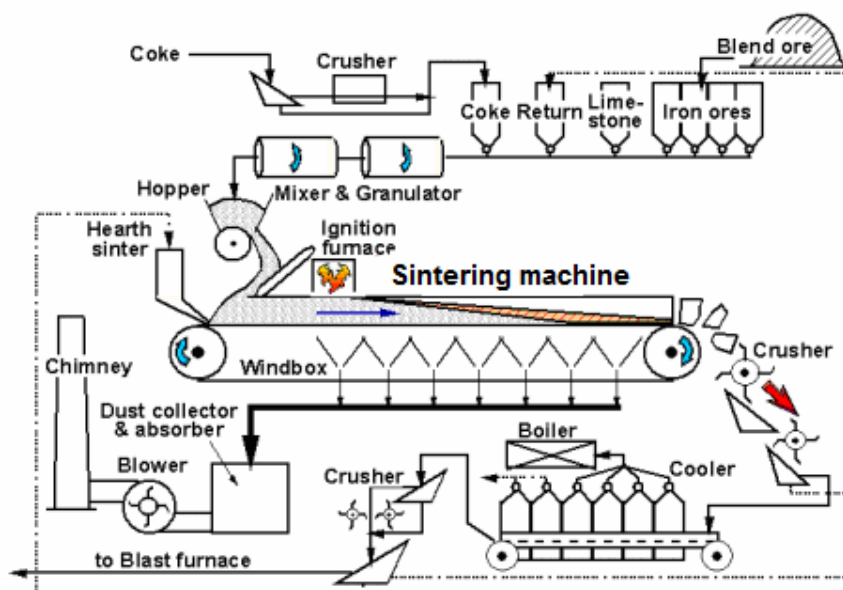


**Fig. 1.** Flow sheet of sintering process on Dwight-Lloyd type of sintering machine [1]



The process is usually carried out by suction of air necessary for solid fuel combustion through a layer composed by a material mixture placed on a sinter band. In the classical sinter plants, iron ore fines, solid fuels (coke fines or coal fine), fine limestone/dolomite are used to compose the feed inputs. Today, in accordance with the new environmental practice for integrated steel mills was developed the sintering technology that allows for the introduction in the charge materials of the various iron-bearing wastes generated in different production steps of iron and steel manufacturing work. Many sinter plants in the world are capable to recycle the wastes up to the extent of 180 - 200 kg/ts [2, 3].

The recycling and utilization of metallurgical wastes (such as oxide dusts, sludge, scales, slag etc.) have as main advantage the reducing of primary raw materials consumption and the recurrent costs of mining/and beneficiation and preserve the environment. Also, the recycling of iron-bearing wastes eliminates their disposal costs, limits the amount of landfilled wastes and their environmental impact.

These materials, as powder or particles with small sizes, are problematic at recycling for their high content of harmful constituents. Are even used only normal feeds that do not contain steel plant wastes, the conventional sintering process is considered as the major source of pollutants within an integrated steel plant.

The sinter plant produces large quantities of pollutant emissions into air. The literature mentions the pollutants: sulphur oxides, nitrogen oxides, carbon monoxide, fluorides dust, heavy metals, alkali-chlorides, hydrocarbons, polychlorinated dibenzo-p-dioxins and furans, polychlorinated bipheyls, organohalogen compounds, polycyclic aromatic hydrocarbons, cooling particulates [4]. At recycling of metallurgical wastes is favoured the generation of emissions and the inadequate operating conditions lead to increasing of their quantity. The recycling the valuable units with reduction of pollutant emissions is one of the most important challenges that require the improving of the operating of sinter plant.

The paper aims at assessing the impact of recycling of integrated steel plant solid wastes on the sintering process and corresponding pollutant emissions.

## 2. Solid wastes recycled in the sintering process

In the case of sinter plant analysed the raw materials inputs are typically composed from various sorts of iron ore fines, ore concentrates and undersize sinter returned from process after crushing and

screening [5]. Also a variety of recycled process materials in form of small or very small particles are introduced in the materials charge. These are wastes mainly consisting of iron scale from the rolling mills, a wide variety of dusts or sludge separated from waste gas treatment devices, and some fractions rich in iron sorted from metallurgical slag. Thus sinter plants work as a „waste to value” converting unit. The recycling capacity of iron-bearing wastes is determined by their properties (both its chemical composition and its state). The knowledge of their characteristics in accordance with iron ores that are usually used in the feed inputs of sinter plant is imposed. Their recycling makes necessary the change of process parameters and has an influence on the sinter quality and especially on pollutant emissions.

**Blast furnace dust and sludge** result from air pollution control equipments, dust from dry BOF gas treatment, respectively sludge from wet treatment. According to European Committee Blast Furnace Report, the chemical composition of dust from blast furnaces that operate with iron sinter varies within 38-42% Fe, 0.8-1.2% Mn, 10-12% CaO, 8-10% SiO<sub>2</sub> și 8-18% C. This is different for the blast furnaces with feeds composed of iron ores and pellets: 44-48% Fe, 0.6-1% Mn, 2-4% CaO, 12-14% SiO<sub>2</sub>, 8-18% C. Iron is present as gehlenite (Ca<sub>2</sub>Al<sub>2</sub>SiO<sub>7</sub>), magnetite, hematite, wüstite [6]. The recycling is conditioned by the content of Zn, Pb, and alkali. Significant is Zn concentration (mainly as ZnO·Fe<sub>2</sub>O<sub>3</sub>) in the BF dust. This is concentrated in fine fractions, where its content varies in the range of 0.01 - 0.5% as against with coarse fractions where the content is 1.4 - 3.4 %. Similar relation is kept for Pb content of the BOF dust (as PbO): 0.01 - 0.04% for fine fractions and 0.2-1.0% for coarse fractions [7]. In some cases the dust contains toxic elements (Cd, Cr and As) [6]. The BF dust has a higher content of K<sub>2</sub>O (~ 0.50%). The sulphur is major for BF dust, about 0.50%. It can be explained by its content of unburned coal particles that circumstantial pass nonburned through the stock column of material into blast furnace.

**BOF sludge** is composed of fine solid particles recovered by wet cleaning of the gas. The moisture content is appreciable (35 - 40%) and it is imposed to be dried before its recycling to the sinter plant. Solid particles from BOF sludge contain C, Fe as oxides, Ca, Mn, Mg, Al, Si, P, alkalis and heavy metals (especially Zn and Pb). The BOF sludge has a high zinc content ranging from 1.8% to 7.8%. The presence of iron is explained by its evaporation during the processes occurring in the converter. The zinc concentration increases in the case of large amounts of galvanized steel scrap used in feeds. Also other metals as Cd, Mn and Pb have origin into scraps recycled. Much of metals emitted from BOF are present in the particles retained in the cleaning

equipments (~ 73%) and a small amount of Zn, Pb associated with fine particles unfiltered is released into air [7, 8].

**Oil mill scale** has a grain size below 10mm. The iron content, mostly in oxide form, is about 70%. The oil content of rolling scale is typically in the range of 0.2 to 2%, but oil contents as high as 10% have been observed. The oil/grease that is bonded to mill scale is the major impediment to the direct recycling [7, 8].

**Scrap C** is selected from old slag that was historically stored in the dump of the integrated steel plant. Typically BOF slag has the basicity (lime/silica ratio) of 2.5 to 4.0 and higher FeO content approximately 25 to 35%. In this slag is often present the significant content of "free lime". Steelmaking slag is crushed and sized for charging to the sinter plant to utilize the iron and manganese units and also the fluxing compounds CaO, MgO [8].

### 3. Origin of pollutant emissions

Most important environmental issue associated with sinter manufacturing by using feed with participation of wastes is that of air emissions consisting of particulate matter and gaseous pollutants.

Sinter plants may generate the most significant quantity of **particulate matter** as emissions in an integrated steel mill.

The solid emissions as airborne particulate matter arise from materials-handling operations. These are greater at handling of very fine and very dry dusts. The crushing, raw material handling and transport, belt charging and discharging from the crusher and hot screens, involve the generation of considerable amounts of particulate matter. Important dust quantity is released from sintering band.

The grain size distribution of the PM from a sinter strand before reduction consists of two types: coarse PM (with a grain size about of 100  $\mu\text{m}$ ) and fine PM (0.1 - 1  $\mu\text{m}$ ) [9]. These include the fragments of the raw materials such as iron ores, limestone, and cokes are released from the sintering process and discharged in the gas. Unburned carbon and metallic chlorides are also contained in the dust particles. The main particulate emission sources are collected in the

gases of wind-boxes. Some of entrained particulate matter is released to air via the main stack, after passing through the particulate air pollution control equipment.

The fine particles used as raw materials in the sintering process in considerable amounts can lead to increasing of particulate emissions. These potential emissions are normally ducted to a separate dust removal system and discharged through a separate stack. Sometimes some particles may pass from the control system and are vented through the main stack. So the fugitive emissions could be released in air [10].

The air emissions are correlated with the nature of feeding materials and performance of waste gas cleaned solutions. The properties (composition, size, and morphology of particles) of fines and their quantity in the feed are important in the mixing operations (first stage of the sintering process). The mixture of materials is granulated by simultaneous balling and wetting of materials (iron ore fines, coke breeze, flux and wastes) into the mixing drum. The attaching and layering processes of finer particles (< 0.25 mm) onto the surface of coarser particles influence not only the permeability of sinter bed but also the amount of dusty particles entrained by gasses. The dust emitted from bed is formed in the drying/dehydration zone due to the materials and formation of fine particles by granules breakage at decrepitating. Largest amount appears due the extinction of adjacent particles in the combustion zone. Also, the combustion zone favours the formation of the alkali chloride (NaCl, KCl) due to the high temperatures [11]. The wet zone from the strand behaves like a temporary trap for the particles fluidized at upper zones.

Some part of trapped dust must re-stick to granules while the wet zone was drying. So, the wet zone acts as a wet gas scrubber, and therefore there is an accumulation of fine particles immediately downstream of the dry zone. At the same wind-box, the dust emission into exhaust started increasing as the gas temperature rose, and ceased before the maximum temperature appeared at the melting zone touching the bottom of the sintering bed (i.e., at "the burn through point") (Figure 2).

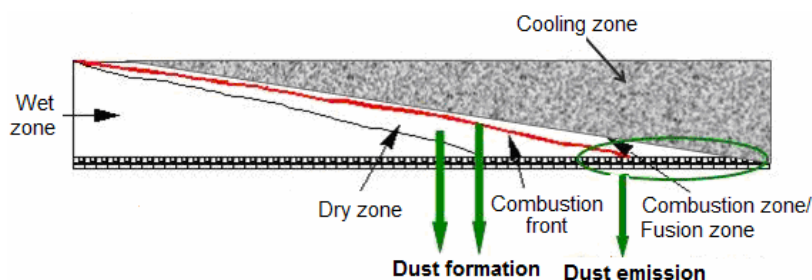


Fig. 2. Formation and releasing of dust emissions from sinter bed [5]

The parameters of the process affect the generation of pollutant emissions. The level of dust emissions is influenced by the moisture of the mixture subjected to agglomeration, the temperature of the gas and the basicity of the agglomerate. The increasing of coke content raises the temperature in the sintering bed and as result enhances the dust suppression. More coke, more particles fluidized at combustion zone. Also, the sintering machine operation (start-up/stopping) leads to the generation of dust.

**CO and CO<sub>2</sub> emissions** result from combustion of fine coke particles and of unburned carbon from BF dust. Also the reduction reactions of iron oxides at high temperature in sintering reaction zone is a source of CO. The combustion of coke begins between 700 and 800°C with hot air from the ignition process. Once the combustion is initiated, its front starts moving downward in the depth of materials bed. With increasing temperature, the CO<sub>2</sub> gas formed reacts with the carbon of coke to produce CO gas. The CO gas reduces hematite to produce magnetite. When further reduction occurs, wüstite is formed. The global rates of CO<sub>2</sub> formation were higher than those of CO formation. So the waste gas emitted at main stack of sinter plant contains more CO<sub>2</sub> (5 - 10%) [12]. The major part of **sulphur compounds emissions** is formed during the combustion of coke

breeze. Also minor participation has unburned coal particles from BF dust. After formation, just under combustion layer, SO<sub>2</sub> is recombined with CaO or water from wet zone. At advancing of the combustion layer through the sinter bed, the thickness of wet zone decreases and as result its capacity to retain small amounts of SO<sub>2</sub> is reduced. At the end of the sinter bed, the wet zone is saturated with SO<sub>2</sub>, and finally this is emitted into the gasses released just before the optimum burning point (Figure 3). The mill role scale present in the sintering charge behaves exothermally during sintering and has an effective contribution in reducing SO<sub>x</sub> emission.

Over 90% of „**nitrogen oxides**” or **NO<sub>x</sub> emissions** (consisting of NO and NO<sub>2</sub>) are originated from the combustion of fuel. The mineralogy of iron ore (the presence of goethite α-FeOOH) has effect on the emissions.

The combustion NO<sub>x</sub> formation starts right after ignition, in the combustion layer. These combustion products are no longer recombined. They are not retained in the wet zone, being released regularly during combustion process.

Due to the relatively low temperature of the combustion front of <1300 °C and low localized oxygen concentrations, thermal NO<sub>x</sub> is present in a less amount (about 10%) in the wastes gasses emitted from sinter bed (Figure 3) [3].

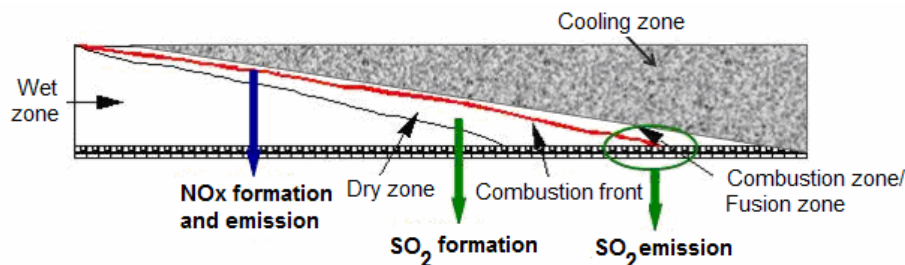


Fig. 3. Formation and emission of SO<sub>2</sub> and NO<sub>x</sub> [5]

**VOCs, hydrocarbons and polyaromatic hydrocarbons** are emitted from volatile hydrocarbons in the sinter feed. Coke breeze and oily mill scale are the main source of these emissions.

**Heavy metals emissions** have the origin into iron ores and some recycled wastes (dusts and sludge) subjected to the sintering process. The BOF sludge has a higher percentage of alkali Zn, Pd, Cd, Cu, Cr, Ni etc. During heating, the heavy metals (especially lead, zinc and tin) contained in these materials may be volatilized and may be adsorbed onto fine solid particles taken by gases emissions. Some fine particles are able to pass through the particulate air pollution control equipment and are emitted in the air. These may have a much higher content of these metals than the raw gas dust or the sinter mixture [2, 3]. Also, during the sintering process, lead reacts with chlorides to form very fine crystals of lead chlorides

which are able to pass through most electrostatic precipitators [10].

**Emissions of dioxins and furans.** Polychlorinated dibenzenoparadioxins (PCDDs) and polychlorinated dibenzenofurans (PCDFs) are formed by thermal and combustion processes in two different areas of sinter installation. Most of dioxins/furans are emitted in the sinter bed during combustion of solid fuel. Appreciatively 10% of the total PCDD/PCDFs are generated in the gas collectors via de novo synthesis [2, 3].

In the sinter bed, PCDD/PCDFs formation starts in the upper regions of the sinter bed shortly after ignition. Then the dioxin/furan and other compounds condense on cooler burden beneath as the sinter layer advances along the sinter strand towards the burn through point (just ahead of the flame front) (Figure 4).

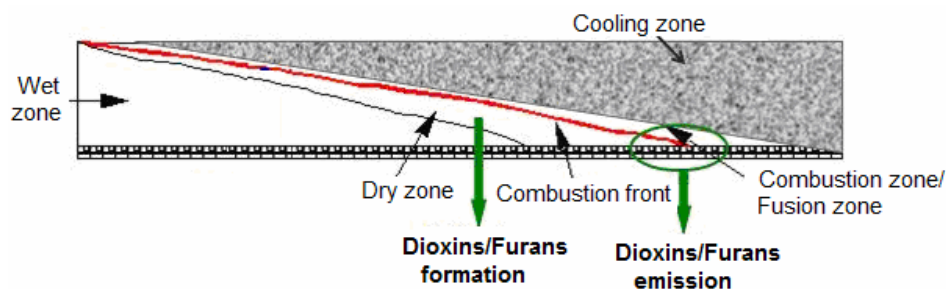


Fig. 4. Formation and emission of dioxins and furans [5]

Near the end of the sinter grate, in the sinter layer there are two temperature intervals favourable for dioxin formation. Though are viable (will be vaporized and emitted from sinter strand) only those formed in the bottom zone. The most likely those generated in the top zone are destroyed at crossing of layers with high temperatures [4].

A small fraction of PCDD/PCDFs is the result of the so-called "de novo" synthesis mechanism. This involves the presence of unburned carbon in the form of soot (and carbonaceous particles derived from hydrocarbon components, chlorine, metallic chlorides and some metals as catalyst [13].

The operating parameters of the sintering process and the composition of the feed mixture have impact on formation of PCDD/PCDFs. The nature of solid combustible and raw materials from sinter bed influences the emissions of chlorine/chlorides, carbon, precursors, metals catalysts, oils etc. Principally the unwanted compounds enter the sinter installation by means of the recycled wastes. Occasionally some components and fine granulation of recycled materials can cause operating unstable conditions for sinter process and as result the flame front propagation is disrupted.

#### 4. Conclusions

The sintering technology allows for the introduction in the charge materials of various iron-bearing wastes generated in different production steps of iron and steel manufacturing work. The recycling of iron-bearing wastes has important benefits: removing of disposal costs; limitation of the landfilled amount of wastes; diminishing of environmental impact for wastes dumped. On the other hand, the essential modifications in the composition of feed materials can have an important impact on the nature and the quantity of pollutant emissions (especially dust, sulphur compounds, heavy metals, dioxins and furans) from sinter plant. Although the flexibility of the sintering process permits recycling of a variety of internal wastes generated from integrated steel plant it is necessary to implement supplementary pollution prevention measures. The primary measures for preventing the

use of pollutant emissions refer to the following: the feed materials selection; the removal of the contaminants from the material in accordance with the specification of limits on permissible concentrations of unwanted substances; adequately mixing or blending of materials.

#### References

- [1]. S. V. Komarov, E. Kasai - *Simulation of sintering of iron ore bed with variable porosity*, Institute of Multidisciplinary Research for Advanced Materials Tohoku University, Phoenix User Conference, Melbourne, (2004), [http://www.cham.co.uk/puc/puc\\_melbourne/papers/Paper13\\_Komarov.pdf](http://www.cham.co.uk/puc/puc_melbourne/papers/Paper13_Komarov.pdf).
- [2]. \*\*\* - *Integrated pollution prevention and control. Draft reference document on best available techniques for the production of iron and steel*, draft February 2008, <http://eicppb.jrs.es>.
- [3]. R. Rainer, M. A. Aguado-Monsonet, S. Roudier, L. Delgado Sanch - *Best Available Techniques (BAT) Reference Document for Iron and Steel Production*. Industrial Emissions Directive 2010/75/EU (Integrated Pollution Prevention and Control), (2013), [http://eippcb.jrc.ec.europa.eu/reference/BREF/IS\\_Adopted\\_03\\_2012.pdf](http://eippcb.jrc.ec.europa.eu/reference/BREF/IS_Adopted_03_2012.pdf).
- [4]. \*\*\* - *Guidelines on Best Available Techniques (BAT) for Sinter Plants in the Iron Industry*, section V.D.2: Sinter Plants in the iron industry, [www.pops.int/.../draftguide/5d2ironsinteringdra](http://www.pops.int/.../draftguide/5d2ironsinteringdra).
- [5]. A. M. Ftodiev - *Emisii poluante survenite in timpul procesului de aglomerare al minereurilor de fier din ArcelorMittal Galati*, proiect GPPEP, (2013).
- [6]. B. Das, S. Prakash, P. S. R. Reddy, V. N. Misra - *An overview of utilization of slag and sludge from steel industries*, Resources, Conservation and Recycling, Volume 50, Issue 1, March (2007), pp. 40–57.
- [7]. \*\*\* <http://www.worldsteel.org/>.
- [8]. \*\*\* - *Iron Unit Recycling*, <http://www.metallpass.com/metaldoc/paper.aspx?docID=89>.
- [9]. \*\*\* - *EC BREF on the Production of Iron and Steel*, <http://www.epa.ie/pubs/advice/bref/Iron%20&%20Steel.pdf> (2001)
- [10]. N. R. Passant, M. Peirce, H. J. Rudd, D. W. Scott, I. Marlowe, J. D. Watterson - *UK Particulate and Heavy Metal Emissions from Industrial Processes*, A report produced for the Department for Environment, Food & Rural Affairs, the National Assembly for Wales, the Scottish Executive and the Department of the Environment in Northern Ireland, AEAT-6270 Issue 2, February (2002).
- [11]. M. Nakano, J. Okazaki - *Influence of Operational Conditions on Dust Emission from Sintering Bed*, ISIJ International, Vol. 47 (2007), No. 2, pp. 240–244.
- [12]. A. Ciocan, *Generarea și controlul emisiilor poluante industriale*, GUP Galati, (2013).
- [13]. N. Tsubouchi, S. Kuzuhara, E. Kasai, H. Hashimoto, Y. Ohtsuka - *Properties of Dust Particles Sampled from Windboxes of an Iron Ore Sintering Plant: Surface Structures of Unburned Carbon*, ISIJ International, Vol. 46 (2006), No. 7, pp. 1020–1026.



# A TWO-STEP INVERSE ANALYSIS APPROACH USED TO IDENTIFY THE MECHANICAL PROPERTIES OF METALLIC MATERIALS SUBJECTED TO LARGE PLASTIC STRAINS. APPLICATIONS TO LOCAL INVESTIGATIONS OF SURFACE LAYER'S BEHAVIOUR

**Adinel GAVRUS, Henri FRANCILLETTE, Duc Thien PHAM**

LGCGM - EA3913, ISCR/CM-UMR CNRS 6226, INSA Rennes, Université Européenne de Bretagne (UEB)  
20, Av des Buttes de Coesmes, F-35708 RENNES Cedex 7, France  
email: adinel.gavrus@insa-rennes.fr

## ABSTRACT

*The aim of this research work is to improve the experimental and numerical analysis of the local mechanical properties corresponding to metallic alloys used by bulk forming processes. A non-conventional upsetting test and an optimal direct extrusion device designed by the authors are used in order to identify the constitutive rheological equations and the friction models, starting directly from measured load-stroke curves. A two-step inverse analysis strategy is thus proposed starting from a complete Finite Element Model of the experimental tests and using a strong numerical coupling of the FEM with an optimization platform in charge with the automatic parameters identification. The obtained results are correlated with experimental investigations based on X-Ray, EBSD and hardness measurements concerning the microstructure and the local mechanical properties of the surface layer obtained from a conical extrusion process.*

**KEYWORDS:** inverse analysis, rheology & tribology, cold metal forming, surface layer properties

## 1. Introduction

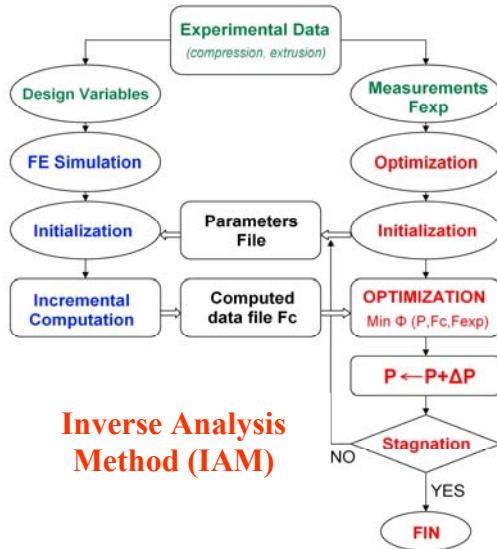
Today many manufacturing processes require improving the knowledge of the mechanical behaviour of material's surface layer, especially conditioned by the strong interaction between the global material rheology and the local tribological phenomena which occur at the tool-piece interfaces. The present work is then focused on the experimental and numerical analysis of the local mechanical properties corresponding to aluminium alloys used frequently by different bulk forming processes [1]. A non-conventional upsetting test [2] and an optimal direct extrusion device [3] have been developed in order to identify the constitutive rheological equations and the friction laws, starting directly from measured load-stroke curves. A two-step inverse analysis strategy is proposed starting from a complete Finite Element Model (FEM) of the experimental tests and using a strong numerical coupling of this FEM with an optimization platform in charge with the automatic parameters identification [4, 5]. All the mechanical complexity of the experimental friction test caused essentially by the non-linearity of the

large plastic deformations and of the local contact evolution, characterizing the tool-specimen interfaces, is taken into account by the numerical model [6]. The obtained macroscopic rheological and tribological behaviour is then used to analyse local microstructure and mechanical properties of the surface layer generated by a conical extrusion deformation [7].

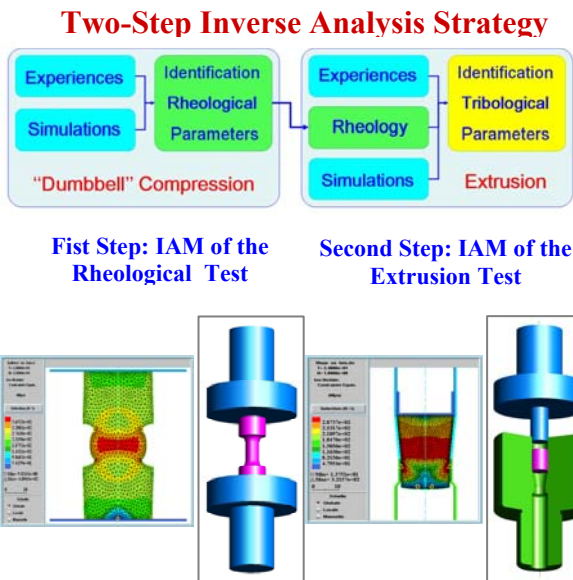
## 2. Mechanical properties identification using a Two-Step Inverse Analysis approach applied to an extrusion process

At a macroscopic and mesoscopic scale, to identify the rheological and the tribological properties of a material used during a bulk forming process requires to reproduce the same plastic deformation conditions via specific mechanical tests. During the forming process, the formation of new contact surfaces between the piece and the tool requires similar mechanical history able to describe the material behaviour corresponding to large plastic strains and for loadings close to the real ones. Recently the authors have been proposed an optimal

forward extrusion test [3, 7] with a geometric design defined by an input cylindrical zone (with a diameter  $D_i = 20$  mm and a length  $L_i = 40$  mm), an output cylindrical zone (with a diameter  $D_o = 17$  mm and a length  $L_o = 7$  mm) and a conical die (with an angle equal to  $5^\circ$ ).



a)



b)

**Fig. 1.** a) Principle of the Inverse Analysis Method (IAM) based on an optimal coupling between the Experiment and the Numerical Model, b) Two-Step Inverse Analysis Strategy applied to a sequential identification of the rheological and tribological properties

During the extrusion process it has been shown that this geometry permits to maximize the influence of the friction phenomena and consequently allows for the identification of the tribological properties. Starting from the research results obtained by Diot et al. [2], a dumbbell specimen upsetting test can be used to identify an elasto-plastic rheological behaviour. In this case the friction has no effect on the material deformation and the measured load-stroke curve depends only on the constitutive rheological law.

The main problem is that in all these cases it is impossible to realize an analytical computation of the stress-strain variation and the use of an inverse analysis technique seems to be compulsory [4]. Figure 1a presents the principle of the Inverse Analysis Method and its application for the both proposed experimental tests.

It is based on a strong coupling between the experimental results, the numerical model used for the simulation of the experiment and an optimization modulus in charge to find the optimal set of the unknown parameters  $P$  that minimizes a cost function  $\Phi(P, F^{exp}, F^c)$  expressed in terms of the measured  $F^{exp}$  and computed  $F^c$  loads using a least square formulation.

The minimization algorithm can be based on a zero order or a first order optimization technique. In this study is used a Gauss-Newton iterative method detailed by Gavrus in [4].

In Figure 1b is pictured the scheme of the two-step Inverse Analysis strategy applied to a sequential identification of mechanical behavior. In a first stage, a compression test of a dumbbell specimen is performed to study and identify by inverse analysis the rheological behaviour of the material. In a second time, using the previous computed rheological data, the automatic identification method is applied to the direct extrusion process in order to obtain adequate formulations of friction models and to compute more precisely the corresponding coefficients [7].

The numerical models used to simulate the experimental tests were built from the commercial FE software FORGE2®

### 3. Application to AA 5083 aluminium alloy

#### 3.1. Identification of rheological and tribological properties

For the AA 5083 aluminium alloy the rheological behaviour can be described by a Ludwick constitutive relationship:

$$\bar{\sigma} = \sigma_0 = \sigma_{00} + K\bar{\epsilon}^n \quad (1)$$

The inverse analysis using a FEM of the compression test leads to the plastic flow equation defined by:

$$\sigma_0 = 142 + 373.05\bar{\epsilon}^{0.306} \quad (2)$$

In the case of the extrusion process, the friction model defining the interface contact conditions must be defined by a Coulomb-Tresca criterion:

$$\tau_f = \text{Min}(\mu\sigma_n, \bar{m}\sigma_0/\sqrt{3}) \quad (3)$$

Starting from the previous identified rheological law, a second inverse analysis applied to the extrusion test estimates the friction coefficients such as:

$$\begin{cases} \mu_{input}^{cyl} = \mu_{output}^{cyl} = 0.24, \mu_{conic}^{cyl} = \infty \\ \bar{m}_{input}^{cyl} = \bar{m}_{output}^{cyl} = 1, \bar{m}_{conic}^{cyl} = 0.37 \end{cases} \quad (4)$$

or

$$\begin{cases} \mu_{input}^{cyl} = 0.30, \mu_{conic}^{cyl} = \infty, \mu_{output}^{cyl} = 0.16 \\ \bar{m}_{input}^{cyl} = \bar{m}_{output}^{cyl} = 1, \bar{m}_{conic}^{cyl} = 0.36 \end{cases} \quad (5)$$

The first friction model I.1 (Eq. (4)) assumes equal values for the Coulomb parameter in input and output cylindrical parts, where the mechanical contact is perfectly elastic, when for the conical die area, where important plastic deformations occur, a Tresca formulation is used. For the second model I.2 (Eq. (5)), different Coulomb coefficients are used to define the elastic contact in the cylindrical zones of the extrusion die.

In order to avoid the strong coupling existing between the friction parameter's influences on the input area, conical zone and the output one, a gap  $j$  equal to 0.15 mm has been chosen between the initial specimen and the extrusion die ( $j = (D_i - D_s)/2$ ).

The comparisons between the experimental load-stroke curve and those obtained from a finite element simulation (using the previous identified rheological and tribological parameters) are plotted in Fig. 2.

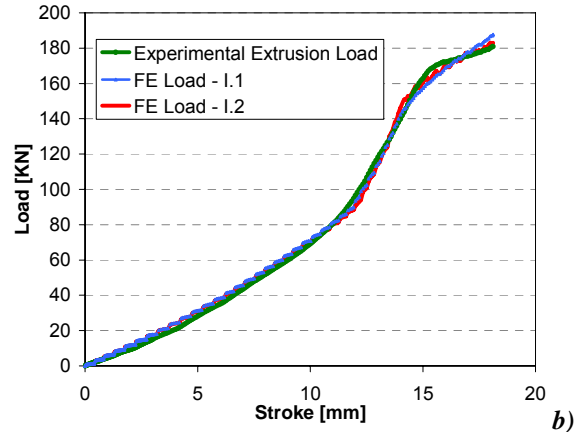
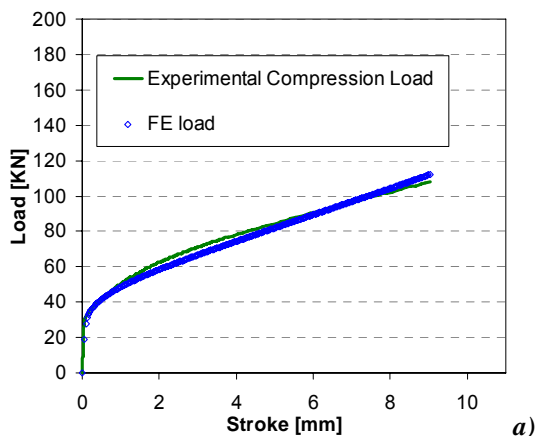


**Fig. 2.** Comparison between the experimental load-stroke curves and the FE ones using the previous identification results [3]: a) for the compression test (the load is independent with respect to the interfaces friction), b) for the direct extrusion test (realized for dry friction conditions)

A very good agreement is obtained for the both mechanical tests, pointing out that the friction model I.2 reproduces correctly the extrusion curve describing the load-stroke variation.

### 3.2. Numerical analysis

Using the identified rheological and tribological data corresponding to the AA5083 aluminum alloy (constitutive Eq. 2 and friction model I.2), a finite element simulation of the extrusion process has been analyzed in details. Figure 3 presents the distributions of the cumulated plastic strain and of the Von Mises stress corresponding to two different stages of the extrusion process.

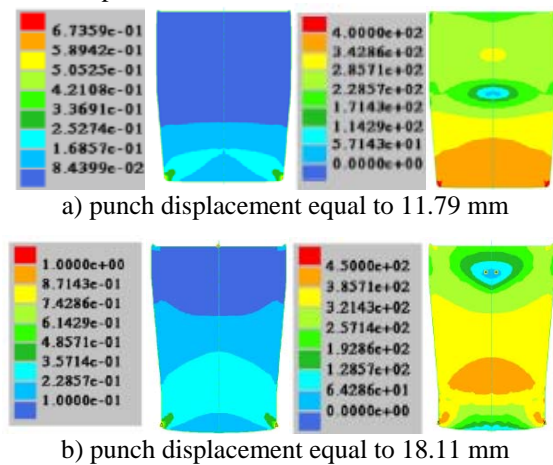


**Fig. 3.** Iso-values of the plastic strain (left pictures) and of the Von-Mises stress (right pictures) for two extrusion stages

These numerical results permit to understand the complex path of the specimen deformation history, the non homogeneity of the strains or stresses and especially to quantify the most important mesoscopic mechanical variables which characterize the new specimen surface formed during the plastic contact of the extruded material with the conical die.

#### 4. Analyses concerning the layer surface properties of an extruded AA5083 specimen

More numerical and experimental correlations can be obtained using data based on the investigations of the material by microstructure observations, by local hardness tests and by estimation of macroscopic shear stress variations on the layer surface [3]. A lot of samples have been prepared from the initial AA5083 specimen ( $D_s=19.7$  mm,  $L=25$  mm and  $Ra=0.8$   $\mu\text{m}$ ) and especially from the extruded ones according to Fig. 4.

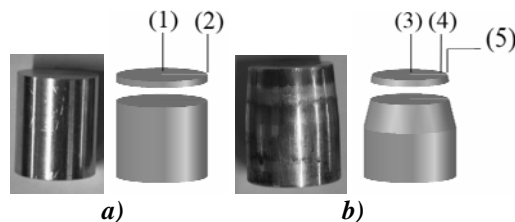


**Fig. 4.** Specimens and radial or axial cut samples (1, 3 – middle area, 2, 4, 5 – edge area) used for X-ray, EBSD measurements and hardness estimation for a) initial state, b) extruded state

This study proposes to analyse an extruded sample obtained from a punch displacement of 11.79 mm, having a final diameter  $D_{\text{extr}}$  equal to 17.6 mm (Fig. 4b). So it is possible to investigate the influence of the local plastic shear friction on the surface layer properties before the complete filling of the conical die.

##### 4.1. Experimental X-Ray analysis

From the X-Ray measurements of overall texture, it is possible to remark that for a plastic strain variation between 17% and 33%, the grain shape is not affected by the material deformation and the grains size is already uniform. The grains shape obtained after a deformation by extrusion is similar to that which was before deformation and the global texture of material obtained from X-Ray diffraction is similar after or before the extrusion process. Furthermore, near the edge of the extruded section, the grain shape is similar to the centre ones.

Concerning the grain size, this one is therefore not sensitive to the friction at the tool-specimen interface. The distribution of the grain size in the sample sections, before and after extrusion, is presented in Table 1.

**Table 1.** Grains size distributions in the cut specimen sections, before and after extrusion

Grain Size	Middle area		Edge area	
	Before	After	Before	After
[2.5 $\mu\text{m}$ , 9.5 $\mu\text{m}$ ]	-	-	58.8%	52.8%
> 10 $\mu\text{m}$	56.6%	66.2%	-	-

Firstly it is observed that for the centre area of cutting samples, most grains have a size larger than 10  $\mu\text{m}$ ; for the edge area the majority of grains have a size between 2.5  $\mu\text{m}$  and 9.5  $\mu\text{m}$ . On the other hand it can be seen that the change in grain size before and after extrusion is not important. In the centre of the initial sample, 56.6% of the grains have a size greater than 10  $\mu\text{m}$  and this value is 66.2% after deformation by extrusion. At the edge of the section, under the simultaneous effect of friction and plastic deformation, the grain size distribution varies only by 6% (from 52.8% to 58.8%). This variation is considered very low if are taken into account the measurement uncertainty and the non-homogeneity of the samples. Finally it is possible to conclude that during an extrusion process characterized by an average plastic deformation of 25% (defined by  $\bar{\epsilon} \approx 2\ln(D_i / D_{\text{extr}})$ ), the influence of the friction on the grain size is rather negligible.

##### 4.2. Experimental EBSD analysis

To obtain information concerning the grain orientation, an EBSD measuring system (Fig. 5) has been used.



**Fig. 5.** System EBSD - Microscope JSM-6400

The Figure 6 and Figure 7 show the obtained pole figures corresponding to the extruded specimen in the central both area (zone 3) and the edge one (Zone 5).

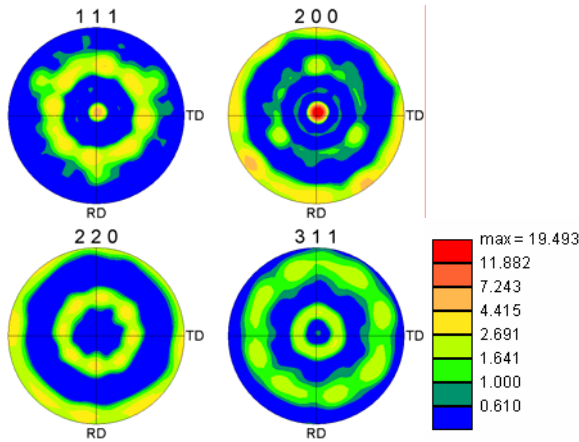


**Fig. 6.** Pole figures corresponding to the central area (zone 3) of the extruded specimen (EBSD measurements)

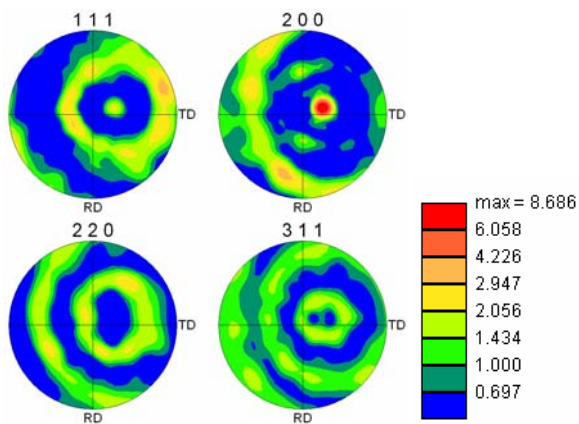


**Fig. 7.** Pole figures corresponding to the edge area (zone 5) of the extruded specimen (EBSD measurements)

Comparing zone 3 (central area of the specimen) and zone 5 (positioned at 100  $\mu\text{m}$  from the outside surface), the intensity distribution is generally asymmetric relative to the centre of the pole figures, but near the sample edge, the asymmetry is more pronounced.

These results are principally due to the specific state of the stress near the surface where the interface friction has a significant influence on the changes of the grain orientations.

Figure 8 pictures the grain orientations of the initial and extruded specimens obtained by EBSD.

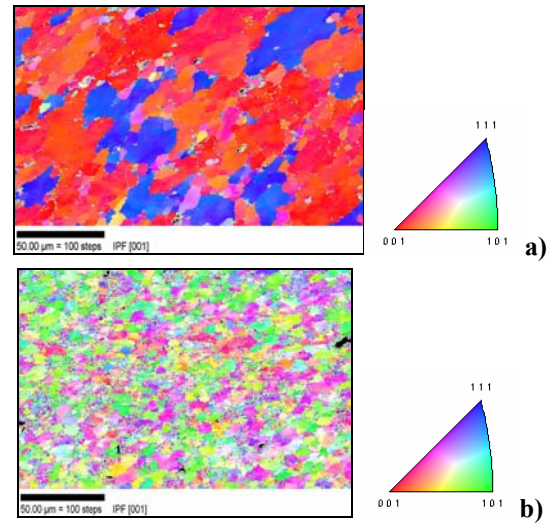


**Fig. 8.** Maps of grain orientations obtained by microscopic EBSD measurements of the extruded specimen [3]: a) for the middle area ( $r/R=0$ ), b) for the outside surface ( $r/R \approx 1$ )

#### 4.3. Experimental hardness analysis

Concerning the local mechanical properties of the layer surface, Vickers hardness measurements have been realized for the extruded specimen along a vertical section passing by a line through the point 3 (pictured in Fig. 4) and along the outside surface, named respectively measurement positions 3 and 5. Using the geometric coordinates of each measured point, the plastic strain values have been estimated from the numerical simulation of the extrusion process (Fig. 3a).

A non-linear regression permits to describe the variation of the hardness with the plastic strain using two relationships: a classical Ludwik formulation and a Voce one. Experimental variations and identifications results are plotted in Fig. 9.

It is possible to conclude that further the contact between the tool and the specimen, the hardness of the material occurs primarily as a result of plastic deformation and can be estimated by the following expression:  $HV = HV_0 + f(\bar{\epsilon})$ . On the other side at the specimen interface the evolution of the hardness is strongly influenced by friction and consequently this one must be correlated with the entire history of both local plastic deformation process and local plastic contact phenomena.

In a general way, starting from the theory of Tabor, for a material characterized by an elastoplastic hardening behaviour, the hardness value can be supposed to be proportional to the Von Mises stress.

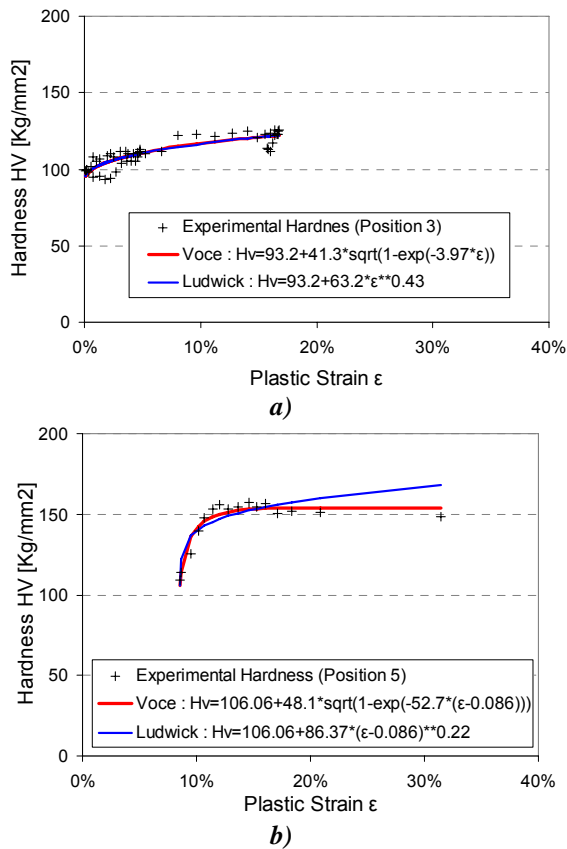


**Fig. 9.** Variation of the Vickers hardness with the plastic strain: a) cut sample from the extruded specimen (vertical cut in Position 3), b) outside surface of the extruded specimen (Position 5)

Thus concerning the initial hardness value this one can be computed from the formulae  $HV_0 = \gamma\sigma_0$  (both terms expressed in kg/mm<sup>2</sup>), where  $\gamma$  is an empirical coefficient, generally equal to 3.0 for a large class of metallic materials, if the equivalent stress  $\sigma_0$  is evaluated for a representative plastic strain value around 0.08 (8%). Thus, for the analysed AA 5083 aluminium alloy, using the rheological law identified from the dumbbell compression test, the initial value of the hardness must be approximately equal to 94.3 kg/mm<sup>2</sup>. This value is close to those given at the beginning of the hardness curves ( $HV_0 \in [90 \text{ kg/mm}^2, 106 \text{ kg/mm}^2]$ ), values which permit to valid the experimental recordings and all the previous comments.

## 5. Discussions

The previous EBSD and hardness experiments have been shown, beside the shape and the grain size distribution, the important changes of the

microstructure morphology and of the local mechanical properties around the layer surface corresponding to the conical die-piece interface. These changes can be explained by the important effect of plastic friction phenomenon at this interface.

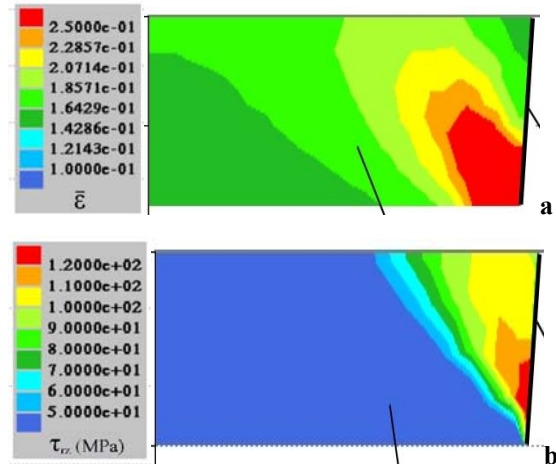


**Fig. 10.** Finite Element simulation of the conical extrusion process (simulation using the friction model I.2 with  $\mu_i = 0.3$ ,  $\bar{m}_c = 0.36$  and  $\mu_f = 0.16$ ) :

- a) Iso-Values of the equivalent plastic strain  $\bar{\epsilon}$ ,  
b) Iso-Values of the shear stress  $\tau_{rz}$

Using finite element simulations obtained from the commercial software FORGE2®, numerical results concerning the maps of the equivalent plastic strain and of the shear stress in the extruded specimen, especially inside the conical part of the tool, are shown in Fig. 10.

When there is no friction between the specimen and the die it is found that the plastic deformation of the material is almost constant over the entire section of the specimen. However, when friction at the contact interface between the tool and the sample is important, increasing plastic deformation values are located rather close to the contact zone (zone 5).

The plastic deformation in this zone is about three times larger than that of the centre of the section (zone 3) and can have locally values up to 40%. Therefore the friction at the interface has a great influence on the evolution of the deformation in the layer near the outside surface of the test material. Concerning the shear stress a similar phenomenon is observed: the shear stress in the area near the edge surface is much larger than that at the centre of the specimen. So a rapid change of stress values can be observed in the contact area. This considerable shear gradient is consistent with the microstructure changes in this area especially for the grain orientations and also for the evolution of the hardness.



## 6. Conclusions

A new approach has been developed by the authors to investigate rheological and tribological properties of metallic materials undergoing large plastic deformations during a bulk forming process. The experimental and numerical investigations of a forward extrusion confirm that during the deformation the specimen is in contact with the outgoing part of the die by a new surface generated in the conical part by the material plastic flow. In this zone, the layer surface has different microscopic and local mechanical properties than the initial one. Furthermore the analysed results confirm also the difference of the Coulomb coefficients values defining the input zone (Di) and the output area (Do) corresponding to a perfect elastic contact. Numerical values of plastic strain and shear stress corresponding to the material layer surface have been correlated with the EBSD and hardness measurements. The results emphasize the need to develop multi-scale approaches in order to obtain quantitative predictions of observed microstructure evolutions, in particular for the grain morphology principally defined by the size and spatial orientations.

## References

- [1]. **B. Avitzur** - *Metal Forming: Processes and Analysis*, McGraw-Hill, New-York, 1968.
- [2]. **S. Diot, D. Guines, A. Gavrus, E. Ragneau** - *Minimization of Friction Influence on the Evaluation of Rheological Parameters from Compression Test: Application to a Forging Steel Behavior Identification*, J. of Eng. Mat. and Tech., 131, n<sup>o</sup>1 (2009), 10 pages.
- [3]. **A. Gavrus, H. Francillette, D. Thien Pham** - *An optimal forward extrusion device proposed for numerical and experimental analysis of materials tribological properties corresponding to bulk forming processes*, Tribology International, 47 (2012) pp. 105-121.
- [4]. **A. Gavrus** - *Identification automatique des paramètres rhéologiques par analyse inverse (Automatic identification of rheological parameters by inverse analysis)*, PhD Thesis, ENSMP, Paris, France, 1996.
- [5]. **B. Boyer** - *Méthode inverse et calcul de sensibilité semi-analytique: application à l'identification de paramètres rhéologiques et tribologiques au cours des procédés de mise en forme*, PhD thesis, ENSMP, Paris, France, 2001.
- [6]. **Q. Zhang, M. Arentoft, S. Bruschi, L. Dubar, E. Felder** - *Measurement of friction in a cold extrusion operation: study by numerical simulation of four friction tests*, Proc. of the Esaform Conf. on Metal Forming, P. Boisse et al. (Eds), Lyon, 2008, pp. 57-60.
- [7]. **D. Thien PHAM** - *Conception optimale d'un test d'extrusion directe pour l'investigation et l'identification par analyse inverse des propriétés tribologiques des matériaux métalliques utilisés dans le forgeage volumique à froid*, PhD Thesis, INSA Rennes, France, 2011.



## STUDIES ON THE EFFECTS OF OLIVE OIL OXIDATION

**Liviu Cătălin ȘOLEA, Romică CREȚU**

"Dunărea de Jos" University of Galați, Department of Machine Elements & Graphics,  
111, Domnească Street, 800201, Galați, Romania  
email: liviu.solea@yahoo.com

### ABSTRACT

*The aim of this study is the viscosity's evolution depending on the temperature and the shear rate and the analysis of the transmittance spectra of the oxidized olive oil. Oxidation of olive oil is a process that leads to the degradation of the sensorial qualities (color) and generates compounds such as peroxides and aldehydes. Studies performed in order to determine olive oil transmittance have shown that this method can be successfully used for the analysis of vegetable oils oxidation, oils that are going to be used as lubricants in food industry. Olive oil oxidation becomes more obvious by determination of trichromatic parameters. Thus it has been proved that by using this method, conclusive results regarding olive oil oxidation are obtained.*

KEYWORDS: viscosity, transmittance, oxidation, olive oil

### 1. Introduction

Recently, lubricants based on vegetable oil which are biodegradable are bit by bit reducing the field application of mineral oil. Biodegradable lubricants will be used more as they are less damageable and toxic to the environment. This will be an important factor in the agriculture and food industry where there are possibilities of lubricant leakage [1].

A high percentage of at least 65% of 16 to 22 carbon fatty acids is required in order for the base oil to provide adequate lubrication. Longer chain fatty acid sources are preferred to provide longevity to the oil. Preferred sources of long chain fatty acids are from members of Cruciferae family, Compositae family and Leguminosae family. Common oilseeds in these families are: canola, rapeseed, crambe, sunflower, safflower, flax, and soybean. Other sources of the base oil include cotton, corn, olive, peanut and other common oils. Each base oil has unique functionality and lubricant formulations will vary depending upon base oil used, [2].

Vegetal oil oxidation is initiated by formation of free radicals. Free radicals can easily be formed from the removal of a hydrogen atom from the methylene group next to a double bond. Free radicals rapidly react with oxygen to form a peroxy radical. The peroxy radical can then attack another lipid molecule to remove a hydrogen atom to form a hydroperoxide and another free radical, propagating the oxidation

process. The vegetable oil autooxidation mechanism presented here is a simplification of a complex series of reactions. The process is further complicated by variations in conditions, such as ultraviolet rays, temperature, pressure and oxygen availability, or by the presence of other compounds, such as antioxidants, chelating agents and metals. Metals, for example, act as a catalyst for the oxidation of vegetable oils speeding up degradation and the production of free radicals [3].

### 2. Experimental Details

The olive oil that was tested here had been purchased from a local store. This oil, according to the information provided by the analysis performed within Expur Slobozia labs, presents this composition: 12.6% palmitic acid (C16:0), 79.3% oleic acid (C18:1), 4.7% linoleic acid (C18:2), 0.8% linolenic acid (C18:3), 0.4% arachidic acid (C20:0), 1.2% palmitoleic acid (C16:1) and very little percentage of heptadecanoic acid (C17:0), behenic acid (C22:0) and erucic acid (C22:1), as well. Transmittance spectrum determination was performed using a T60 spectrophotometer, produced by PG Instruments Limited (C.E.), the determinations were performed for the range of 300-1100nm. In order to reach a forced oxidation process, the equipment in Figure 1 was used. That is composed of 1-air pump, 2-air flowmeter, 3- air filter, 4-oil sample tube, 5-thermostatic bath. For every test oxidation 25 ml of

oil were used. The flow rate of air introduced into the oil sample was 20 L/h.



**Fig. 1.** Oxidation equipment

Also, the samples were measured for colour in the  $x$ ,  $y$ ,  $z$  or  $L^*$ ,  $a^*$ ,  $b^*$  and  $C^*$ ,  $h_{ab}$  coordinates (CIE XYZ, CIE  $L^*a^*b^*$  and CIE  $C_{ab}^*h_{ab}$  colour systems). CIE  $L^*a^*b^*$  scale is recommended by the Commission Internationale de l'Eclairage (CIE), where  $b^*$  measures the yellowness when it is positive, the grayness when zero, and the blueness when negative. In this colour space  $L^*$  represents the lightness. Illumination was performed by  $C/2^\circ$  (standard illuminant defined by CIE).

Chroma values denote the saturation or purity of colour. Hue angle values (expressed in grade) represent the degree of redness, yellowness, greenness and blueness [4].

Dominant wavelength,  $\lambda_d$  was determined as described according to CIE indications [5], [6]. Forced oxidation behavior research of the oxidized and non-oxidized rapeseed oils give us qualitative and quantitative estimations regarding their efficiency in use as lubricants. Trichromatic values are obtained according to Tristimulus Colorimetry method, in the case of oils by determination of the transmittance according to the relations:

$$\begin{aligned} X &= 0.21 \cdot T_{445} + 0.35 \cdot T_{550} + 0.42 \cdot T_{625} \\ Y &= 0.17 \cdot T_{445} + 0.63 \cdot T_{550} + 0.20 \cdot T_{625} \\ Z &= 0.94 \cdot T_{445} + 0.24 \cdot T_{495} \end{aligned}$$

where  $T$  is the transmittance measured by the spectrophotometer, when  $\lambda$  is 445, 495, 550 and 625nm [7], [8].

### 3. Experimental Results

Oxidizing the olive oil at a temperature of 100°C for 5 hours and 10 hours, no changes in shape of the transmittance spectrum were shown. Thus, for evidence of changes in the transmittance spectrum of olive oil shape, this oil was oxidized for 5 hours or 10 hours at 110°C and 130°C (Figure 2 and 3). The shape of spectrum for non-oxidized olive oil is

similar to that presented by other authors in the specific literature [9] for other varieties of olive oil.

In Figure 2 and 3 it is noted that the spectra shapes of olive oxidized oil at 100°C for 5 or 10 hours, weren't changed too much compared to reference oil.

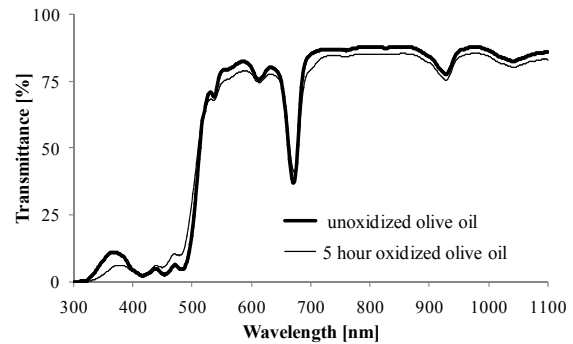


**Fig. 2.** Transmittances of unoxidized and oxidized olive oils for 5 hour at a temperature of 110°C

By comparing the absorption spectra of olive oil while oxidation, there are highlighted its hypochromic displacements between 450nm and 470nm respectively up to 662nm and hypochromic displacements to 520nm and 640nm.

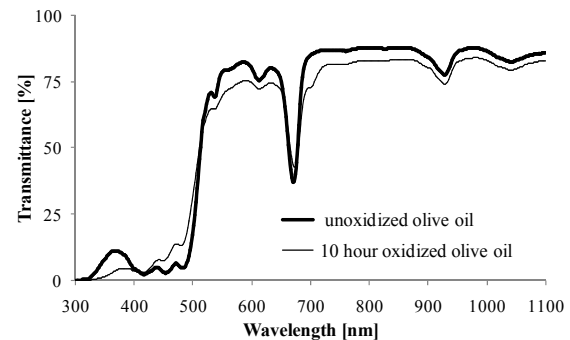


**Fig. 3.** Transmittances of unoxidized and oxidized olive oils for 10 hours at a temperature (1) of 110°C

It was also performed the study of olive behaviour during oxidation, regarding the evolution of chromatic parameters at variations of oxidation temperature, using different color systems.

Thus, in Tables 1 and 2 there are shown the experimental results related to olive oil oxidation at the temperature of 110°C for different oxidation periods of time. Olive oil color parameters, shown in these tables are given by  $X$ ,  $Y$ ,  $Z$  tristimulus values or by  $x$ ,  $y$ ,  $z$  trichromatic coordinates.

Trichromatic measurements are highlighting a decrease of luminosity by 2.65% comparing to unoxidized olive oil ( $\Delta L^* = -2.272$  at 110°C). On the

other hand, vegetable oils also have their own aromatic systems which make the particular being eventually present even after tough treatments. Meanwhile it is to be taken into account that color intensity varies similarly to the variation of luminosity. It is also noted that this color variation of 110°C oxidized olive oil is sustained by the hue angle too, presenting a more restricted value range.

Increasing the oxidation temperature from 110°C to 130°C, important changes of transmittance occur, for olive oils that were oxidized for 5 or 10 hours (Fig.4 and 5).

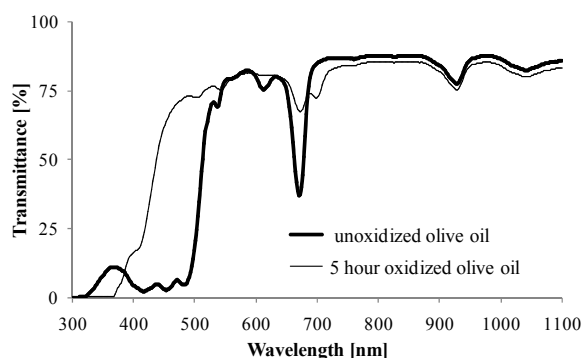


**Fig. 4.** Transmittances of unoxidized and oxidized olive oils for 5 hour at a temperature of 130°C

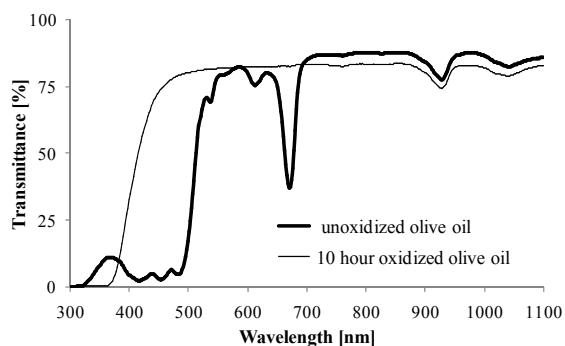


**Fig. 5.** Transmittances of unoxidized and oxidized olive oils for 10 hour at a temperature of 130°C

It is noted the oxidized oil spectra displacement to ultraviolet range. At the same time it is revealed an important decrease, even the disappearing of initial spectrum peaks corresponding to unoxidized olive oil, after an oxidation period of time of 5 or 10 hours, at 130°C temperature. As a result of oxidation, the peaks related to the presence of carotenoids and those related to chlorophyll as well disappear, due to the destruction of the pigments responsible for the color of oil.

Table 3 presents trichromatic compounds and coordinates, respectively the dominant wavelengths

determined by the latter, for 130°C oxidized olive oil. It is noted that oxidation process leads to displacements of the dominant wavelength, which is decreasing with oxidation time, from 575nm to 559.5nm. The experimental data also show a close connection between chromatic parameters as the luminosity, displacement from red to yellow, chroma and tonality angle and oxidation temperature/time.

In the case of 130°C oxidation too, the yellow rate and chroma are the parameters which prevail for a comparative evaluation of olive oil behaviour (Table 4). After a period of time of 10 hour oxidation it is noted a slight increase (about 8%) of luminosity, which is in accordance with the information that other authors have previously shown [9].

At the same time, color differences that were presented in Table 5 are corresponding to the information provided by the measured parameters.

According to the data presented in Table 5 it is highlighted that the luminosity of 110°C oxidized oil for 5 or 10 hours, is decreasing. This aspect is the result of the minus sign of the luminosity value differences. Meanwhile, the luminosity of 130°C oxidized oil for 5 or 10 hours, is increasing. This aspect is the result of the positive values of the luminosity differences values.

The same variations are noticed regarding other important trichromatic parameters differences, as the yellow grade or chroma. It should be specified that these variations occur, in addition for the case of olive oil oxidized at 130°C. In the case of the latter we can notice that after a maximum period of time of oxidation, under the experimental conditions, the difference of the yellow grade is wider compared to that obtained in the case of 110°C oxidized oil. This is due to the destruction of the most of the chromophores present in the original oil.

Color differences expressed by  $L^*$ ,  $b^*$  and  $C_{ab}^*$  parameters are also supported by the hue angle  $h_{ab}$ . The values for  $h_{ab}$  differences for oxidized oil at 110°C and the oxidized oil at 130°C as well, after 5 and 10 hour oxidation time period, are positive in all cases. This result shows that the position of olive oil color being subject of this experiment is moving within the same quadrant in chromatic circle, counter clockwise, towards the hues of yellow green. This occurs due to the fact that during forced oxidation hydroperoxides are formed too because of the composition of olive oil containing just a little quantity of polyunsaturated acids (the quantity of linolenic acid is 0.8% while the studied olive oil contains 4.7% linoleic acid).

The color difference is very important considering the cumulated contribution of chromatic parameters. In this context, the data in Table 5 show large and even very large differences in the color of olive oil that occur during its oxidation, expressed by

parameter  $\Delta E^*_{ab}$  ( $\Delta E^*_{ab} > 10$ ). According to enshrined data in literature and industrial practice [5], [10], the values of the color differences are used for chromatic significance interpretation. It is accepted in standards that if  $\Delta E^*_{ab} < 0.2$  then the difference of color is not perceivable; by visualisation it is hardly noticed if  $0.2 < \Delta E^*_{ab} < 0.5$ , but it becomes perceivable if  $\Delta E^*_{ab} = 0.5 - 1.5$ , and easily to be observed when  $\Delta E^*_{ab} = 1.5 - 3.0$ . In literature [10] it is mentioned that the differences of color when  $\Delta E^* < 10$  are considered slight differences, and the color difference for  $\Delta E^* > 10$  are considered big differences.

In Figure 6 and 7, the variations of viscosity with shear rate are represented, for olive oils oxidized at 120 and 130°C, testing temperature being 30°C.

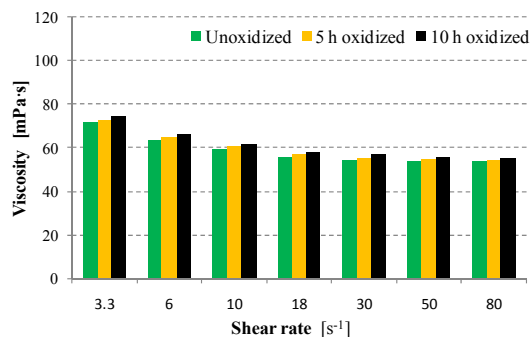


**Fig.6.** Variation of viscosity with shear rate, for the unoxidized and oxidized olive oil at the temperature of 120°C

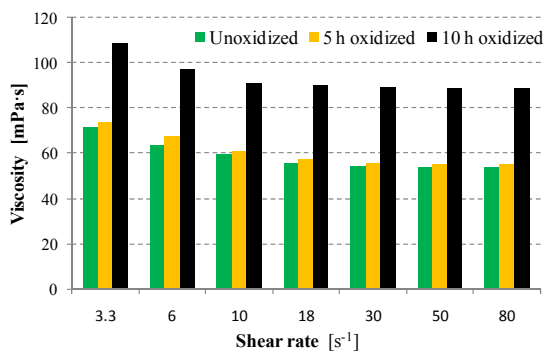


**Fig.7.** Variation of viscosity with shear rate, for the unoxidized and oxidized olive oil at the temperature of 130°C

Viscosity decreases with shear rate increase but this decrease is sharper when the values of the shear rate are in the range of 3.3 to 18 s<sup>-1</sup>. Viscosity increases with oxidation temperature increase and the increase of oxidation period of time, important increases are observed in the case of oil that was oxidized for 10 hours at a temperature of 130°C.

In Figure 8 and 9 there are represented the variations of the viscosity with the temperature for olive oil that was oxidized at 120 and 130°C, and the

variation of viscosity depending on the temperature for non-oxidized olive oil as well, at a shear rate of 3.3 s<sup>-1</sup>. Viscosity is decreasing when temperature is increasing, the same situation for both oxidation temperatures. It is noted a slight increase of the olive oil viscosity when oxidized at a temperature of 120°C for 5 hours and 10 hours compared to non-oxidized olive oil.

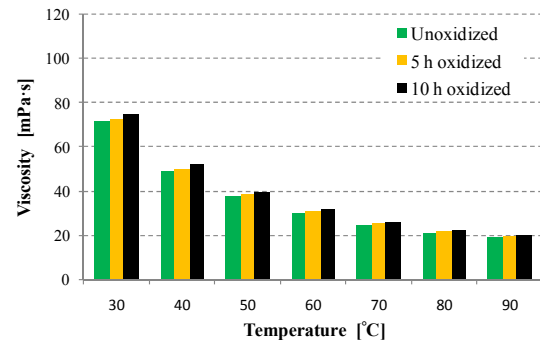


**Fig. 8.** Variation of viscosity with temperature, for the unoxidized and oxidized olive oil at the temperature of 120°C

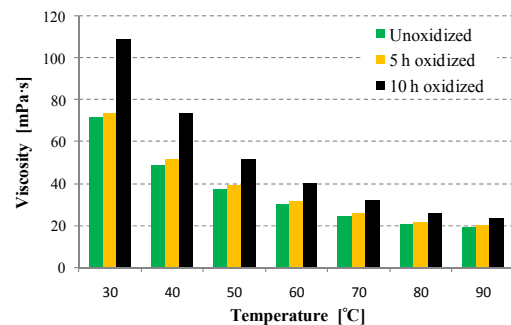


**Fig. 9.** Variation of viscosity with temperature, for the unoxidized and oxidized olive oil at the temperature of 130°C

When oxidation temperature is increasing one can notice a sharp increase of the viscosity for olive oil that was oxidized for 10 hours. Analyzing viscosity increases corresponding to the 10 hour oxidation period of time, at a testing temperature of 30°C, the viscosity of the oxidized olive oil increases by 51.51% compared to the viscosity of non-oxidized olive oil. At a 60°C testing temperature, the viscosity increase is 32.35% and at a temperature of 90°C the viscosity increased by 22.36%.

These significant increases in both viscosity variation with temperature and the variation with shear rate may be due to the fact that after oxidation of vegetable oils some chemical compounds could result, such as hydroperoxides, volatile substances, non-volatile substances, high weight molecular compounds and fatty acids.



#### 4. Conclusions

Oxidation of olive oil is a process that leads to the degradation of the sensorial qualities (color) and generates compounds such as peroxides and aldehydes.

Some aspects regarding olive oil oxidation were clarified, for different temperatures and different periods of time, using spectrophotometric data analysis and Tristimulus Colorimetry method.

Studies performed in order to determine olive oil transmittance showed that this method can be successfully used for the analysis of vegetable oils oxidation, oils that are going to be used as lubricants

in food industry. Olive oil oxidation becomes more obvious by determination of trichromatic parameters. Thus it has been proved that by using this method, conclusive results regarding olive oil oxidation are obtained.

Viscosity variations with temperature and shear rate were determined both for oxidized and non-oxidized olive oils. A strong increase of the olive oil viscosity is observed, when olive oil was oxidized at a temperature of 130°C and for 10 hour period of time of oxidation. The increase of the viscosity represents an indicator of vegetable oil oxidation. Using these two methods, olive oil use parameters could be optimized at the industrial level.

**Table 1.** Experimental results for olive oils oxidized at a temperature of 110°C

Olive oil	Trichromatic components			Trichromatic coordinates			$\lambda_d$ [nm]
	X	Z	Z	x	y	z	
Unoxidized	61.642	67.215	6.232	0.45631	0.49756	0.04613	575
5 hours oxidized	59.43	65.808	10.34	0.43834	0.48538	0.07626	574.5
10 hours oxidized	57.026	62.806	12.879	0.42969	0.47325	0.09704	574.2

**Table 2.** Chromatic characteristics for olive oils oxidized at 110°C - illuminant C/2°

Olive oil	Chromatic coordinates			$a^*/b^*$	$(a^*/b^*)^2$	$C^*_{ab}$	$h_{ab}$
	$L^*$	$a^*$	$b^*$				
Unoxidized	85.61242	-9.5804	100.1562	-0.0956	0.009151	100.6134	95.46
5 hours oxidized	84.89814	-11.688	85.12887	-0.1373	0.018853	85.92757	97.81
10 hours oxidized	83.34022	-10.7599	75.69697	-0.1421	0.020205	76.45787	98.09

**Table 3.** Experimental results for olive oils oxidized at a temperature of 130°C

Olive oil	Trichromatic components			Trichromatic coordinates			$\lambda_d$ [nm]
	X	Z	Z	x	y	z	
Unoxidized	61.642	67.215	6.232	0.456307	0.497561	0.046133	575
5 hours oxidized	72.912	77.103	71.57	0.329048	0.347961	0.322991	562
10 hours oxidized	78.134	81.517	85.986	0.318087	0.33186	0.350053	559.5

**Table 4.** Chromatic characteristics for olive oils oxidized at 130°C- illuminant C/2°

Olive oil	Chromatic coordinates			$a^*/b^*$	$(a^*/b^*)^2$	$C^*_{ab}$	$h_{ab}$
	$L^*$	$a^*$	$b^*$				
Unoxidized	85.61242	-9.5804	100.1562	-0.0957	0.00915	100.6134	95.46
5 hours oxidized	90.36901	-5.4215	14.09896	-0.3845	0.147869	15.10544	111.03
10 hours oxidized	92.36127	-3.4411	6.854868	-0.502	0.251991	7.670076	116.66



**Table 5.** Experimental values of color differences when studied olive oils during forced oxidation - illuminant C/2° (unoxidized – 5 hour forced oxidation, unoxidized – 10 hour forced oxidation)

Olive oil	Time [hours]	$\Delta L^*$	$\Delta a^*$	$\Delta b^*$	$\Delta C^*_{ab}$	$\Delta h_{ab}$	$\Delta E^*_{ab}$
Oxidized oil to 110°C	5	-0.72	-2.1	-15.03	-14.69	2.35	15.19
	10	-2.272	-1.179	-24.46	-24.16	2.63	24.59
Oxidized oil to 130°C	5	4.75	4.16	-86.06	-85.51	15.57	86.29
	10	6.748	6.1394	-93.31	-92.95	21.2	93.75

## References

- [1]. **Stefanescu, I., Calomir, C., Chirita, G.** - *On the future of biodegradable vegetable lubricants used for industrial tribosystems*. The Annals of University "Dunarea de Jos" of Galati, Fascicle VIII, pp. 94-98, ISSN 1221-4590, (2002).
- [2]. **Lambert, W.J., Johnson, I.J.**, *Vegetable oil Lubricants for internal combustion engines and total loss lubrication*, US Patent Nr. 5888947, (1999).
- [3]. **Paz, I., Molero, M.**, Journal. Am. Oil Chem. Soc, 77(2):127, (2000).
- [4]. \*\*\* - CIE Technical Report: Colorimetry, 3rd ed., Publication 15, Central Bureau of the CIE, Vienna, (2004).
- [5]. \*\*\* - CIE Technical Report: Improvement to Industrial Colour-Difference Evaluation, (2001).

- [6]. \*\*\* - CIE Pub. No. 142, Vienna: Central Bureau of the CIE, (2001).
- [7]. **Zgherea, Gh.**, *Analize Fizico – Chimice*, Ed. Fd. Universitare "Dunărea de Jos" Galați, pp. 74-80, 88-94, (2002).
- [8]. **Florea, T., Crețu, R., Zgherea, Gh.**, *Studiul afinității unor coloranți alimentari față de fracțiunile majore ale laptelui*, Buletin de Informare Pentru Industria Laptelui (BIL), Editura Academica, 19 (2), II, pp. 86-101, (2004).
- [9]. **Sancez-Gimeno, A.C., Negueruela, A.I., Benito, M., Vercet, A., Oria, R.**, *Some physical changes in Banjo Aragon extra virgin olive oil during the frying process*, Food Chemistry, No.110, pp. 654-658, (2008).
- [10]. **Gonnet, J. F.** *Colour effects of co-pigmentation of anthocyanin revisited*, Analytical, Nutritional and Clinical Methods Section, Food Chemistry, 75, pp. 474, (2001).



## PREMISES IN THE DESIGN OF COMPUTATIONAL ALGORITHMS FOR REFINING SLAGS APPLIED IN LADLE TREATMENT OF STEELS. INFLUENCE OF BOF SLAG AND OF OTHER SOURCES OF SLAG

**Petre Stelian NITA**

"Dunărea de Jos" University of Galati, Faculty of Materials Engineering and Environment,  
111, Domnească Street, RO-800201, Galati, Romania  
email: pnita@ugal.ro

### ABSTRACT

*In the design of computational algorithms for refining slags for ladle treatment of steels, the evaluation of contributions of different factors is a definitory step, allowing to evaluate the real possibilities and limitations in steel refining practice. Slag carried over from steelmaking converters to the ladle is evaluated from the point of view of contributions of its amount and contents of SiO<sub>2</sub> and iron oxides. It is shown in quantitative manner what it happens in conditions of variations of the above mentioned factors, in the ranges of values closed to real industrial practice. It is shown and concluded that quantitative evaluations of the contributions of slag carried over in refining ladle are of outmost importance. It is possible, under the above mentioned conditions, to ensure adequate values of sulphide capacity, low residual values of iron oxides in economical conditions and to save aluminium from the exaggerate loss by oxidation.*

KEYWORDS: BOF slag amount, SiO<sub>2</sub> content, iron oxydes content, aluminium consumption

### 1. Introduction

Nowadays, informatics applied in engineering of materials plays an increasing role to achieve reproducible quality indicators of products, to increase their levels and simultaneously to save costs, allowing reaching all these in a friendly interaction with the environment. Steel production in oxygen blowing furnaces (BOF), also known as L-D converters and steel refining in different secondary metallurgy facilities, like process in ladle metallurgy, are permanently the object of different measures directed to fulfill the actual requirements for the above mentioned purposes, including the extension of informatics applied in engineering of steelmaking and refining. In this regard, for accurate results that can be obtained with full knowledge, there is no other way than a correct evaluation of technological parameters and requirements from the points of view of their contribution and weight.

Actually, about the whole production of steels obtained at industrial scale in BOF steel plants and electric arc furnaces is treated using slags. Treatment of steels in ladle under slags, applied in various

purposes is applied in order to achieve very low and extremely low contents of sulphur and high purity levels in non-metallic inclusions, is from far one of the most advantageous and cheap methods because of some particular features. Low carbon aluminium killed steels (LCAK) are a wide class of steels grades made in BOF and treated with refining slags in ladle, ladle furnace (LF) and other refining plants.

Despite the fact that technology of steel refining based on synthetic slags is not a new one, its efficiency in obtaining advanced refined steels made it a permanent and an indispensable technique to obtain high quantities of refined steels in conditions of low cost of investments and in short times. The simplicity of the method is remarkable due to the fact that in the ladle, the steel must be always covered by a slag layer along its residing period and therefore the problem to have an adequate slag, corresponding to a certain purpose of maximal utility, could be always posed at large. Therefore the refining of steel, using adequate refining slag became almost naturally a real technological plurivalent tool which must be permanently re-evaluated in order to update the knowledge, procedures and working technologies, all



those serving to increase the technical and economical performances.

## 2. Current state and requirements

There is usually in steelmaking the tradition and practice of using the so-called general or basic recipes which are used because of the availability only of short time intervals, frequently of orders of few minutes, when different intended actions, in different technological steps, are possible in many cases in critical conditions of time. Such a practice is suitable in conditions when parameters of liquid steel are fully in the ranges of certain previous established values, which are practically the desired final values for the processing step in question but unfortunately these are also frequently far from their optimal values. A certain variability of many other factors, other than the ones before mentioned, contributing the values of different parameters of refining is superposed on the mentioned practice, but only rarely these factors are evaluated with satisfactory precision in the traditional procedure. It results that there are not too many freedom degrees in a such procedure and anything out of the usual range of parameters will affect the efficiency of steel treatment. Finally, it could be mentioned that the traditional practice is still wide spread and intensively used, although this is not always recognized fairly. However many of these difficulties can be avoided, the flexibility of the procedures can be increased and the reproducibility rate of the results could be improved, when adequate computational algorithms for slags are implemented, coupled with the availability of certain technological facilities in the steel refining shop. A good evaluation of particular conditions in the steelmaking practice of the steel grades taken into consideration allows for the design of adequate computational algorithms, flexible enough to be useful in many refining purposes, either simultaneously or separately, according to needs and conditions.

Starting from the above general remarks, fully acceptable as veridicity, a procedure of designing computational algorithms, to obtain a refining slag used mainly in desulphurization process of low carbon and low alloyed steels obtained in blowing oxygen converter (BOF) and treated in ladle, could be realized in the established practical conditions. These algorithms once established, tested and evaluated, can be used directly in steel refining practice as a tool for operators use, or at a superior level of integration in neural networks, making possible the management of steel refining processes based on artificial intelligence, replacing older mathematical methods based only on statistics, in the form of static and dynamic models, even of those implemented in on-line computer management facilities.

The necessity of such an approach, like the one suggested in the present paper, is due also to the fact that, despite the huge amount of reported data on slag refining technologies, there are only formal and often incomplete aboard, the most frequent limited to a narrow target.

## 3. General premises of computational algorithms for refining slags

Starting from necessities, a set of general and preliminary premises have been established, as it follows, in the form of direct and indirect sources:

1. the natural sources of slags during steel refining from starting of tapping to the end of treatment in the ladle, and even later if deleterious actions on quality occur;
2. the external sources of slags-fluxes, introduced in the process to obtain certain numerical values of the edificatory physico-chemical properties in an optimised manner;
3. the physico-chemical properties and their values related to slags in general and to refining slags, in particular;
4. the main refining process taken into account to be performed and the potential possible and desired adjacent refining processes, which can be coupled to the first;
5. the adjacent undesired processes taking place naturally or associated to the desired processes; their actions must be obligatorily known, evaluated and limited in their development.
6. the impact on environment taken into account from various points of view, starting from the possible action on life and work environment, to the impact on social environment and recycling.

All these aspects mentioned above must be carefully evaluated according to their characteristic actions, amounts, and weight from the various points of view which are relevant.

## 4. Contribution of (BOF) slag to the refining slag

Slag resulted from steelmaking process in BOF process, called shortly (BOF) slag, is an important primary source in obtaining the refining slag from the point of view of quantity and as an initial factor of influence acting further and determining technological actions and measures to bring it in the range of requirements. Despite this, in practice the weight of its contribution is not always precisely evaluated and included in computations. Many times the results of treatments under slag are bad, even disastrous, because of this attitude. Unfortunately, it seems that many times the amount of slag transferred



in the ladle during tapping of steel not only it is not measured, but even it is not at least evaluated somewhat objectively. In an extensive study dealing also with evaluation of amounts of different sources leading to impurification of steel, the slag carried over to the ladle during tapping is about 3kg/t liquid steel, in a normal practice using different stoppers of slag [1]. Frequently and not only accidentally in the industrial practice the amount of slag carried over to the ladle during tapping is even higher than the amount mentioned above.

At the end of the heat BOF the slag contains high levels of iron oxides according to the carbon content and the temperature at the end point of blowing. In great measure this depends also upon the performing oxygen blowing combined with argon bubbling through nozzle placed on the bottom of the converter when such a facility and practice are used. Some typical chemical compositions of slags, at the end of oxygen blowing presumed to be identical to the transferred slag from converter into the pouring/refining ladle, are presented in table 1.

**Table 1.** Main chemical compositions (rounded values) of final slags in BOF

Ref. No./year	Chemical composition of slag, mass %								
	CaO	MgO	SiO <sub>2</sub>	Al <sub>2</sub> O <sub>3</sub>	FeO <sup>(*)</sup>	Fe <sub>2</sub> O <sub>3</sub> <sup>(*)</sup>	MnO	P <sub>2</sub> O <sub>5</sub>	S <sup>(**)</sup>
[2]/1999	48	1	12	1	26	-	0.3	3.3	0.12
[3]/2004	30-35	5-15	8-20	1-6	10-35	-	2-8	0.2-2.0	0.07-0.14
[4]/2006	52	5	11	1.3	17	10	2.5	1.3	-
[5]/2007	45	10	11	2	11	11	3	-	-
[6]/2009	48	6	12	2	23	-	2	2.7	-
[7]/2010	48	-	13	3	-	24	2.6	1.5	-

(\*)-upon the analysis method; (\*\*) -derived from the content of SO<sub>3</sub>, initially determined

Valuable sources of data are provided in papers published in the adjacent research fields of waste management, recycling and cement industry. From far there are strong evidences that, despite efforts to standardize the technological process of steelmaking in BOF, according to conditions, high variability of final chemical compositions of slags is present. Therefore, once again, high quality algorithms must be applied when refining processes with BOF slag participation take place.

The steelmaking process and refractories contribute in most cases to the chemical composition of slag. The necessity to take into consideration these aspects could result from comments on the chemical composition of slags in table 1. As a general remark, it can be said that there are practically two major tendencies in the use of refractory linings, the first being to use classical lining based on dolomitic blocks and the second to use the lining based on magnesite elements, more or less evaluated, including those in the class MgO-C. In order to decrease the wear of such lining, due to the chemical agresivity when SiO<sub>2</sub> content is at high levels [3], also is encountered the practice consisting in increasing MgO content to levels closed to saturation of slag with MgO. Therefore in table 1 the component MgO is present in contents of very high variability [2]-[6]. This fact is frequently associated with the content of silica in slag. Increasing the content of MgO in slag is more efficient in lowering the aggressivity of slags at high contents of SiO<sub>2</sub> due to the lower molar mass of MgO because of the bigger numbers of moles contained in the same amount, compared to the CaO.

Slags from table 1 ref [3] are the result of modern steelmaking process, in BOF lined with magnesite, therefore they contain 5-15mass % MgO. In the same time in the respective BOF are processed heating based on highly preliminary treated crude liquid iron with desulphurizing reagent up to low contents of sulphur and therefore the sulphur content in the final BOF slag is low, below 0.014 mass%. The relatively high final content of FeO (10-35 mass%) and of MnO (2-8 mass%) proves the heating has been processed with low proportions of iron scrap as cooling materials in favor of oxydic materials, perhaps iron ores.

Silica content in final slags (8-20 mass %) seems to prove that have been processed both desilicized crude iron and crude iron with normal silicon content were used.

Due to the same mentioned conditions, final slags contain low contents of phosphorus oxyde (0.2-2%) [3].

As a general consideration, heatings must be processed in BOF with the lowest possible amount of slag. In the case of such slags, attention will be paid to contents of FeO and MnO, being known that refining of steels under slags requires extremely low contents of FeO+ MnO, usually bellow 1-2 mass% [8].

The necessities of the chemistry in BOF determine high contents of iron oxydes in slag along the whole processing route of heatings. Excepting the content of CaO which is the highest in the BOF slag, iron oxydes are on the second place at levels of 22-35 mass % the sum of both two oxydes obtained by chemical analysis (FeO+Fe<sub>2</sub>O<sub>3</sub>).

### 5. Evaluation of effects of BOF slag on some technological parameters and on the estimated performances of refining slags

In the above mentioned conditions, due to their composition, (BOF) slags give a set of limits in what regards the amount of refining slag and even their composition, sometimes limiting also the maximal refining performance to lower levels than the theoretically required highest values.

The refining slags used for advanced desulphurization and advanced removal of oxydic inclusions in low carbon aluminium killed (LCAK) steels are based in the system CaO-MgO-Al<sub>2</sub>O<sub>3</sub>-SiO<sub>2</sub> with some additions of fluorine as fluidizer. In such slags, besides optimal ranges of the major components CaO and Al<sub>2</sub>O<sub>3</sub>, there are severe limitations for SiO<sub>2</sub> contents, usually at max. 5mass% in order to limit the increasing of silicon content in LCAK grades where it is limited or prohibited like it is in many grades of high strength low alloyed (HSLA) steels. Many times even more severe restrictions are imposed consisting in limitation of SiO<sub>2</sub> to levels below 2.5 mass%.

Another restriction is imposed concerning the sum of contents of FeO and MnO, limited to below 1mass% and admitted sometimes for qualities not so high up to 1.5-2mass%. These contents must be compared to the values from table 1 in order to evaluate the directions to action in order to fulfill the

requirements in conditions of the amount of BOF slags carried over in refining ladle.

Particular values of the (%SiO<sub>2</sub>) contents in the refining slag could be computed using the following relation:

$$(\%SiO_2) = \frac{\sum_{i=1}^n q_i \cdot (\%SiO_2)_i}{\sum_{i=1}^n q_i} \cdot 100 \quad \%mass \quad (1)$$

where:

i - current number of source of slag;

n - total number of sources of slag;

q<sub>i</sub> - amount of slag from source i;

(%SiO<sub>2</sub>)<sub>i</sub> - SiO<sub>2</sub> content of source i, in %mass.

but a valuable and fast image on the simultaneous influence of the SiO<sub>2</sub> contents and of different sources of slags could be obtained using Figure 1 or a similar figure.

Data presented in Fig. 1 are in the range of interest in the industrial practice; the range of accidental of hazardous data is avoided. It is obvious that only carefully an adequate refining slag could be obtained and that the process of obtaining the slag is a very sensitive one to complex factors as composition and the amount of the converter slag carried over in the refining slag. It is difficult to obtain contents of SiO<sub>2</sub> as low as possible, but it is possible to take adequate measures to limit these contents at required values satisfying which meet the requirements.

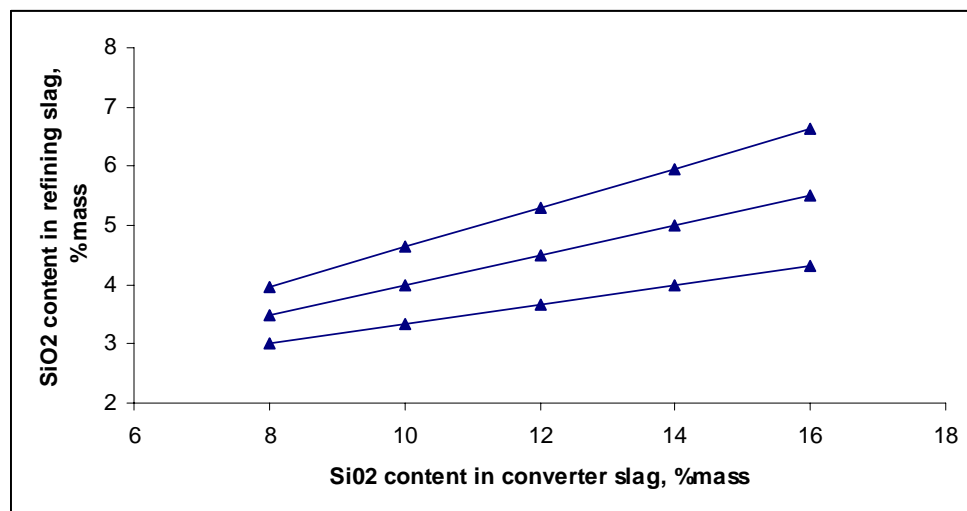


**Fig.1.** Influence of the SiO<sub>2</sub> content in converter slag and of the amount of slag carried over on the SiO<sub>2</sub> of the refining slag in the ladle.

Reference steel heat treated under slag - 180t; reference amount of refining slag -2160kg (corresponding to 12kg slag/tonne liquid steel). Converter slag carried-over in the ladle: 720kg (upper line); 540kg (middle line); 360kg (lower line). Contribution of other components added to form refining slag- 2%mass SiO<sub>2</sub>



The content of SiO<sub>2</sub> in slag acts as a major factor in the activity of SiO<sub>2</sub> in slag and the basicity of the refining slag.

Considering a slag in the system CaO-Al<sub>2</sub>O<sub>3</sub>-SiO<sub>2</sub> where CaO and Al<sub>2</sub>O<sub>3</sub> represents the base

(%CaO+ %Al<sub>2</sub>O<sub>3</sub> = min.90% mass) at a ratio %massCaO/ %massAl<sub>2</sub>O<sub>3</sub>=1.4, it results a chemical composition of the CaO-Al<sub>2</sub>O<sub>3</sub>- SiO<sub>2</sub> shown in Table 2. for various concentration of SiO<sub>2</sub> in the refining slag.

**Table 2.** Several quality indicators of CaO-Al<sub>2</sub>O<sub>3</sub>- SiO<sub>2</sub> slags at various contents of SiO<sub>2</sub> and ratio CaO/Al<sub>2</sub>O<sub>3</sub>=1.4, compared to the pure CaO-Al<sub>2</sub>O<sub>3</sub> slag at the same ratio

Quality indicators of slag	Chemical composition of CaO-Al <sub>2</sub> O <sub>3</sub> - SiO <sub>2</sub> (C-A-S), %mass			
	3% SiO <sub>2</sub>	6% SiO <sub>2</sub>	9%SiO <sub>2</sub>	0% SiO <sub>2</sub>
Basic composition	A=40.42 C=56.58	A=39.17 C=54.83	A=37.92 C=53.08	A=41.67 C=58.33
*Optical basicity, Λ	0.76863	0.75587	0.74799	0.78176
*Sulphide capacity, C <sub>s</sub> at 1873.15K	4.309x10 <sup>-3</sup> (72.21%)	3.1405x10 <sup>-3</sup> (52.63%)	2.58321x10 <sup>-3</sup> (43.29%)	5.967x10 <sup>-3</sup> (100%)

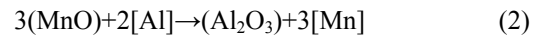
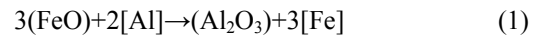
\*computed according to ref.[8]:

$$\Lambda = \frac{1.783\%CaO + 1.756\%Al_2O_3 + 1.598\%SiO_2}{1.783\%CaO + 2.943\%Al_2O_3 + 3.33\%SiO_2}; \lg C_s = 10.767 \Lambda - 10.64$$

The deleterious effect of the presence of SiO<sub>2</sub> content in slag, exerted on relevant technological properties involved in refining operation, is better shown by the decrease of the sulphide capacity C<sub>s</sub>. Even a relatively reduced percentage of SiO<sub>2</sub> in slag, despite of an apparently not important decreasing of the optical basicity of slag (1.68-3.38%), exerts very strong effects in decreasing the sulphide capacity of slag of an important magnitude (42.29-72.21%), compared to the similar slag without SiO<sub>2</sub> content, further affecting in a negative manner the efficiency in removal of sulphur and the final content of sulphur in steel. These results have been confirmed experimentally in ref. [8], also in many other published papers, here not cited because of economy reasons.

It is extremely obvious that the main source of iron oxides in the refining slag is the slag carried-out from converter in the refining ladle. As it is shown in table 1 in the widest range, considering oxides in the form of FeO, this content is 10-35%mass, but more

frequent the sum of iron oxides contents is Σ(FeO+Fe<sub>2</sub>O<sub>3</sub>)=20-27%mass and (MnO)=2-3%mass. An important loss of aluminium will be in steel due to the reactions of slag deoxidization, which takes place in the presence of aluminium content from aluminium killed steels:



For easiness, the content of MnO will be included in the sum of iron oxides because of the small content of MnO in BOF slag and closed molar masses (M<sub>Mn</sub> =54.93 and M<sub>Fe</sub>=55.84), also considering only the FeO form.

The quantity of aluminium in liquid steel, consumed directly q<sub>[Al]</sub><sup>c</sup> in order to reduce the (FeO) content to a final residual value, according to the reaction (1), is given by the following relation:

$$q_{[Al]}^c = \left[ q_{BOF} \cdot (\%FeO)_{BOF} - Q_{slag \ ladle} \cdot \frac{(\%FeO)_{residual}}{100} \right] \cdot \frac{2 \cdot M_{Al}}{3M_{FeO}}, \text{ kg/heat} \quad (3)$$

where:

q<sub>(BOF)</sub>- is the amount of BOF slag carried over in the ladle ;

(%FeO)<sub>BOF</sub>- is the FeO content in the BOF slag;

(%FeO)<sub>residual</sub>-is the residual content of (FeO) in refining slag;

Q<sub>slag ladle</sub>- is the amount of refining slag, from all sources;

M<sub>Al</sub>, M<sub>(FeO)</sub> – are respective molar mass of aluminium (27) and of iron oxyde (72).

Data from Fig. 2 show the necessary amounts of aluminium for reduction of iron and manganese oxides in the slag carried over form BOF in the ladle refining. Reduction starts in industrial conditions from initial contents in the range (FeO+Fe<sub>2</sub>O<sub>3</sub>)=20-

35mass% and (MnO)=2-4mass% even less than 1%mass. The refining slag must contain much more lower contents of iron and manganese oxides in order to be of certified utility. The sum of their contents must be lower than 1-2 %mass. Sometimes, due to

requirements to guarantee extra low activity of oxygen and of extra low content of oxide inclusions, this sum must not exceed 0.5- 1.0%.

These extra low contents also favorize a deep removal of sulphur from steel in the refining slag. Unfortunately, this is obtained scarifying a certain content from the aluminium present in the liquid steel, and this must be compensated by re-feeding the corresponding amount of aluminium, usually by

immersing wire of Al. From Figure 2 it results that, in the case of a heat of 180 t liquid steel, in conditions of addition 1.5KgAl/tonne, important amounts of aluminium are consumed to reduce content of iron oxides below 1%mass and these amounts must be taken into account in algorithms of any mathematical model to ensure the accomplishing of different functions of performance concerning the quality by refining.

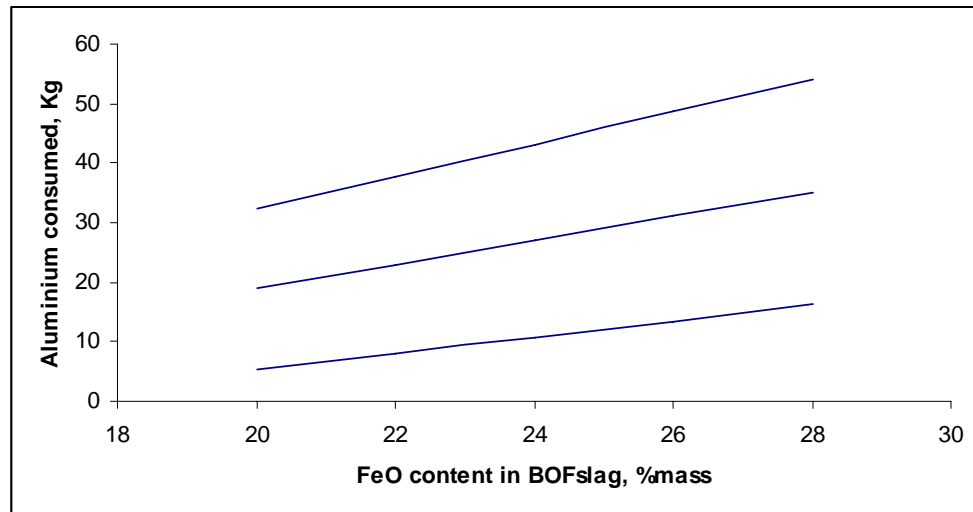


**Fig. 2.** Consumption of [Al] in steel due to reduction of iron oxydes contents in the ladle slag from initial content to 1% FeO residual content in slag, starting from values coresponding to input with various BOF slag amounts.

Reference steel heat treated under slag - 180t; reference amount of refining slag ( $Q_{slag\ ladle}$ ) 2160kg (corresponding to 12kg slag/tonne liquid steel); Final content in the ladle slag (%FeO)<sub>residual</sub>=1%.  
BOFslag carried-over in the ladle: 720kg(upper line); 540kg(middle line); 360kg(lower line)

## 6. Conclusions and comments

From the theoretical approach and the results presented, the final slag in BOF converter contributes the final results of steel refining operations by the following major factors:

a. SiO<sub>2</sub> content acting in the sense of decreasing the sulphide capacity of slag which is one of the defintory parameters of slag in desulphurization of steel. The decreasing of the negative influence of SiO<sub>2</sub> content is costly and practically it may be performed only by increasing the total amount of slag by supplementing the additions. The possibilities to do this are limited in a narrow range and other performance indicators of steel refining efficiency became worse due to the increasing of slag amount in the ladle.

b. the amount of slag carried-over in the refining ladle, during tapping;

c. the content of iron oxides, whenever this indicator is expressed.

As general conclusions, it might be mentioned that the refining of steel under slags is possible, efficient and might be optimized as performance and costs, only if the amount of transferred slag from converter to the ladle is limited to less than 400-500kg/heat (180tonnes of steel) and the content of SiO<sub>2</sub> in slag to also limited at less than 12% mass. At a such moderate and acceptable amount of BOF slag carried over in the refining ladle, the intake of iron oxides is also moderate and the necessary content for successful refining operation (including FeO<0.5-1%mass) is controllable by usual operations during current operations involved in normal practice and normal duration of the refining period. Reduction of iron oxides in the ladle slag is realized with an important consumption of aluminium (7-54kg/heat of 180t of steel) at a reference amount of slag 2120kg equivalent to 12kg slag/t steel.

These conditions are relatively easy to be accomplished in the normal practice of steelmaking in



BOF, but they are easier to be ensured if the pre-treated liquid iron is used.

A complex treatment of liquid iron consisting in decreasing the content of silicon, sulphur and carbon, combined with steelmaking in BOF equipped with argon bubbling bottom nozzles is the optimal solution to minimize the possible negative effects of converter slag carried – over in the refining ladle.

There is evidence that, if optimal parameters of BOF slag carried over in the ladle refining are not respected, any computational algorithm will give receipts and parameters for treatment with refining slag out of optimal range satisfying technical and economical requirements.

Mainly either due to the necessity to prolong too much the duration of treatment or due to the increasing of the necessary amount of refining slag, refining process will evaluate with difficulty and usual purposes of treatments, i.e. obtaining low

contents of oxide inclusions and/or low contents of sulphur, are missed or are random.

## References

- [1]. **Zhang L., Thomas B.G.** - ISIJ International 43, no. 3 (2003): 271–291.
- [2]. **Das B, Prakash S., Reddy P.S.R. and Misra V.N.** - Ressources, Conservation and Recycling 50 no.1 (2007):40-57.
- [3]. **Shi Caijun** - Journal of Materials in Civil Engineering 16, no.3 (2004):230-236.
- [4]. **Poh, D. and Ghataora, G.S. and Gazireh, N.** - Journal of Materials in Civil Engineering 18 no.2 (2006):229-240.
- [5]. **Tossavainen M., Engstrom F., Yang Q., Menad N., Larson M.L. and Bjorkman J** - Waste Management 27 no.10 (2007): 39-48.
- [6]. **Mahieux P.Y., Aubert J.E. and Escadeillas, G.** - Construction and Building Materials 23 no.2 (2009): 742-747.
- [7]. **Valigora J., Bulteel D., Degrugilliers P., Damidot D., Potdevin J.L. and Messon M** - Materials Characterization 61 no.1 (2010): 39-48.
- [8]. **Nita, P. S., I. Butnariu, and N. Constantin** - Revista de metalurgia 46, no. 1 (2010): 5-14.



## OCCUPATIONAL RISK MANAGEMENT IN INDUSTRY

**Tamara RADU, Maria VLAD, Viorel DRAGAN, Vasile BASLIU,  
Gina Genoveva ISTRATE**

"Dunărea de Jos" University of Galați, 111, Domnească Street, 800201, Galați, Romania  
email: tamara.radu@ugal.ro

### ABSTRACT

*Occupational risk management is part of the occupational health and safety at workplace. Occupational risk management has a specific component relating to the assessment of the risk and a common component of all types of management including: planning, organizing, implementing, and controlling. Managers must understand the legal and moral liability of their job in ensuring a healthy and safe workplace and to make all necessary efforts to achieve and maintain this goal. Although this action is the responsibility of management, employees also have a role as important in ensuring health and safety at the workplace.*

*The case study approach, this paper aimed to determine if employees respond to the important efforts being made by the organization to reduce the level of risk in the workplace and improve security. The case study was based on questioning of one total of 64 employees in the industrial sector in Galați area Romania. The questionnaire had a total of 24 questions chosen so as to show how well the respondents understood the occupational risk management, the attitude towards risk assessment at the workplace, how vigilant are at the workplace, if they understood measures security and the extent to which they meet.*

**KEYWORDS:** Occupational risk, employee's involvement, understanding, attitude, vigilance

### 1. Theoretical aspects

The standard O.H.S.A.S. 18001 (revised in 2007) shows in section 4 that organizations have to develop all the functions of occupational risk management such as: security policies, organizational plan, the hazard identification, risk assessment, implementation, control, monitoring, and continuous improvement [1, 2, and 3].

Risk management is therefore part of the occupational health and safety at workplace can be integrated with environmental management and quality management.

Adoption by the organizations of risk management was stimulated by trade unions, advances in medicine, technology upgrading, standards, legislation and other factors.

As result of the OHSAS 18001 occupational risk management has a specific component relating to the assessment of risk and a common component of all types of management namely: planning, organizing, implementing, controlling.

Speciality literature [4, 5, and 6] is in agreement with the following steps in the evaluation of occupational risk:

- identifying hazards;
- measuring (assessing) risk in terms of severity and probability;
- risk analysis;
- response to risk;
- control and monitoring of risks.

There are no fixed rules regarding risk assessment but mentioned steps assure us that the process is adequate and sufficient. Identifying hazards is widely recognized as the most important stage of the process. These steps require guidance by risk specialists and an experienced working team. Successful approach is provided as management involvement and active participation of the employees. There are also methods that can be used to identify hazards [7, 8, and 9] such as: Check list, What if? Tee Fault Analysis, Analysis of Failure Modes and Effects "(FMEA) Brainstorming, Hazard Study and Operability (HAZOP), etc.



For low risk activities such qualitative methods allow a simple risk assessment and taking immediate and appropriate action. For organizations with numerous risk factors this qualitative analysis will be followed by a quantitative analysis techniques and appropriate methods.

Risk assessment is considering two main components: the severity of the consequences resulting from the production of a hazard and the probability of that hazard. Most methods for assessing the severity of consequences and likelihood of happening receive a numerical value (class) with clear explanations and descriptions. Risk assessors will fit correctly hazards in these classes.

Size of risk can be assessed by multiplying the two factors [7]:

$$R = G \times P \quad (1)$$

where: R - risk value;

G - class of severity of hazard consequences

P - class the probability of chance;

or torque is estimated by two factors [10]:

$$R = (G, P) \quad (2)$$

Risks are classified according to their size and risk levels then enclosed in a matrix which allows identification of major hazards requiring urgent action. Our country applies a domestic method devised by ICSPM in 1998 which provides 7 grades of severity, 6 classes of probability and seven levels of risk. It is established a partial risk on each hazard and risk global is established with relationship:

$$Nr = \frac{\sum_{i=1}^n r_i \cdot R_i}{\sum_{i=1}^n r_i} \quad (3)$$

where: Nr = the global risk level on the workplace;

$r_i$  = risk factor rank "i";

$R_i$  = risk level for the hazard "i";

n = number of hazards identified at the workplace.

Risk analysis involves risk ranking and classification in acceptable risk and unacceptable risk.

Legislation in our country has the global risk threshold value 3.5 (calculated with Equation 3). Also at this stage it is verify all existing measures and procedures to control risks. All the specialists make observation that risk analysis should identify the major hazards that can damage important to the health and safety of employees, but also significant financial harm. Therefore, even if apparently risk management requires financial expenses, applying it will bring many benefits.

For answer to risk is very important to apply measures in the following order of priority (ILO Recommendation No. 193 Paragraph 5):

- elimination of the risk;
- control of the risk at the source;
- minimisation of the risk by such means as the design of safe work systems, the introduction of technical and organisational measures and safe practices and training;
- use of personal protective equipment and clothing (at no cost to the worker).

The control activity and monitoring of the risk is a common component of management. You will adopt and promote a policy that describes the security measures, responsibilities of management and employees. There are procedures clear and easy to understand. Will be put in place mechanisms for consultation between employees and between employees and their elected representatives on all aspects of the existing risks in the workplace This actions encourages a proactive behavior of employees beneficial in understanding and applying security measures. Besides technical measures other measures such as information, training and continuous training of employees for knowledge and risk awareness is essential [11].

Managers must understand the legal and moral liability of their job in ensuring a healthy and safe workplace and to make all necessary efforts to achieve and maintain this goal. Although this action is the responsibility of management, employees also have a role as important in ensuring health and safety at the workplace [12, 13, and 14].

The case study approach, this paper aimed to determine if employees respond to the important efforts being made by the organization to reduce the level of risk in the workplace and improve security.

## 2. Case study regarding employee response to the implementation of risk management

The case study was based on questioning a total of 64 employees in the industrial sector in Galati area Romania. The questionnaire had a total of 24 questions chosen so as to show how well the respondents understood the occupational risk management, the attitude towards risk assessment at the workplace, how vigilant are at the workplace, if they understood measures security and the extent to which they meet.

Figure 1 shows the level of understanding of occupational risk by those polled. Were well appreciated by the responses of 16 (25%) respondents. They know the very basics of hazard and risk have been trained and are aware of the risks and hazards of the workplace, were directly involved in the risk assessment.

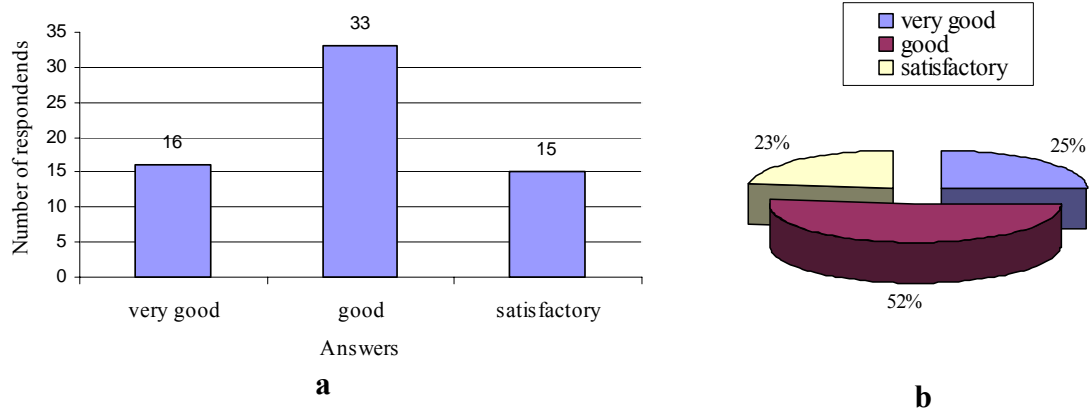


**Fig. 1. Understanding level of risk management:**  
 a) on number of interviewed employees b) in [%]

Were well appreciated by a total of 33 (52%) who know the notion of risk and hazards at the workplace, know emergencies situations and participated in the assessment of the risk by the representatives. Satisfactory appreciated by 15 (23%) of the respondents. They understand the concept of risk and the need for security measures work, admit

they were and are regularly trained in occupational safety but do not know the risk factors and hazards of the workplace and any measures taken by employers to avoid risks.

Figure 2 presents the results of the respondents on attitudes towards risk assessment process at the workplace.

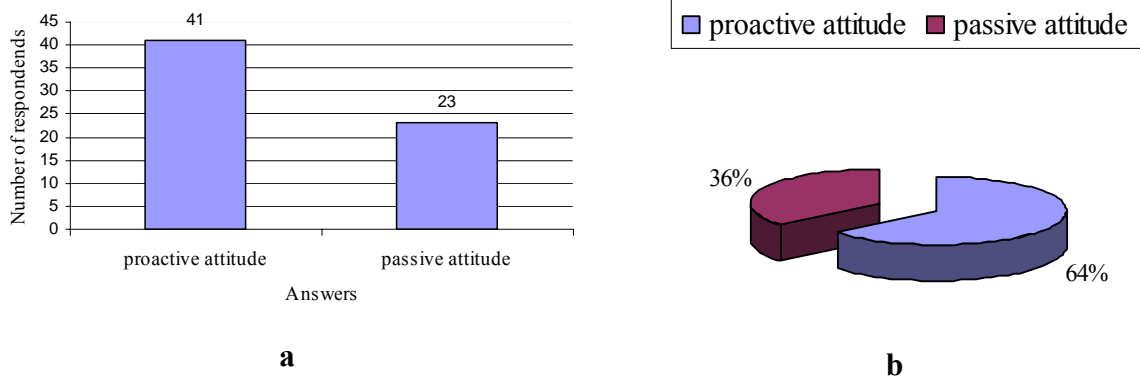


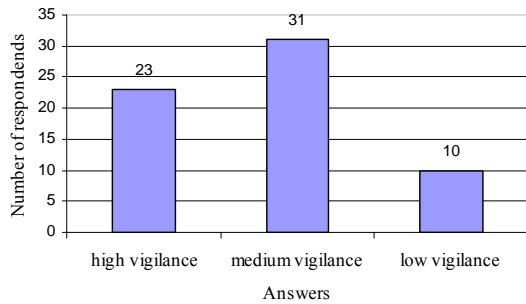
**Fig. 2. Attitude towards risk assessment process:**  
 a) on number of interviewed employees, b) in [%]

It was considered a proactive attitude to 41 (64%) respondents interviewed respectively who were involved in evaluating the risk personally or through representatives, know the difference between a situation of risk and one normal, know the dangers of the workplace and emergency situations. A passive attitude was assessed for 23 (36%) respondents who are not paying attention to trainings, consider employer solely responsible for prevention, consider excessive security measures.

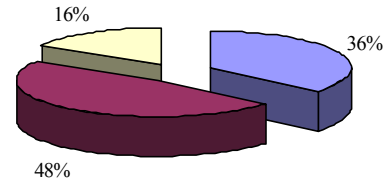
Results concerning vigilance at the workplace are shown in Figure 3 and it was considered on three

scales: high, medium and low. Were considered the most vigilant employees who take steps to feel safe at the workplace; considers that routine work not diminish vigilance; are paying attention to training even know what it is about, never happened not to use safety equipment, know all the risk factors and at the workplace hazards. They were in total of 23 (36%) respondents.

They were appreciated with medium vigilance a mean of 31 (48%) who admitted that it was happened not to use safety equipment and do not know the risk factors at the workplace.



■ high vigilance ■ medium vigilance □ low vigilance



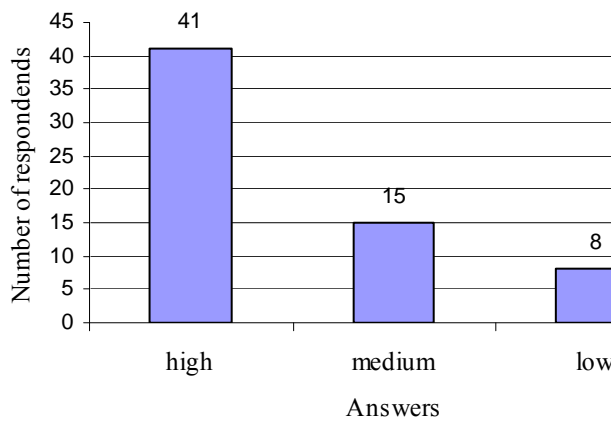
**a**

**b**

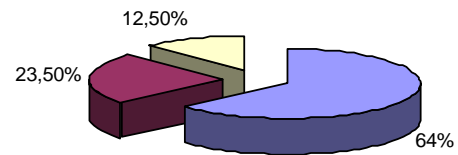
**Fig. 3. Vigilance at the workplace: a) on number of respondents, b) in [%]**

With low vigilance were considered to be the inattentive to instruction and who does not take all safety measures at the workplace respectively a total of 10 (16%) respondents.

Figure 4 shows the results concerning the level of understanding of occupational safety measures. This was assessed on three levels: high, medium and low.



■ high ■ medium □ low



**a**

**b**

**Fig. 4. Level of understanding of occupational safety measures: a) on number of interviewed employees b) in [%]**

It is seen from the graphical representation that most employees, 41 people [64%], understand the need for security measures of work. However, besides the positive rated answer, the respondents underline that would get advices concerning safety at workplace. Respondents do not take always measures to feel safe at the workplace. A total of 15 [23.5%] respondents were appreciated with medium understanding of security measures. A total of 8 (12.5%) people said that security measures are exaggerated and believes that safety equipment is not always absolutely necessary. Figure 5 shows the extent that employees respect work safety measures.

We established in this respect three stages of assessment: high, medium and low extent.

Most of those respondents answered "yes" to the question if they comply with safety occupational measure at the workplace but the answers at other relevant questions did the differentiation on the three steps.

Many of them said they consider uncomfortable safety equipment (24) and have been times when they not worn (27) or do not know measures in case of fire (then how to comply?) and another 13 respondents recognized directly as not comply with occupational safety measures.

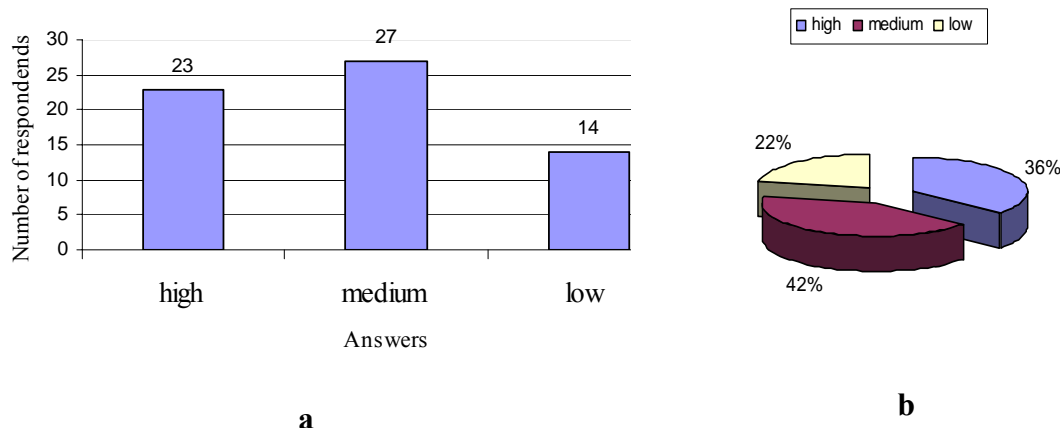


**Fig. 5.** Far as employees respect occupational safety measures:  
a) on number of interviewed employees b) in [%]

### 3. Conclusions

The case study shows that at the organizations level it has been implemented occupational risk management and it has been done a risk assessment for each job. Thus 94% of those surveyed said they were informed (signed) on risk factors and specific hazards of the workplace and over 65% have personally participated in risk assessment. All respondents confirm that they are trained on occupational safety issues (daily, monthly or quarterly depending on their activity).

- Although managers meet their legal and moral obligations regarding occupational safety the case study shows that employees are still many steps to go up to an optimal response to these efforts, as follows:

- 37% of respondents consider only the employee or employer responsible only to the prevention of at the workplace hazards;

- over 40% do not know the risk factors and 32% do not know what is the usual procedure in case of fire;

- 16% show a low vigilance at the workplace;

- 22% respect to a small extent occupational safety standards;

Over 50% would not report an incident if it has no consequences; 15.5% said that faced with a situation of risk at the workplace.

### References

[1].\*\*\* - EORM, 2008: OHSAS 18001 and OSHA's VPP: Development and Comparison Priority Press ED. No.8. (2008).

[2]. \*\*\* - LMCS, New International OHSAS 18001 2007 Management System (2007).

[3]. <http://ufh.netd.ac.za/bitstream/10353/217/2/mini-dissertation.pdf>.

[4]. **Cothler, R.C.** - *Handbook for environmental risk decision making*, Lewis Publishers, New York (1995).

[5]. **Băbuț G., Moraru R.** - *Environmental risk characterization principles*, Proceedings of the 6<sup>th</sup> Conference on Environment and Mineral Processing, part. I, p. 17-21, VŠB-TU Ostrava, Cehia, 27 - 29.06.2002.

[6]. *Workplace Health and Safety Handbook*, [http://www.safework.sa.gov.au/uploaded\\_files/hsr\\_handbook.pdf](http://www.safework.sa.gov.au/uploaded_files/hsr_handbook.pdf) nov.2012.

[7]. **Ozun A., Anghel C.** - *Evaluarea riscului tehnologic si securitatea mediului*, Ed. Accent, Cluj Napoca (2007).

[8]. **Kletz T.** - *Hazop and Hazan Identifying and assesing process industry hazards*, Fourth Edition Institution of chemical Engineers, (1999).

[9]. **Lees F. P.** - *Loss Prevention in the Process Industries: Hazard identification, assesment and control*, Second Edition, United Kingdom (1996).

[10].\*\*\* - *Metoda de evaluare a riscurilor de accidente si imbolnavire profesionala la locurile de munca*, Institutul de Cercetare pentru Protectia Muncii, ICSPM Bucuresti, (1998).

[11].\*\*\* - WHO Regional Office for Europe, *Good Practice in Occupational Health Services Contribution to Workplace Health*, World Health Organization (2002)..

[12]. **Hayes, B.E. Parendar, J. Smecko, T. And Trask, J.** - *Measuring Perceptions of Workplace Safety; Development and Validation of Work Safety Scale*. Elsevier Science USA. *Journal of Safety Research* Vol. 29 No.3. (1998).

[13]. **Radu T., Ciocan A., Vlad M. Balint S. I., Dragan V.** - *Environmental risk assessment in the galvanizing steel sheets*, Proceeding of the International Multidisciplinary Scientific Geoconference, SGM vol. V p.391-397 (2012).

[14]. **Radu T., Vlad M., Bodor M.** - *Environmental risk management at hot dip galvanizing*, The Annals of "Dunarea De Jos" University of Galati, Fascicle IX. Metallurgy And Material Science, May 2011, special issue p.263-269, Galati University Press.

## RESEARCHES REGARDING THE INFLUENCE OF STEAM OXIDATION ON SINTERED ALLOYS PROPERTIES

Mihaela MARIN, Florentina POTECAȘU,  
Octavian POTECAȘU

"Dunărea de Jos" University of Galați, 111, Domnească Street, 800201, Galați, Romania  
email: mihaela.marin@ugal.ro

### ABSTRACT

*In this paper is studied the influence of steam treatment applied on sintered steels and the mechanical properties and abrasive wear behavior for two different types of powder. Steam treatment was carried out at temperature of 550° C and maintaining time of 60 minutes. It was found that the best values for Vickers microhardness and abrasive wear were recorded for sampler P<sub>2</sub>.*

KEYWORDS: powder metallurgy, sintering, steam treatment, mechanical properties, abrasive wear

### 1. Introduction

In the last years, there has been a growing trend in utilisation of ferrous and nonferrous alloys obtained through powder metallurgical (P/M) processing. Comparing it with conventional casting techniques, this technique offers some advantages, such as: a low processing temperature, a near-net shaping, more material utilization (>95%). The properties of a P/M component depend on the sintering cycle [1, 2].

The four basic stages of powder metallurgy are: powder manufacture, powder mixture, pressing and sintering.

Sintering is the process of compaction, consolidation by heat treatment of a compacted product [3]. During sintering, surface, intergranular and volume diffusion are the mechanisms involved in the transport of material [4]. The properties of sintered materials are determined, in the first step, by the nature of the material's characteristics for powders involved, and secondary by pressing and sintering process parameters [5].

Steam treatment is a surface treatment applied to sintered iron-based parts to reduce the interconnected pores by sealing with iron oxides [6]. Comparing it with plastic or copper impregnation, this treatment is an economic way. An increase in the hardness, wear resistance and corrosion resistance by the oxide formed was detected occur [7 – 18].

In this paper, the mechanical properties and abrasive wear behavior of steam treatment on the sintered alloys were analyzed.

### 2. Experimental procedure

#### 2.1. Materials

Specimens prepared from atomized iron powder and from pre-alloyed iron base powders were analyzed in this paper. The chemical composition of the powder samples, pure iron and iron-based pre-alloyed powder with Cu, Ni and Mo is presented in Table 1. In Figure 1 is presented the size distribution of the analyzed powders.

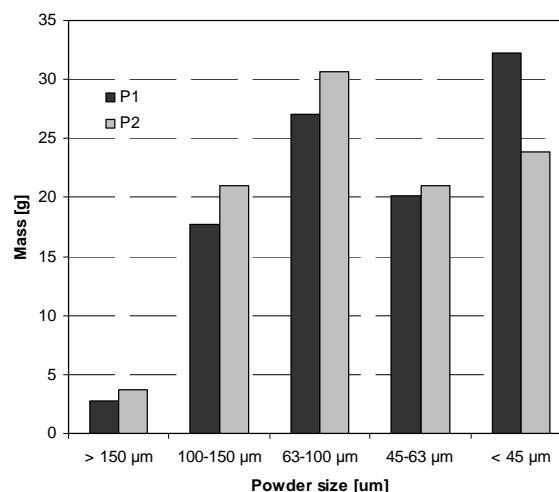


Fig. 1. The size distribution of analyzed powders

To evaluate the mechanical properties, a die for making the samples in the form of a cylinder was produced.

**Table 1.** The chemical composition of analyzed powders, %

Powder type	Cu	Mo	Ni	C
P <sub>1</sub>	0.096	0.008	0.046	<0.01
P <sub>2</sub>	1.50	0.50	4.00	<0.01

The samples were used to evaluate the mechanical properties such as Vickers microhardness and abrasive wear. The powders were mixed with 1% zinc stearate. The samples were compressed in a universal mechanical testing machine to a pressure of 600 MPa, the dimensions of disc specimens are  $\phi 8 \times 6$  mm (Fig. 2).

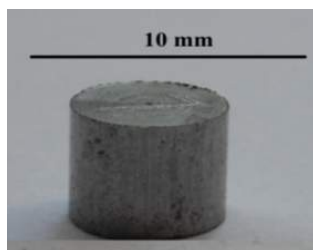


**Fig. 2.** The aspect of a sample

The green samples were sintered in a laboratory furnace, within a controlled atmosphere. The sintering temperature was approximately 1150°C and the sintering time was 60 minutes with a heating rate of 30-40°C/min. All the samples were kept in the furnace for slow cooling to room temperature.

After cooling to room temperature the samples were steam-treated. The steam treatment temperature was approximately 550°C and the maintaining time of 60 minutes. Specimens were then air-cooled at room temperature.

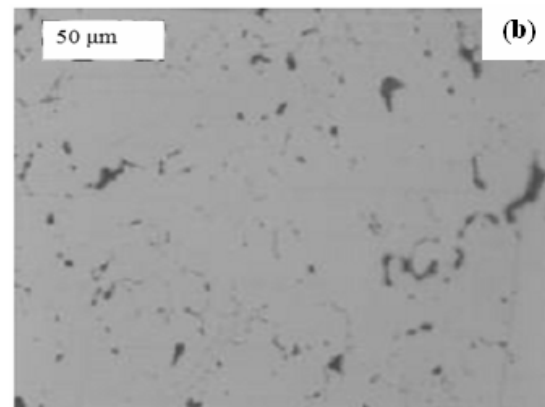
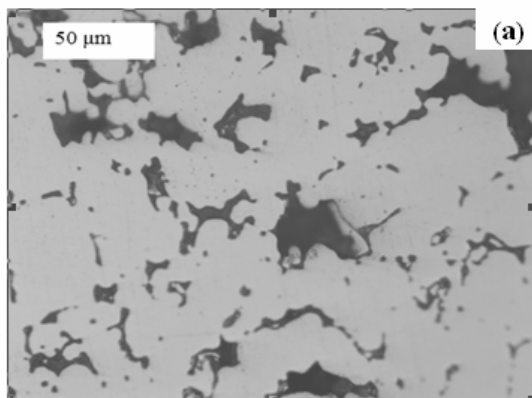


**Fig. 3.** Microstructures of sintered samples: a) P<sub>1</sub>, b) P<sub>2</sub>

## 2.2. Abrasion wear tests

The sintered samples and those subject to steam treatment were tested for abrasion wear test. The SiC particles on the abrasive papers were the size of 80μm and the load applied was 855g. The distance traversed in each case was limited to 150 cycles, corresponding to 76.5 m. The samples were subjected to circular motion over the wheel on which the abrasive paper was stuck.

The abrasion test process included fixing the abrasive paper on the wheel, loading on the machine of the samples of known weight and then applying the load. The samples were cleaned and weighed before and after each test interval. After the tribological tests, the worn surfaces were examined by optical microscope, to identify the characteristics wear mechanisms.

## 2.3. Mechanical properties

The sintered and steam treated samples were analyzed according to their mechanical properties. The microhardness tests were performed by measuring Vickers microhardness, the test parameters are: the penetrator is a diamond pyramid diameter and load of 100g. The microhardness values were the average of three indentations.

## 3. Results and discussion

### 3.1. Microstructure analysis

The microstructures of sintered and steam treated samples were observed by optical microscopy (Olympus BX 50). Figures 3 and 4 show the microscopic analysis of the sintered and steam treated samples. The microstructures reveal the appearance of pores in sintered state and their filling after the steam treatment.

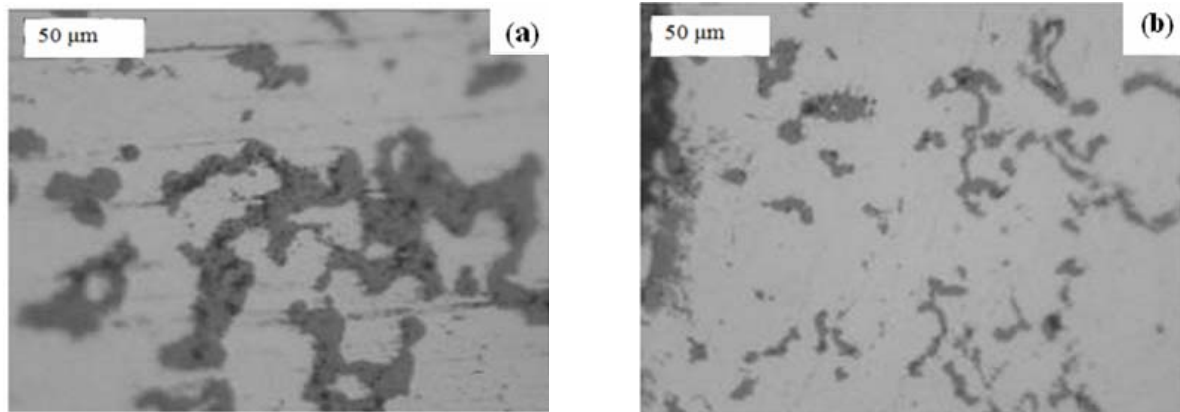


**Fig. 4.** Microstructures of steam treated samples: a) P<sub>1</sub>, b) P<sub>2</sub>

It appears that the iron oxide formed during steam treatment seals the pores at the surface and inside to sintered samples. It was found that the sample of non-alloy powder P<sub>1</sub> presents the best reaction to steam, meaning that its lower density provides a higher pore filling compared to sample P<sub>2</sub>, which is more compact.

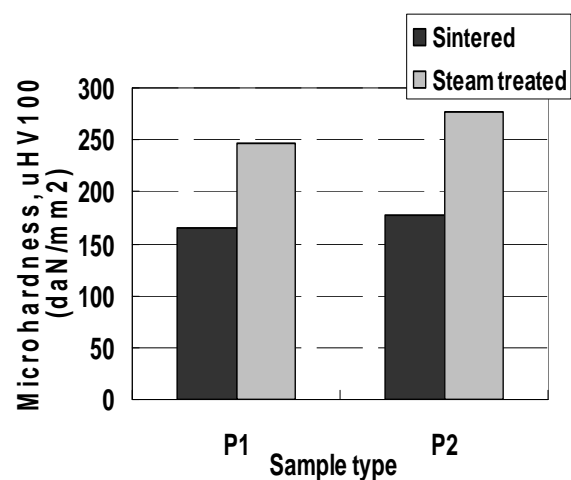
### 3.2. Microhardness values

Figure 5 shows Vickers microhardness values for sintered and steam treated samples.

The microhardness values were the average of three indentations.

It is found that steam treated samples have a difference of approximately 30% in values of Vickers microhardness compared to sintered samples.

This difference results from the high hardness of the induced magnetic iron oxide (Fe<sub>3</sub>O<sub>4</sub>). An increase in hardness was associated with an increase in wear resistance.



**Fig. 5.** Vickers microhardness values for sintered and steam treated samples

### 3.3. Tribological tests

The worn surfaces of sintered and steam treated samples after abrasion tests were examined in optical microscope, the typical aspects of abraded surfaces are represented in figures 6 and 7.

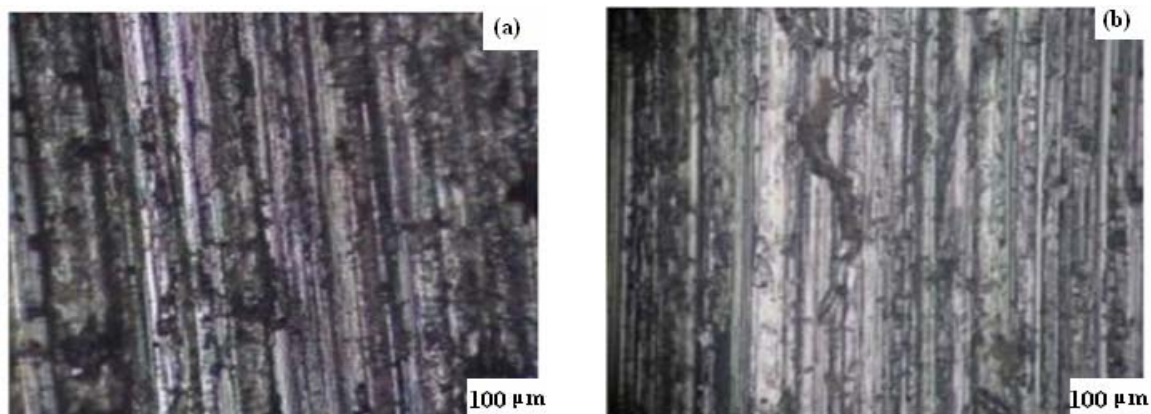


**Fig. 6.** Optical photomicrographs of worn surfaces for sintered samples: a) P<sub>1</sub>, b) P<sub>2</sub>

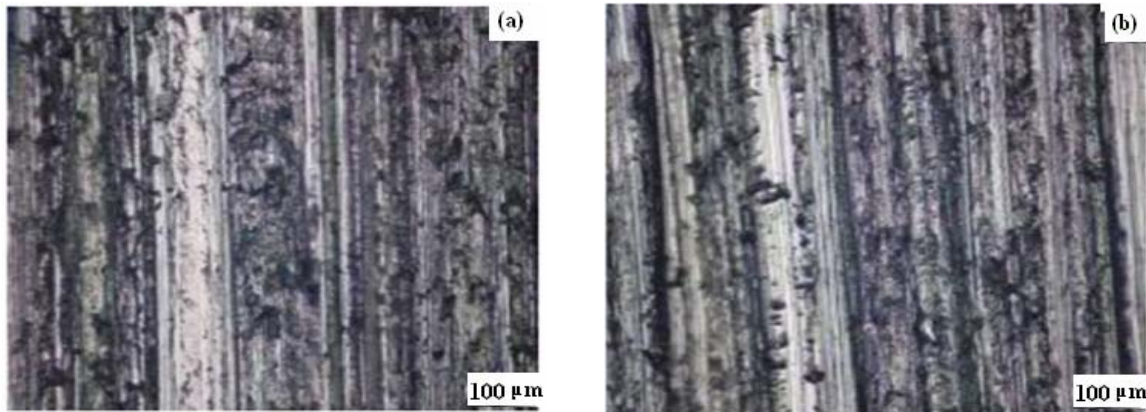


Fig. 7. Optical photomicrographs of worn surfaces for steam treated samples: a) P<sub>1</sub>, b) P<sub>2</sub>

The microscopic analysis of sintered samples subjected to abrasive wear shows that the wear traces are more pronounced for sample P<sub>1</sub>.

This observation is confirmed by the wear loss of the sintered samples. The presence of pores increases the stress concentration around the pores and acts as wear generation and material deformation areas. The wear resistance for steam treated samples results from the high hardness of the induced magnetic iron oxide (Fe<sub>3</sub>O<sub>4</sub>). Also, the oxide layer produced by the steam oxidation is able to perform a lubricating action between the sliding surfaces. For the worn steam treated samples, the depth and width of wear grooves for sample P<sub>1</sub> are greater as compared to those of the samples P<sub>2</sub>.

### 3.4. Wear loss

The wear rates were calculated from the difference in mass of the specimens before and after the tests. The samples were weighed using a precision balance with a sensitivity of 10<sup>-4</sup> before and after each test (Fig. 8), so it was possible to evaluate the wear undergone by the material, the sample P<sub>1</sub> provided the greatest weight loss, in sintered and steam treated state.

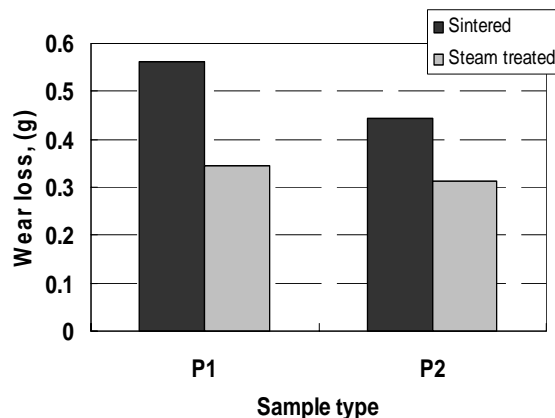


Fig. 8. Mass loss of the sintered and steam treated samples tested to the abrasion test

## 4. Conclusions

The following conclusions can be obtained from this research:

- The microscopic analysis reveals the steam treatment effect on sintered samples by pore filling of iron oxides, mainly the magnetite oxide.

- The wear properties of sintered iron were significantly improved by a steam treatment of 60 minutes and by the addition of copper and molybdenum. The wear resistance for steam treated samples results from the high hardness of the induced magnetic iron oxide (Fe<sub>3</sub>O<sub>4</sub>).

- Abrasive wear surfaces for two types of powders present deeper traces in unalloyed samples and finer trace in samples alloyed P<sub>2</sub>, as subsequently wear tests give results in conformity with these aspects of the surface.

- Sample P<sub>1</sub> presents a depth and width of wear grooves greater, thus there is a possibility of less resistance offered.

- Sample P<sub>2</sub> presents a much smaller wear groove width that can ensure a good resistance.

## References

- [1]. G.B. Jang, M.D. Hur, S.S. Kang - A study on the development of a substitution process by powder metallurgy in automobile parts, J Mater Process Technol (2000): 110–5.
- [2]. V. B. Akimenko, I. A. Gulyaev, O. Yu. Kalashnikova, M. A. Sekachev - The Prospects for Russian Iron Powder, Central Scientific-Research Institute of Ferrous Metallurgy, Vol. 37, No. 5, p. 472–476, (2007).
- [3]. K.S. Narasimhan - Sintering of powder mixtures and the growth of ferrous powder metallurgy. Mater Chem Phys (2001); 67:56–65.
- [4]. Hadrian Djohari, JorgeI Martínez-Herrera, Jeffrey J.Derby - Transport mechanisms and densification during sintering: I. Viscous flow versus vacancy diffusion, Department of Chemical Engineering and Materials Science, MN55455-0132.
- [5]. C. Anayarana C, E. Ivanov, V.V. Boldyrev - The science and technology of mechanical alloying. Mater Sci Eng A, 304–306:151–8, (2001).
- [6]. P. Beiss - Steam treatment of sintered iron and steel parts, Powder Metallurgy, Vol 34, No3, p. 173–177; (1991).



- [7]. **P. Franklin, B.L. Davies** - *The effects of steam oxidation on porosity in sintered iron*, Powder Metallurgy, Volume 20, pages 11–16, (2001).
- [8]. **K. Razavizadeh, B. L. Davies** - *The effects of steam treatment on the wear resistance of sintered iron and Fe-Cu alloys*, Wear, Volume 69, Issue 3, pages 355-367, (1981).
- [9]. **J.D.B. De Mello, I. M. Hutchings** - *Effect of processing parameters on the surface durability of steam-oxidized sintered iron*, Wear, Volume 250, Issues 1-12, pages 435-448, (2001).
- [10]. **J.D.B. de Mello, R. Binder, A.N. Klein, I.M. Hutchings** - *Effect of compaction pressure and powder grade on microstructure and hardness of steam oxidized sintered iron*, Powder Metallurgy, Volume 44, Number , pages 53–61, (2001).
- [11]. **G. Straffelini, D. Trabucco, A. Molinari** - *Oxidative wear of heat-treated steels*, Wear, Volume 250, Issues 1-12, p. 485-491, (2001).
- [12]. **K. Razavizadeh, B.L. Davies** - *Combined Effects of Steam Treatment and Age Hardening on Mechanical Properties of Sintered Fe-Cu Alloys*, Powder Metallurgy, Volume 25, p. 11–16, (1982).
- [13]. **A. Molinari, G. Straffelini** - *Surface Durability of Steam Treated Sintered Iron Alloys*, Wear, Volume 181-183, p 334–338, (1995).
- [14]. **A. Molinari, G. Straffelini** - *Surface durability of steam treated sintered iron alloys*, Wear, Volumes 181-183, p. 334-341, (1995).
- [15]. **S.L. Feldbauer** - *Steam Treating; Enhancing the Surface Properties of Metal Components*; Aabbott Furnace Company; (2003).
- [16]. **A. Molinari, G. Straffelini** - *Tribological Steam Treated Ferrous Parts*, Int. J. Powder Metallurgy, Volume 33, p. 55–62, (1997).
- [17]. **G. Straffelini, A. Molinari** - *Dry sliding behaviour of steam treated sintered iron alloys*, Wear, Volume 159 , Issue 1, p. 127-134; (1992)
- [18]. **W. M. da Silva, R. Binder, J.D.B. de Mello** - *Abrasive wear of steam-treated sintered iron*, Wear, Volume 258, Issues 1-4, p. 166-177, (2005).



## INFLUENCE OF SUBSTRATE TEMPERATURE ON STRUCTURAL AND MORPHOLOGICAL PROPERTIES OF SnO<sub>2</sub> NANOSTRUCTURED THIN FILMS

D.C. VLADU<sup>1</sup>, C. GHEORGHIES<sup>1</sup>, M. BERCEA<sup>2</sup>, I. STOICA<sup>3</sup>,  
M.C. POPESCU<sup>4</sup>, B. BITA<sup>4</sup>, M. BORDEI<sup>5</sup>

<sup>1</sup>Faculty of Sciences and Environment, Chemistry, Physics and Environment Department,  
„Dunarea de Jos” University of Galati, Romania

<sup>2</sup>U. T. Gh. Asachi Iasi, Romania

<sup>3</sup>"Petru Poni" Institute of Macromolecular Chemistry Polymer Materials Physics-Atomic Force Microscopy,  
Aleea Grigore Ghica Voda, 41A, Iasi - 700487, Romania

<sup>4</sup>National Institute for Research and Development in Microtechnologies IMT  
126 A, Erou Iancu Nicolae Street, 077190 Bucharest, Romania

<sup>5</sup>Faculty of Materials Science and Environment, “Dunărea de Jos” University of Galați,  
111, Domnească Street, 800201, Galați, Romania

email: cvladu2010@gmail.com

### ABSTRACT

*SnO<sub>2</sub> nanostructures thin films with thickness of 500 nm were prepared by electron beam-physical vapor deposition on glass substrate at temperature of 300, 373, 443, and 583 K. Structural and morphological properties of these nanostructured thin films were studied by Scanning and Transmission Electron Microscopy (SEM, TEM) and Atomic Force Microscope (AFM) methods. The changes in structural and morphological properties are found at different temperatures. Increase temperature causes important change of the structural and morphological properties. The sample prepared at 300 K has crystalline structure and the sample prepared at 583 K has amorphous structure. Roughness parameters have low values at 300, 373, 443 K as opposed to the values obtained at 583 K. This different behavior may be due to the amorphous structure of the sample that was observed in the TEM analysis.*

KEYWORDS: electron beam-physical vapor deposition, structural, morphological properties, TEM, SEM, AFM

### 1. Introduction

Nanostructures of SnO<sub>2</sub> thin films have been employed in a wide range of applications including solid state gas sensors, liquid crystal displays, transparent conducting electrodes, infrared reflectors, plasma display panels (PDPs), transistors, etc. [1–5].

Among such semiconductors, SnO<sub>2</sub> nanostructured thin films seem to be a good candidate for the solar cell applications (e.g., as a window material) because of their wide band gap (3.6 eV) at room temperature [6–10]. In addition, SnO<sub>2</sub> is useful as a hard film material for applications requiring high refractive and reflective properties. SnO<sub>2</sub> thin films have been prepared by various techniques such as RF-magnetron sputtering [1, 11, 12], electron beam evaporation [13], sol-gel coating [14], chemical

vapor deposition [15], etc. Various characteristics of these SnO<sub>2</sub> films have been observed to change by changing the preparation technique and environment.

Of all the methods, electron beam-physical vapor deposition (EB-PVD) is much preferred for many desirable characteristics such as flexible deposition parameters, low contamination relatively controlled composition, high deposition rates, dense coatings, tailored microstructure [16, 17].

SnO<sub>2</sub> films produced by the EB-PVD process usually have a good surface finish and a uniform microstructure. The versatility of the EB-PVD process is very wide and friendly to environment and new films and materials continue to be developed. In the present study were prepared SnO<sub>2</sub> nanostructured thin films with 500 nm thickness onto glass substrate by EB-PVD at various substrate temperatures.

The influence of substrate temperature on structural and morphological properties of nanostructured SnO<sub>2</sub> thin films were studied using Scanning and Transmission Electron Microscopy (SEM, TEM) and Atomic Force Microscope (AFM).

## 2. Experimental part

SnO<sub>2</sub> thin films were deposited using electron beam evaporation of SnO<sub>2</sub> powder (Sigma Aldrich, purity 99.99%) as a starting material onto high-quality microscope glass substrates using tungsten crucibles. The substrates were chemically cleaned and by glow discharge 30 mA for 6 minutes. The temperature of the glass substrates during the electron beam evaporation was maintained at different values of 300 K, 373 K, 443K, 583 K in order to study the temperature's influence on the properties of the obtained films. The system was pumped to a base pressure of less than 10<sup>-3</sup> Pa before deposition and O<sub>2</sub> was injected into the chamber during evaporation at a partial pressure below 10<sup>-4</sup> Pa. The substrate was set at a distance of 56 cm from the source and rotated at 20 rpm during deposition to obtain uniform and homogeneous films. The deposition parameters were

optimized to reduce the film roughness. Thickness of film and rate of its deposition were controlled with the help of an in situ quartz crystal thickness monitor. Thickness of the film was about 500 nm and the deposition rate was set as 20 Å/sec. The TEM investigation was performed on a Philips CM-120 electronic microscope with an accelerating voltage of 120 kV. The surface morphology for SnO<sub>2</sub> nanostructured thin films was studied by Atomic Force Microscope (AFM, model: Solver PRO-M) and scanning electronic microscope (SEM, model: FEI Nova NanoSEM 630).

## 3. Results and discussion

Selected area electron diffraction (SAED) patterns were taken from a selected area of the SnO<sub>2</sub> thin films. In Fig.1 is shown the SAED pattern of the SnO<sub>2</sub> thin film deposited at substrate temperature of 300 K. The seven intense diffraction rings shown are corresponding to diffraction from (101), (111), (210), (211), (310), (320) and (321) crystallographic planes. The SnO<sub>2</sub> thin film deposited at 300 K exhibits the polycrystalline structure and corresponds to a tetragonal rutile structure.

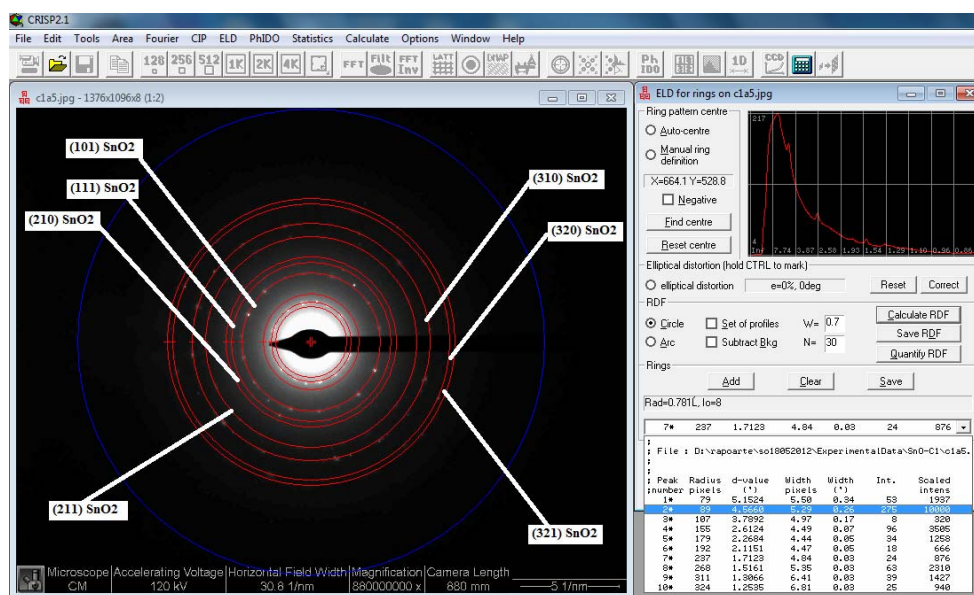


Fig. 1. SAED pattern of the SnO<sub>2</sub> thin film deposited at substrate temperature of 300 K

Fig. 2 shows bright-field transmission electron microscopy (BF-TEM) image recorded from plan view specimen, showing that SnO<sub>2</sub> thin films exhibit a grainy structure which consists of many small grains of relatively uniform size forming a morphologically homogeneous structure.

The size distribution of the crystallites, are plotted in Fig. 3. The distributions of grain sizes, as measured from BF-TEM images, were fitted to the lognormal curves [18, 19]. The mean grain size was

found to be around of 9.48nm. Table 1 shows the average particle size varies with the substrate temperature. Note that the maximum average size of 40.78nm of nanoparticles was obtained at temperatures of 373K.

At a temperature of 300K, the average particle size is the smallest value, i.e. 9.48nm. At temperatures of 443K and 583K, nanoparticles average size decreases to 17.16nm and 13.18nm, respectively.

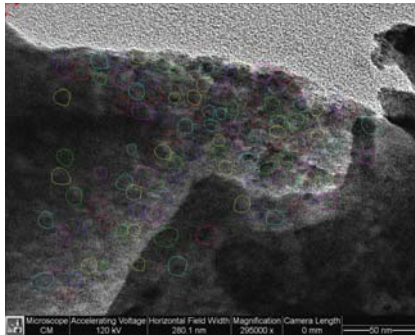


Fig. 2. BF-TEM images of the SnO<sub>2</sub> thin film

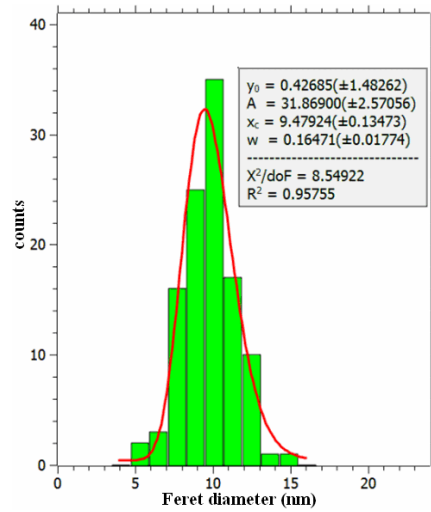


Fig. 3. The distribution curve of the diameters of the crystalline grains of SnO<sub>2</sub> thin films

Table 1. Some characteristics of SnO<sub>2</sub> thin films

Substrate temperature [K]	Film thickness [nm]	Mean grain size [nm]	Grain shape
300	500	9.48	spherical
373	500	40.78	spherical
443	500	17.16	spherical
583	500	13.18	spherical

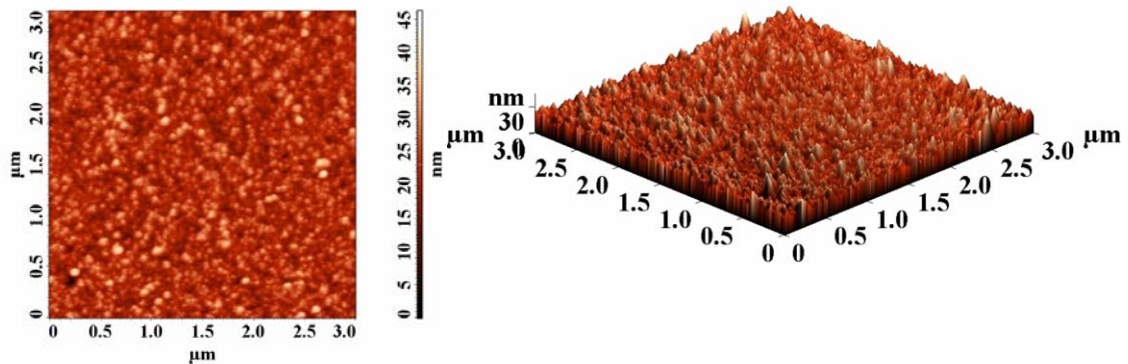
We find that spherical nanoparticles retain all four temperatures [20, 21].

The structure of the thin films is crystalline at a substrate temperature of 300 K, and it is noticed become amorphous at 583 K.

Another method of investigating the structure of SnO<sub>2</sub> nanostructured thin films is atomic force microscopy (AFM). By this method it has been

determined the roughness of the samples studied. Fig. 3 shows 2D and 3D images of SnO<sub>2</sub> samples obtained at temperatures of 300 K (a) 373 K (b) 443 K(c) and 583 K(d) and the 500nm thickness.

Table 2 shows roughness parameters (average roughness, Sa, root square average, Sq) at samples with thickness of 500 nm obtained at temperatures of 300, 373, 443, and 583 K.



a)

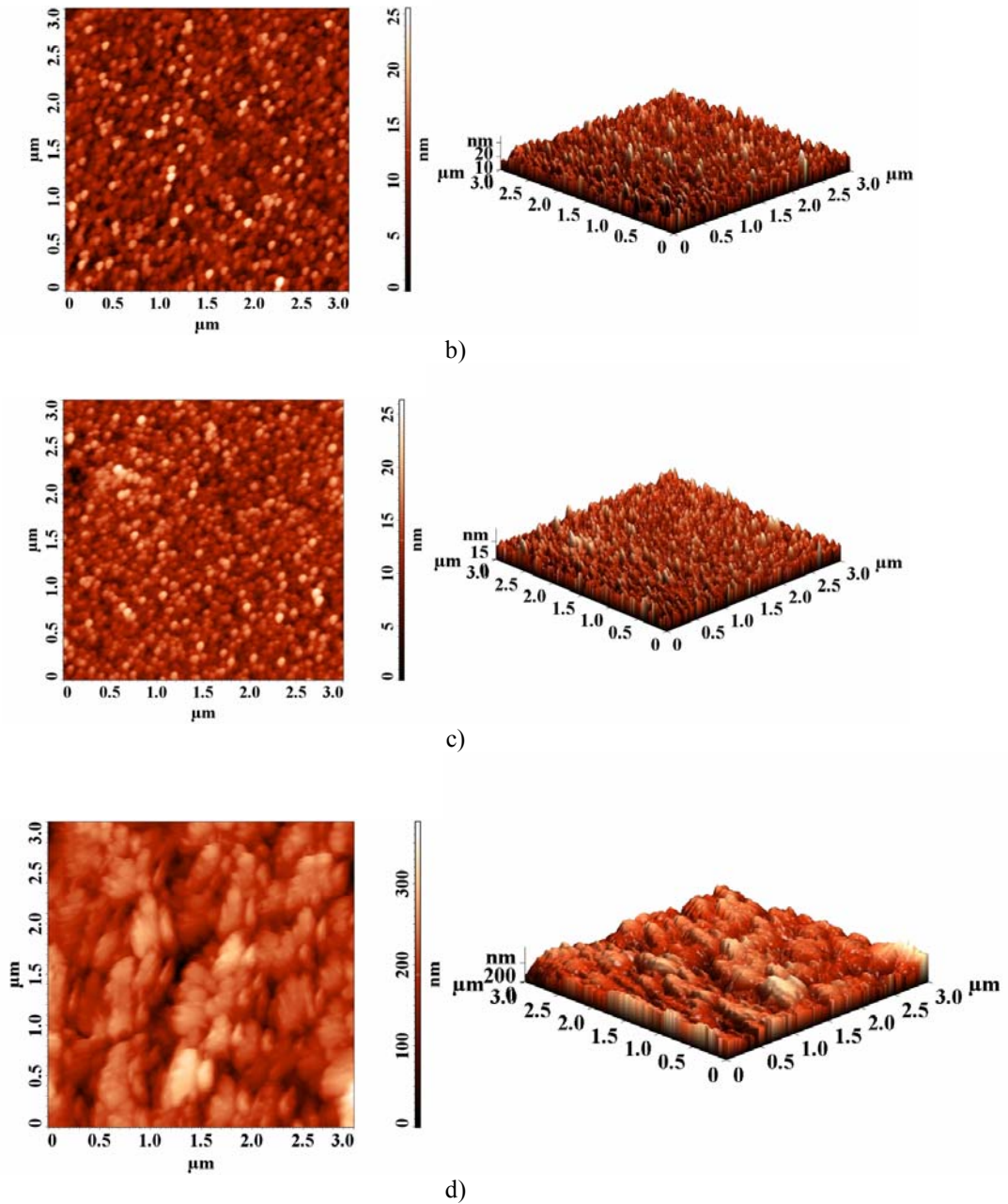


**Fig. 3.** 2D (left) and 3D (right) images of SnO<sub>2</sub> thin films with thickness of 500 nm obtained at temperatures of 300K (a) 373K (b) 443K (c) and 583K (d)

**Table 2** Some roughness parameters of SnO<sub>2</sub> thin films

Substrate temperature [K]	Film thickness	Average roughness, Sa [nm]	Root mean square, Sq
300	500	3.1966	4.06847
373	500	2.31532	2.99308
443	500	2.20535	2.81901
583	500	34.3865	43.9978

Studying the surface topography of SnO<sub>2</sub> thin films thus obtained was found that surface morphology of the substrate is influenced by temperature. Very small values of roughness of SnO<sub>2</sub> nanostructures thin films at temperatures of 300, 373, 443K, and a much increased value at 583K. This different behavior may be due to the amorphous structure of the sample at this temperature, confirmed by the TEM analysis [20, 21].

Because SnO<sub>2</sub> nanostructured thin films have a low electrical conductivity, their research by scanning electron microscopy is difficult. For this reason films were covered with a gold layer with a thickness of 5Å using Edwards AUTO 500 equipment. In this case, the SEM study was performed with an accelerating high voltage of electrons of 10kV and a magnification of 30,000x.

The images presented in fig. 4 show that for the same film thickness of 500nm, deposited layer structure is influenced by the substrate temperature. Thus, Fig. 4a shows the image of a film deposited at 300 K consisting of islands composed of nanoparticles whose size varies between 133.7 to 188.8 nm. At a substrate temperature of 373K, image shown in fig.4b, the coating consists of islands joined together and that includes nanoparticles whose dimensions range from 104.2 to 178.3nm. At a substrate temperature of 443K, Fig. 4c, the thin film tends to appear uniformly encompassing irregular particles of size 133.2-570.3nm arranged disorderly. Films obtained at a support temperature of 583K, fig.4d, are smooth including nanoparticles uniformly arranged with irregular polygonal shapes and sizes of 276.4-660.4nm.

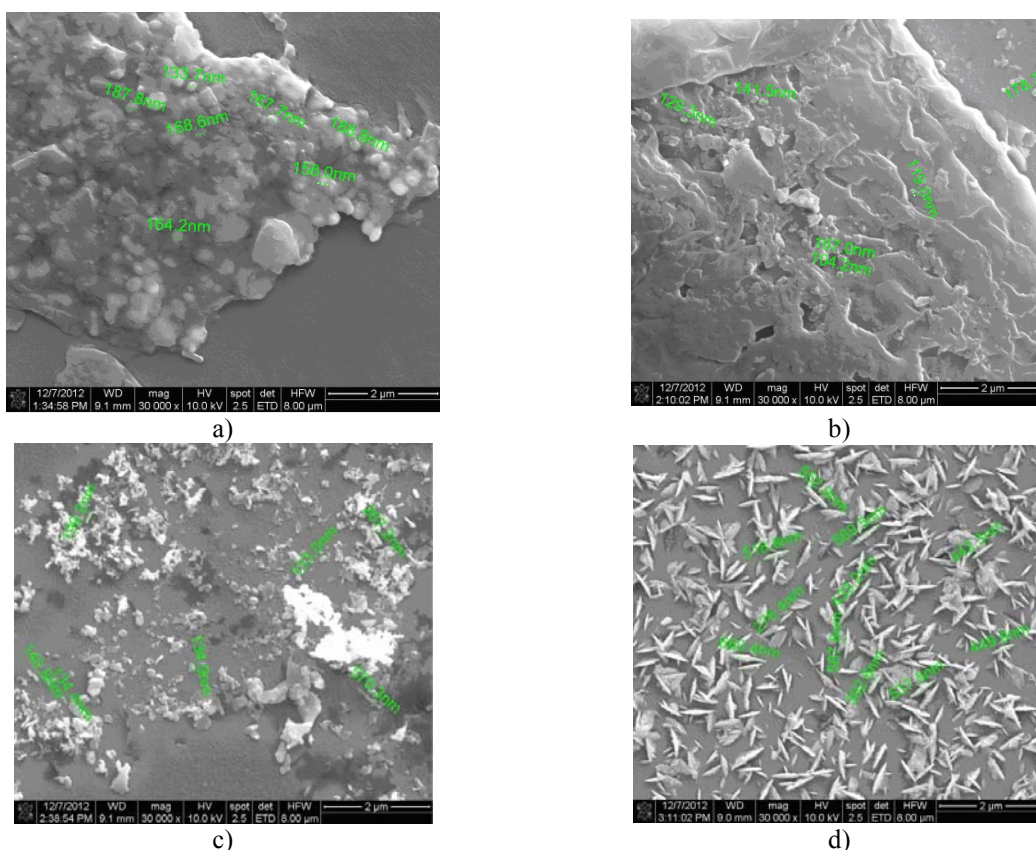


**Fig. 4.** SEM images of SnO<sub>2</sub> nanostructured thin films with thickness of 500 nm obtained at temperatures of 300 K (a) 373 K (b) 443 K (c) and 583 K (d)

#### 4. Conclusions

By EB-PVD method, we prepared SnO<sub>2</sub> nanostructured thin films with thickness 500 nm on glass substrates, at different temperatures of 300, 373, 443 and 583K. We investigated structural and morphological properties of the thin films thus obtained using TEM, AFM and SEM techniques. The sample obtained at 373K has the highest average size

of nanoparticles, 40.78nm, while those obtained at 300K have the lowest average size of nanoparticles, 9.48nm. Nanoparticles have a spherical shape and it is not influenced by the change of the substrate temperature. Roughness parameters show different values to changes in the substrate temperature. The greatest roughness parameters of the SnO<sub>2</sub> thin film corresponding to a support temperature of 583K when the film is in amorphous state.



Structural and morphological properties were studied, proving to be very sensitive to the change of substrate temperature during nanostructuring of SnO<sub>2</sub> thin depositions. The substrate temperature strongly influences the structural and the morphological properties during nanostructuring of SnO<sub>2</sub> thin films, which is in good agreement with literature dates [16-21].

### Acknowledgements

This work was financially supported by the Project SOP HRD - TOP ACADEMIC 76822. The authors gratefully acknowledge Dr. Gabriel Prodan from Ovidius University of Constanta for guidance and TEM measurements.

### References

- [1]. W. Gopel, K.D. Schierbaum - Sens. Actuators B 26 (1995) 1
- [2]. K.L. Chopra, S. Major, D.K. Pandya - Thin Solid Films 102 (1983) 1
- [3]. W.A. Badawy, H.H. Afify, E.M. Elgiar - J. Electrochem. Soc. 137 (1990) 1592
- [4]. A.K. Abbas, M.T. Mohammad - J. Appl. Phys. 59 (1986) 1641
- [5]. G. Sberveglieri - Sens. Actuators B: Chem. 6 (1992) 239
- [6]. A.F. Khan, M. Mehmood, A.M. Rana, M.T. Bhatti, A. Mahmood - Chin. Phys. Lett. 7 (2009) 077803
- [7]. A.F. Khan, M. Mehmood, A.M. Rana, M.T. Bhatti - Appl. Surf. Sci. 255 (2009) 8562
- [8]. I.H. Kim, J.H. Ko, D. Kim, K.S. Lee, T.S. Lee, J.-h. Jeong, B. Cheong, Y.-J. Baik, W.M. Kim - Thin Solid Films 515 (2006) 2475
- [9]. H.J. Kim, J.W. Bae, J.S. Kim, Y.C. Jang, G.Y. Yeom, N.E. Lee - Surf. Coat. Technol. 131 (2000) 201
- [10]. S.G.P. Borojerdian, S.R. Sainkar, R.N. Karekar, R.C. Aiyer, S.K. Kulkarni - Thin Solid Films 295 (1997) 271
- [11]. R. Cavicchi, S. Semancik - Thin Solid Films 206 (1991) 81
- [12]. I.A. Karapatnitski, K.A. Mit, D.M. Mukhamedshina, N.B. Beisenkhanov - Surf. Coat. Technol. 151-152 (2002) 76
- [13]. J.C. Jiang, K. Lian, E.I. Meletis - Thin Solid Films 411 (2002) 203
- [14]. S. Wang, J. Huang, Y. Zhao, S. Wang, S. Wu, S. Zhang, W. Huang - Mater. Lett. 60 (2006) 1706
- [15]. C.F. Wan, R.D. McGrath, W.F. Keenan, S.N. Frank - J. Electrochem. Soc. 136 (1989) 1459
- [16]. N. Tigau, V. Ciupina, G. Prodan, G.I. Rusu, E. Vasile - J. Cryst. Growth 269, 392, 2004
- [17]. M. Huang, Y. Wang, Y. Austin Chang - Thin Solid Films 449, 113, 2004
- [18]. D. E. Wolfe, M. Movchan and J. Singh - *Architecture of Functionally Gradient Ceramic-Metallic Coatings By EBPVD for High Temperature Applications*, Proceedings of Proceeding of Advances in Coating Technologies, at TMS Annual Meeting at Orlando, edited by C. R. Clayton and J. K. Hirvonen (TMS, 1997) p. 93
- [19]. D. E. Wolfe J. Singh and K. Narasimhan - J. Surf. Coat. Techn. 165 (2003) 8
- [20]. Y. Wang, S. Zhang, K. Wei, N. Zhao, J. Chen, X. Wang - Mater. Lett. 60 (2006) 1484
- [21]. H.N. Lim, R. Nurzulaikha, I. Harrison, S.S. Lim, W.T. Tan, M.C. Yeo - Int. J. Electrochem. Sci., 6 (2011) 4329 – 4340.

## CHARACTERIZATION OF SINTERED HARDMETALS COATED WITH TiC

Stela CONSTANTINESCU, Lucica ORAC

"Dunărea de Jos" University of Galați, 111, Domnească Street, 800201, Galați, Romania  
email: [constantinescu\\_stela@yahoo.com](mailto:constantinescu_stela@yahoo.com)

### ABSTRACT

*This paper presents the realization of TiC thin films by CVD method. The thin layers of TiC thicknesses were 8 and 10 $\mu$ m, their thickness increasing with time, keeping the temperature. Diffractometer analysis certifies that this thin layer of TiC is homogeneous and unscratched. Microhardness of thin layers of TiC is  $HV_{0,05} = 30000\text{MPa}$  compared to WC (carbide substrate of the component) that has a microhardness  $HV_{0,05} = 17000\text{MPa}$ .*

KEYWORDS: method, diffractometer analysis, microhardness

### 1. Introduction

Mono-based sintered hardmetals, WC-Co, are mainly used for cutting materials and parts for wear resistant applications.

Chemical Vapor Deposition is a widespread method of forming thin layers. In today's world, it is estimated that 30-40% of all exchangeable cutting plates, sold, are covered by CVD method [1].

Technology of thin films of titanium carbide wear resistant vapor phase followed an original way of achieving titanium tetrachloride directly inside the heat treatment, thus avoiding the import of these tetrachlorides which present a high toxicity. For the ferrotitanium technology with positive results we obtained using ferroalloys with higher concentration

of 65% titanium. Ferrotitanium technology shows economic interest as it eliminates the drawbacks of tetrachloride which is highly corrosive titanium and us instead ferrotitanium.

### 2. Experiments

Titanium tetrachloride vapor is obtained directly in the deposition reactor, the reaction of hydrochloric acid vapors passed over incandescent ferrotitanium (1120<sup>o</sup>C).

Installation of obtaining thin layers of TiC, (Figure 1), includes the following main parts: 1 - sources of Gas; 2- flowmeters; 3 – evaporator; 4- the working chamber; 5, 6 - air purification; 7 - widia plates; 8 - neutralization vessel.

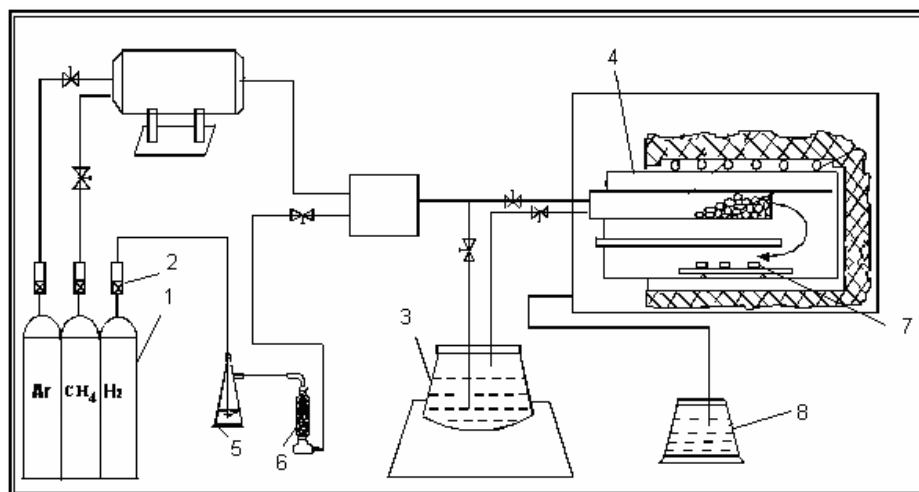


Fig. 1. Installation of obtaining thin layers of TiC

In developing the system layer deposition technology, it occurs the simultaneous deposition on the entire the working chamber, a particular temperature profile combined with a time ratio of the volume of gas in the mixture. This is achieved with a thermocouple and pressure flow meters [2].

Titanium tetrachloride is obtained from rutile, ilmenite, titanium slag, titanium oxide and methane gas according to the reaction:



Reactions being endothermic, require heat entering the system. In this work, titanium tetrachloride is obtained directly in the working chamber of the ferrotitanium and concentrated hydrochloric acid at elevated temperature (over 1000°C) according to the reaction:

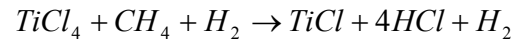
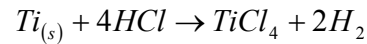


Figure 2 shows the equilibrium diagram Ti-C.

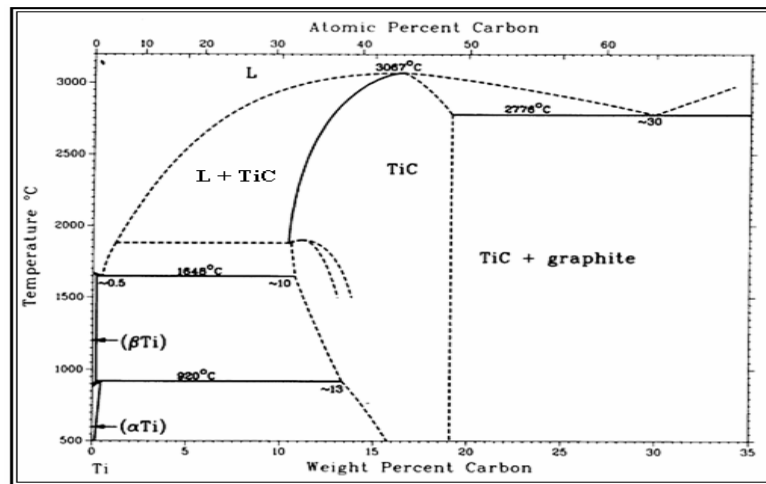


Fig. 2. Diagram of equilibrium Ti-C system, [3]

We can make the following considerations:

- diagram contains narrow areas of solubility of carbon in  $\alpha\text{Ti}$  and  $\beta\text{Ti}$ ;
- titanium carbide (TiC) has a wide range of homogeneity;

- the lower border of the solubility of carbon in TiC eutectic temperature Ti – TiC (1645 °C) [3].

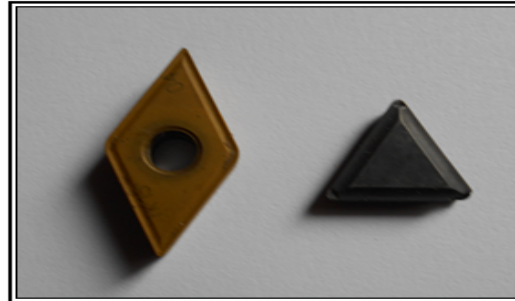
In Table 1 are presented the main characteristics of titanium carbide [4].

Table 1. Properties of TiC carbide

Property	u.a.	TiC
Report ray C/Ti		0.52
Carbon content	%	20.05
Temperature homogeneity range 1750°C	%	11-20
Type and lattice parameters	Å	Cubic a=4.317 Å
Density	g/cm <sup>3</sup>	4.92
Enthalpy of formation of elements $\Delta H_{0298}$	Kcal/mol	-55.3
Standard entropy S <sub>0298</sub>	Kcal/mol	5.8
Entropy training elements $\Delta S_{0298}$	Kcal/mol	-2.92
Specific heat 298..2073 °C	Kcal/mol	$11.83+0.8 \cdot 10^{-3}T - 3.58 \cdot 10^{-5}T^2$
Melting point	°C	3257
The evaporation temperature	°C	4300
Tensile resistance	MPa	0.65
Flexural	MPa	0.15
Compressive strength	MPa	13.8
Modulus of elasticity	MPa	4600
Mineralogical hardness scale	-	8-9
Rockwel Hardness HRA	MPa	9.25- 9.35
Microhardness H <sub>μ</sub>	MPa	317±17

Uncoated (TPUN22.04.08 type P30 and SNUN15.04.08 type K20) and coated plates of TiC were tested, Figure 3. Microstructure of samples

analyzed indicate that they belong to the user group P (WC-Co-TiC) and revealed the presence phases  $\alpha$ ,  $\beta$  and no  $\eta$  phase [5, 6].



**Fig. 3.** The visual appearance of widia plates-type P30 and K20

Figure 4 shows the SEM micrography: a- structure unassailable of alloy with 5% Co and 95% WC and b- structure attacked of alloy with 5% Co and 95% WC. This structure represents the type of structure characterized by the predominance of non-

crystallising tungsten carbide with very fine grains. This type of tungsten carbide is called  $\alpha$  - metastable constituent, whose size grading upward transformation is inevitable during sintering.

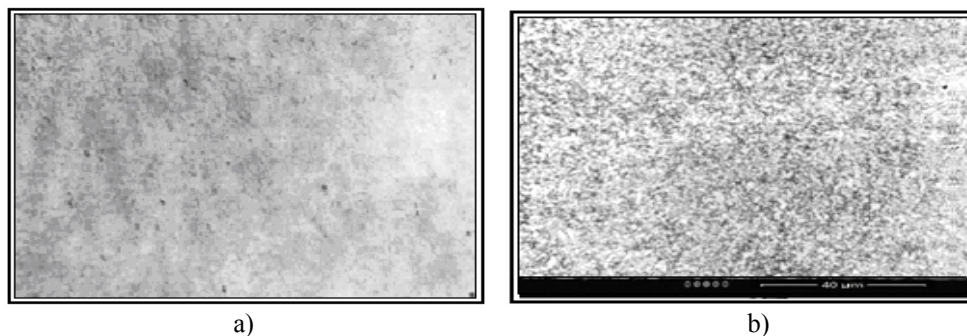


**Fig. 4.** SEM micrography: a - unassailable, b - attacked of alloy with 5% Co and 95% WC, X500

Figure 5 presents the microscopic appearance of the sample in the interface coating-substrate separation and SEM micrograph of TiC surface layer is presented in Figure 6.

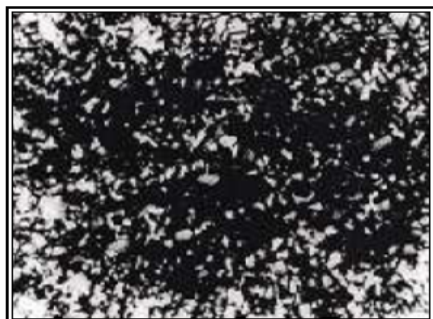


**Fig. 5.** SEM micrograph in the interface coating-substrate separation (attack Murakami, x 2000)

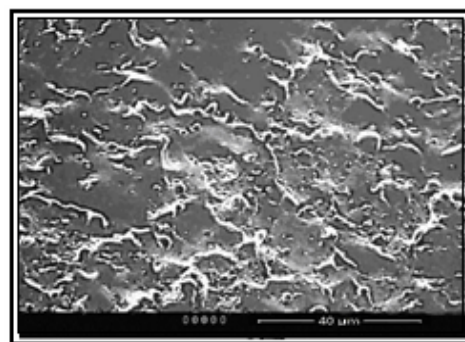


**Fig. 6.** SEM micrograph of TiC, x2000

In Figure 7a is shown thin layer of TiC of 10  $\mu$ m, thickness layer is uniform, homogeneous and adherent throughout its depth and in Figure 7b is presented a diffusion layer by dispersion X ray camera.

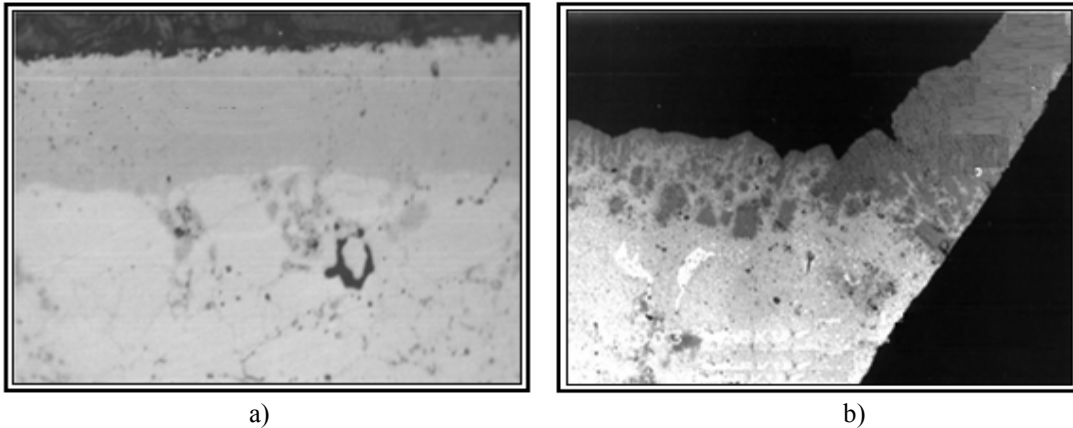


**Fig. 7.** a) SEM micrograph of the TiC layer with a thickness of 10 μm;  
b) Diffusion layer by retrodispersion camera, X 2000

Diffractometer analysis was performed by X-ray diffraction (XRD) on plates coated with thin layers of TiC to working temperature 1120°C. Diffractogram was obtained with a diffractometer equipped with a horizontal goniometer (Figure 8) [7].

XRD spectra were recorded at room temperature and diffractometer using CoK $\alpha$  radiation ( $\lambda=1,79 \text{ \AA}$ ) in  $2\theta$  configuration ranged between 40° and 70°, at 40 kV tension and 30mA current intensity with a scanning speed of 0.02°/min and acquisition time of 1s/step.

The specific lines are tall and narrow, (111) plane corresponds to the angle  $2\theta = 16.5^\circ$ , (220) plane corresponds to the angle  $2\theta = 21.73^\circ$ , and (200) plane corresponds to  $2\theta = 20.25^\circ$ . The result is favorable evidence of TiC layer (the high curves diffractometer).

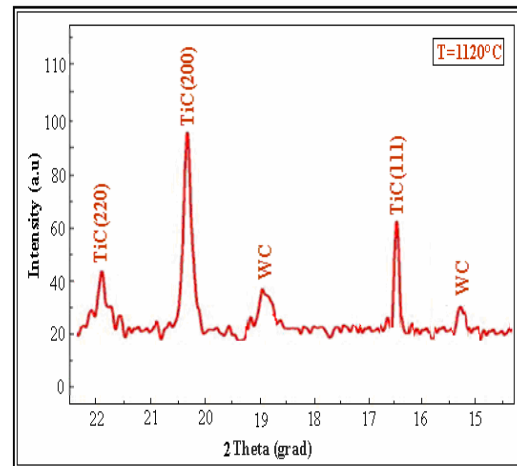


**Fig. 8.** XRD analysis for the thin layer of TiC

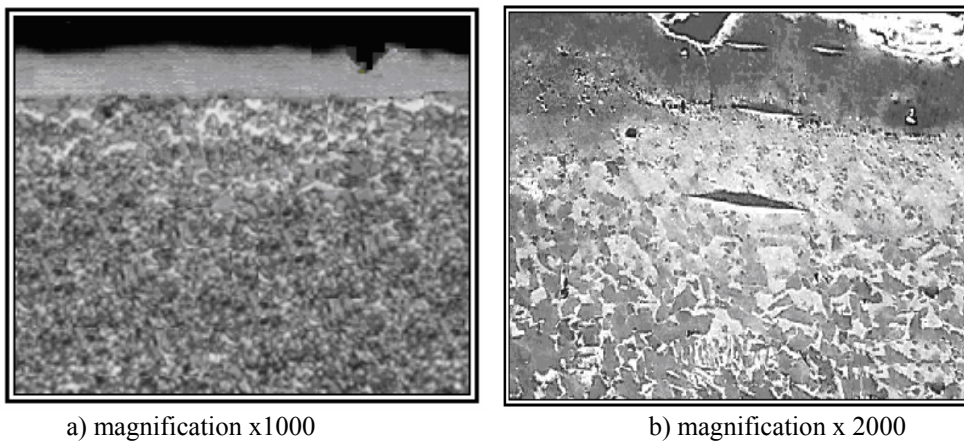


**Fig. 9.** Microhardness deposited layer of TiC - cross section

The results are in agreement with the literature [8, 9].

Layers Microhardness Vickers method was performed by using an optical microscope type M-400-H1 (Hardness Testing Machine) [10]. The

microhardness determinations were carried out on plates coated with thin layers of TiC with thickness of 10 μm.

Microhardness Vickers is not a constant as Vickers hardness, with all geometric similarity of

fingerprints, but generally decreases with increasing test load. [11].

Figure 9 a, b presents microhardness TiC coated plates in cross section at different magnifications and in Figure 10 are presented  $HV_{0,05}$  microhardness prints in the substrate. The microhardness tests show a hardness value of  $HV_{0,05} = 30000$  MPa coated with

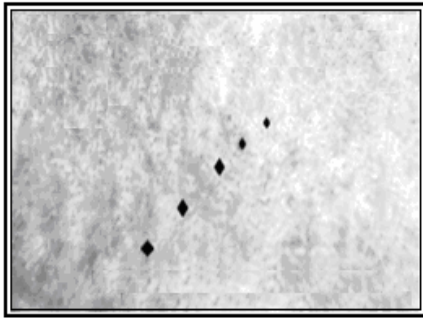


**Fig. 10.** Prints of microhardness  $HV_{0,05}$  in the substrate (magnification  $\times 1000$ )

### 3. Conclusions

- Titanium carbide thin layers obtained by chemical vapor deposition method, followed a realization original titanium tetrachloride directly in the working chamber, thus avoiding import this tetrachloride showing a high toxicity.
- Titanium tetrachloride is given directly the thermal treatment chamber by the use of hydrochloric acid vapors passed over the incandescent ferrotitanium (or pure titanium).
- It was established a substrate temperature of  $\sim 1120^{\circ}\text{C}$  at which TiC can be achieved.
- SEM micrographs have a suitable structure.
- Thickness layer is uniform, homogeneous and adherent throughout its depth.
- The diffractometer analysis is favorable evidences TiC layer.
- The microhardness tests show a hardness value of  $HV_{0,05} = 30000$  MPa coated with TiC layer.

TiC layer, a value that is consistent with data from the literature in relation to the microhardness substrate (95% WC - 5% Co) which is  $HV_{0,05} = 17000$  MPa.

In terms of hardness, there is a strong correlation between Co and hardness of WC-Co alloys, the hardness decreases with increasing cobalt content [12].

### References

- [1]. C. Ciocardia, E. Dragulanesu, I. Dragulanesu - *Sintered Carbide Carbide*, Ed Technique, Bucharest, (1985).
- [2]. V. K. Sarin, *Cemented Carbide Cutting Tools* - Advances in Powder Technology, Ed. D. Y. Chin, ASM, pp. 253-287, 1981.
- [3]. A. T. Santhanam, P. Tierney, and J. L. Hunt - *Cemented Carbides*, Metals Handbook, ASM Int., Vol. 2, 10th Ed. pp. 950-977, 1990.
- [4]. S. Constantinescu, T. Radu - *Advanced methods of obtaining thin coats*, Scientific Publishing F.M.R. ISBN 973-8151-25-2 Bucharest, 2003.
- [5]. Carceanu, M. Chivu, P. Neagu-Manicatile - *New technologies of achievement for cutting tools based cermets, with improved properties*, Third International Conference & Exhibition On Powder Metallurgy RoPM 2005, Cluj Napoca, Proceeding, Vol II ISSN 1221, Sinaia.
- [6]. I. Petrov, P. B. Barna, L. Hultman, J. E. Greene - *Microstructural evolution during film growth*, Journal of Vacuum Science and Technology A 21(5) (2003) S117-S128.
- [7]. A. D. Krawitz - *Introduction to Diffraction in Materials Science and Engineering*, Wiley, New York, 2001, 165-167.
- [8]. J. I. Goldstein, D. E. Newbury, P. Echlin, D. C. Joy, C. Fiori, E. Lifshin - *Scanning Electron Microscopy and X-Ray Microanalysis*, Plenum Press, New York and London, 1981.
- [9]. \*\*\* - *Materials Characterization* 18MB, ASM Handbook, Volume 10 <http://mihd.net/i1mz5k> or <http://depositfiles.com/files/353327>.
- [10]. \*\*\* - *Mechanical Testing and Evaluation*, ASM Handbook Volume 8, <http://mihd.net/s2hvm1> or <http://depositfiles.com/files/353320>.
- [11]. S. Constantinescu - *Properties of hard alloys sintered from metallic carbides*, Tehnomus "New technologies and products in machine manufacturing technologies", Journal no.18, 2011, University Publishing, Suceava, Romania ISSN:1224-029X, p. 245-250, 2011, <http://www.tehnomusjournal.fim.usv.ro>
- [12]. A. C. Fernandes, F. Vaz, L. Cunha, N. M.G Parreira, A. Cavaleiro, L. Goudeau, E. Bourhis, J. P.Riviere, D. Munteanu, B. Borcea, R. Cozma - *The influence of structure changes in the properties of  $TiC_xO_y$  decorative thin-films*, Thin Solid Films 515/2007, p. 5424 – 5429.



## STRUCTURE CHARACTERIZATION OF Ca / Ba, Ca-FeSi INOCULATED, LOW SULPHUR, ELECTRICALLY MELTED, THIN WALL GREY IRON CASTINGS

Lavinia Marilena HARCEA, Iulian RIPOSAN

Politehnica University of Bucharest, 313, Spl. Independentei, RO-060042, Bucharest, Romania  
emails: harcea.lavinia@yahoo.com, riposan@foundry.pub.ro

### ABSTRACT

*Much of the base iron in grey iron foundries is electrically melted in an acid lined induction furnace. The performance of the induction furnace allows superheating above 1500 °C, which is appropriate for thin wall casting production. With higher levels of superheat, the base iron characteristics are totally different from cupola melted iron, resulting in changes to the final casting microstructure. Previous experiments illustrated that eutectic undercooling of this type of base iron is excessively high, demonstrating an increased need for inoculation. The high dissolution rate of residual graphite in superheated iron and difficulties in forming complex (Mn,X)S compounds as active nucleation sites of graphite can be due to very low residuals of Al (< 0.003%) and Zr (< 0.0003%), especially at less than 0.03%S content. This results in increased tendencies for chill and undercooled graphite morphologies, even in inoculated irons. The structural characteristics of low-S (0.025%), low-Al (<0.003%) and 4.0 wt.% carbon equivalent for electrically melted grey irons were studied at different solidification cooling rates in wedge castings up to 20mm wall thickness, using Ca and (Ba + Ca) inoculating elements in FeSi based alloys with the same Si and Al contents. Under these conditions, Ca inoculation had minimal effect at less than 8mm wall thickness, while a Ca-Ba combination improved most of the structural parameters, including those in thin wall castings: less than 10% carbides for 2.5 mm and no carbides at more than 5mm section size, which also showed the highest graphite amount with a uniform distribution over the casting section.*

KEYWORDS: grey cast iron, S, Al, Ca, Ba, inoculation, graphite, carbides, matrix

### 1. Introduction

The study on the efficiency of inoculants used in the production of grey irons aims to design a process that will produce a structure that is commensurate with achieving the target mechanical properties [1]. These are strongly influenced by the components in the structure, or control of graphite morphology and its distribution, the composition of the metal matrix and possibility of defects. The key factor for the production of grey irons with high resistance is represented by the graphite morphology control [2].

Recent research results have identified the graphite nucleation sites as being of the (Mn, X)S - type in commercial grey cast iron. Formation of these complex compounds can be more difficult in electrically melted iron, because of the tendency to

low sulphur content especially if residual Al or Zr are also very low. After the addition of one or more inoculants to the molten iron, the compound (Mn,X)S becomes more complex at a lower ratio Mn/S, which is suitable for the germination of graphite [2-4].

The purpose of this paper is to evaluate the efficiency of Ca-and-Ca,Ba-FeSi alloys for controlling the structural characteristics of 4.0% carbon equivalent [CE], low S (0.026 wt.%S), low Al (0.0015 wt.%Al), typical of electrically melted commercial iron.

### 2. Experimental procedure

For this experiment grey cast iron was melted in a 100kg, 2400Hz frequency, electric induction furnace. The iron was superheated to a temperature of

1484°C and poured into a specially designed furan resin mould.

The mould was designed with a central downsprue, which simultaneously supplied the base iron to four separate test reaction chambers, with one acting as an un-inoculated reference and three to test different inoculation variants [5-7].

In this paper two inoculated irons were compared, one treated with Ca-FeSi alloy and the other with Ca, Ba-FeSi alloy to assess the effectiveness of each inoculant in reducing carbides, and to control the graphite morphology. The effective inoculating elements in the two alloys were Ca and Ca-Ba: Ca-FeSi (wt-%: 73.8Si, 1.02Ca, 0.77Al, Fe-bal) and Ca, Ba-FeSi: (wt-%: 72.6Si, 0.94Ca, 0.96Al, 1.68Ba, Fe-bal). The treatment alloys had a fine grain size (20x80 mesh), specifically for addition of the inoculant into the iron stream. The addition rates of the two selected inoculants in the reaction chamber were evaluated at 0.16 wt.% Ca-FeSi alloy and 0.10 wt.% Ca, Ba-FeSi alloy, respectively.

Sample wedges W<sub>3</sub> (ASTM A367-85, 19x38x100mm, CM = 0.35cm cooling modulus) were connected to the reaction chamber. The wedges were analyzed to establish the structural characteristics of grey iron after inoculation. Plate and cylindrical samples were also cast for other analyses. The design of the ASTM W<sub>3</sub> samples promotes the formation of carbides in the apex area because of the high solidification rate [8].

These samples were fractured, polished and analyzed with a conventional microscope for metallography and an automated image analyzer, on the un-etched and those etched with a 2% Nital solution.

The analyses were performed on both the centreline and along the surface at 1mm depth of the test castings. A higher solidification rate is expected at the casting surface, compared to the central region. The amount of graphite and its morphology (Figure 1), the amount of carbides and the metal matrix features were evaluated.

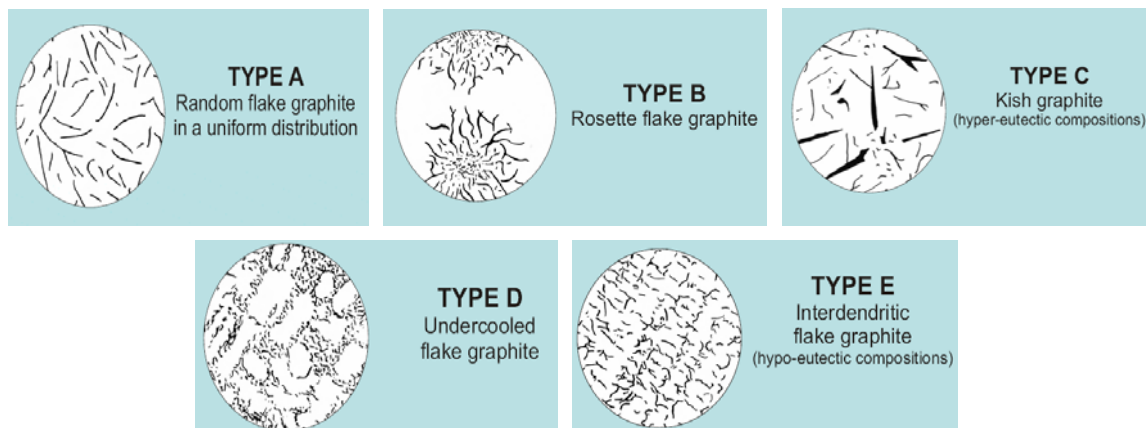


Fig. 1. Typical graphite morphology in grey irons [ASTM]

### 3. Results and discussion

The test iron is characterized by medium levels of C and Si, positioning it close to the eutectic (CE = 4.0%, Sc = 0.93), with low trace elements content, including those known to promote carbides (Tables 1 and 2). A Pearlite factor P<sub>x</sub> [9], commonly used to characterize ductile iron, is mainly influenced by Mn, Si and some micro-elements.

One of the most important characteristic of grey cast iron is the level of and the ratio of the elements Mn and S since these affect the germination of lamellar graphite in commercial irons.

Tables 1 and 2 show critical parameters for iron solidification with low eutectic undercooling, as affected by Mn, S and Al content: (% Mn) x (% S) = 0.01 < 0.03; Al = 0.0015 < 0.005%; Zr = 0.00044% < 0.0005% [2-4].

Table 1. Chemical Composition of Base Iron (wt-%)

<b>C</b>	<b>Si</b>	<b>Mn</b>	<b>P</b>	<b>S</b>	<b>Al</b>	<b>Cr</b>	<b>Mo</b>	<b>Ni</b>	<b>Co</b>	<b>Cu</b>
3.49	1.73	0.382	0.100	0.0258	0.0015	0.048	0.0087	0.0364	0.0045	0.0566
<b>Nb</b>	<b>Ti</b>	<b>W</b>	<b>V</b>	<b>Pb</b>	<b>Sn</b>	<b>As</b>	<b>Zr</b>	<b>Bi</b>	<b>Sb</b>	<b>Te</b>
0.00033	0.0042	0.0066	0.0016	0.0005	0.0041	0.0061	0.00044	0.0011	< 0.0004	0.0016
<b>B</b>	<b>Zn</b>	<b>N</b>	<b>Ca</b>	<b>Mg</b>	<b>Ce</b>	<b>La</b>	<b>Fe</b>			
0.00079	< 0.0001	0.0095	< 0.0002	0.00058	0.0018	< 0.0001	94.1			

*Table 2. Control Factors of Base Iron Chemistry*

Eutectic Range		Mn and S Control		Pearlitic Factor <sup>***</sup> , P <sub>x</sub>	Al Control [min. 0.005%]
Carbon Equivalent* CE, %	Carbon Saturation Degree <sup>**</sup> , S <sub>c</sub>	Mn / S	(%Mn) x (%S)		
4.04	0.93	14.81	0.01	3.83	0.0015

\*CE = C + 0.3(Si + P) - 0.03.Mn + 0.4S; \*\*S<sub>c</sub> = C / C<sub>c</sub> = C / 4.3 - 0.3(Si + P) + 0.03.Mn - 0.4S

\*\*\*P<sub>x</sub> = 3.0 (%Mn) - 2.65 (Si - 2.0) + 7.75 (%Cu) + 90 (%Sn) + 357 (%Pb) + 333(%Bi) + 20.1(%As) + 9.60(%Cr) + 71.7(%Sb) [9.]

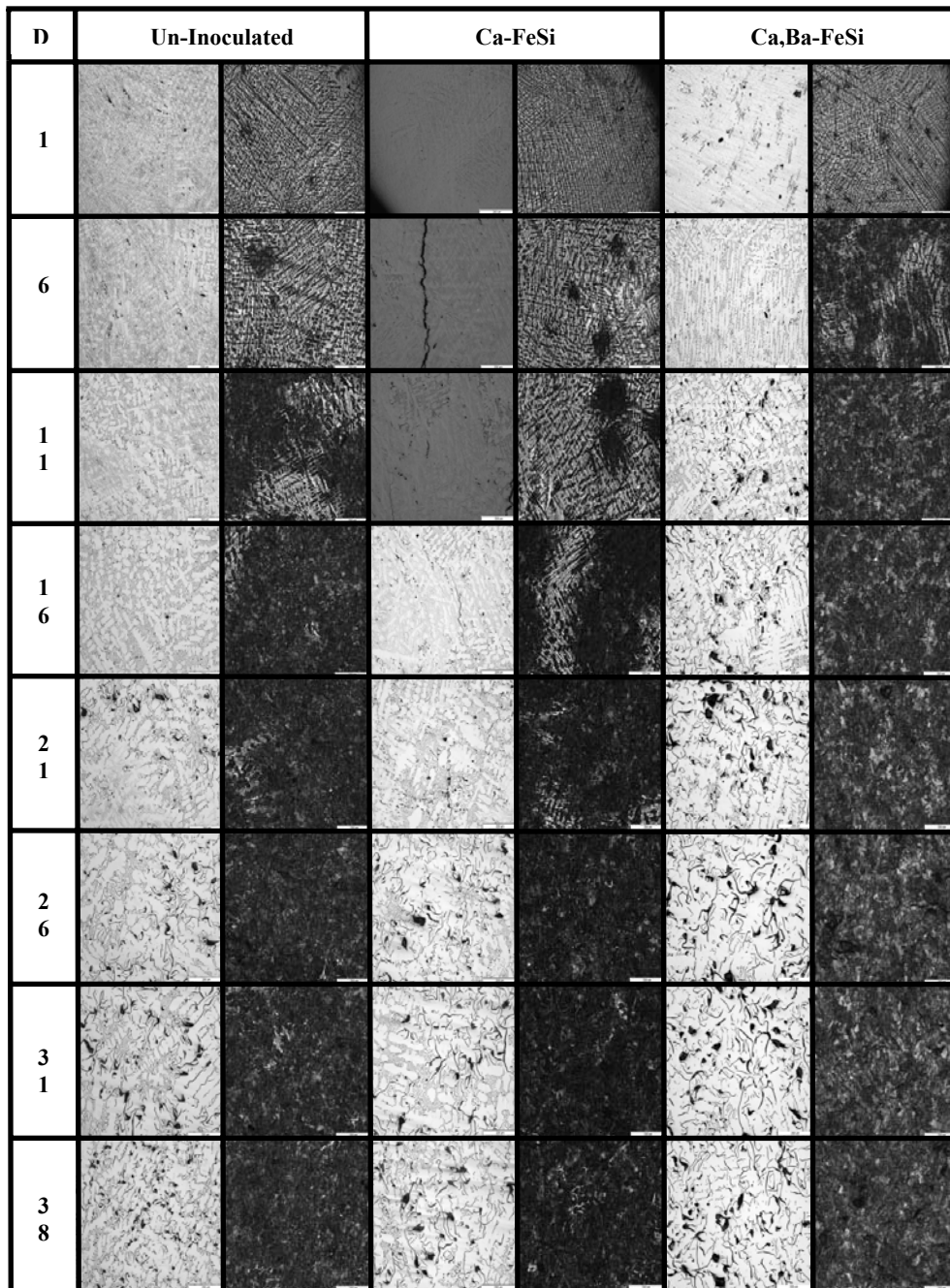


*Fig. 2. Central zone microstructure of W<sub>3</sub> samples at different distance (D, mm) from the apex, for un-inoculated, Ca-FeSi and Ca,Ba-FeSi inoculated irons [un-etched and Nital etched]*

Figures 2 and 3 show the graphite phase and metal matrix characteristics, of un-inoculated and Ca-FeSi or Ca, Ba-FeSi inoculated irons at different distances from the apex of  $W_3$  wedge sample, along

the centreline (Fig. 3) and at the surface (Fig. 4), respectively. At greater distance from the apex sample width increases (section size), and therefore experiences slower cooling rate.

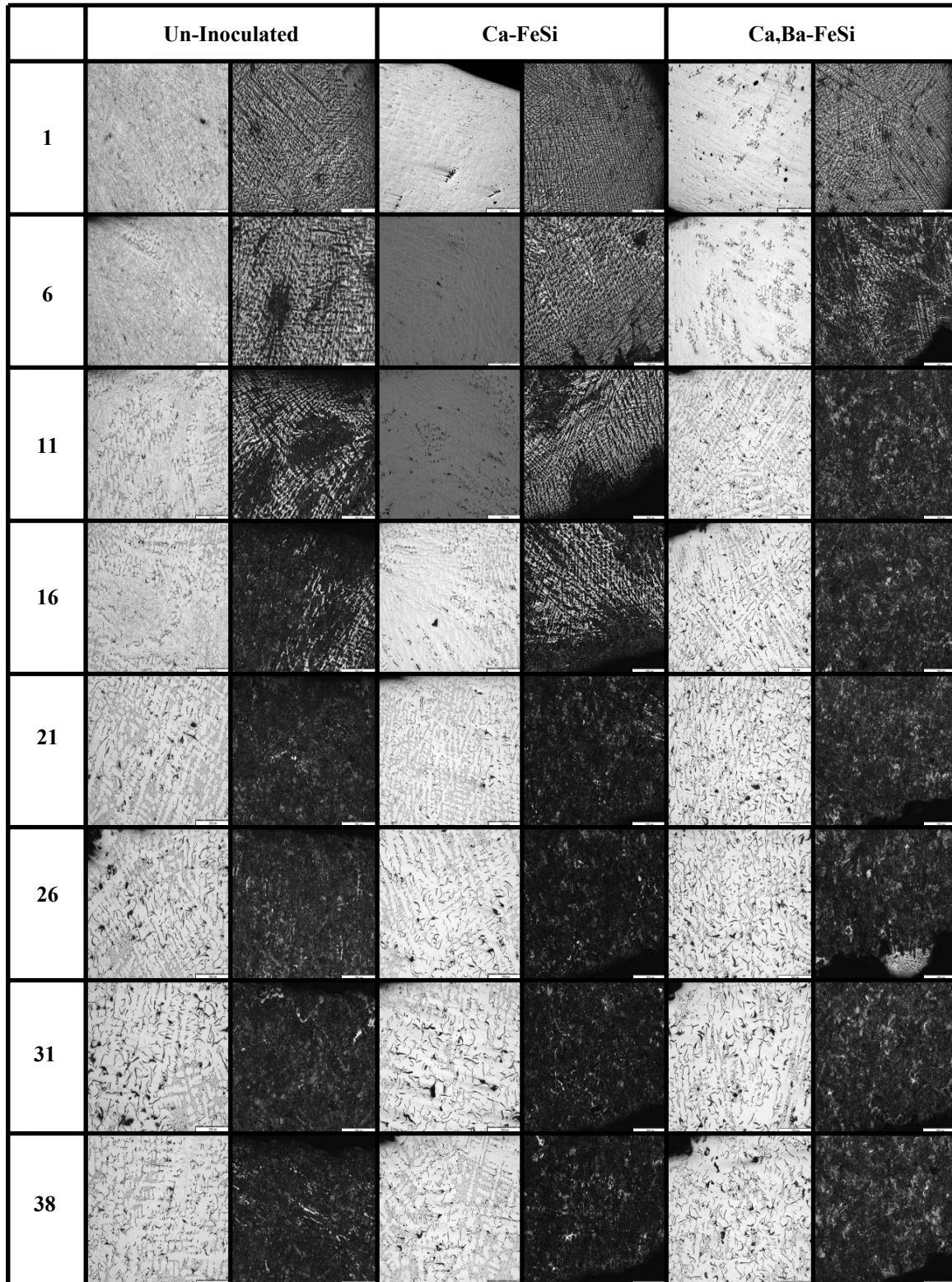


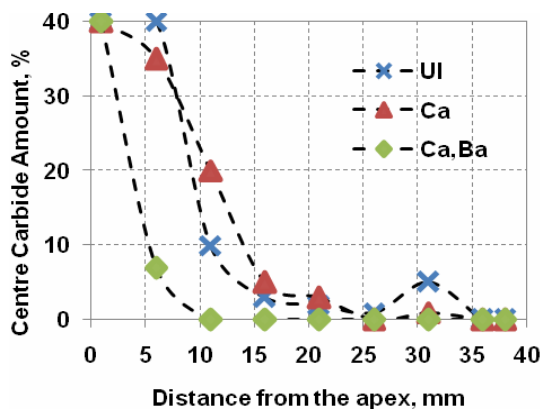
**Fig. 3.** Surface zone microstructure of  $W_3$  samples at different distance ( $D$ , mm) from the apex, for un-inoculated, Ca-FeSi and Ca,Ba-FeSi inoculated irons [un-etched and Nital etched]

The influence of cooling rate or the distance from the apex of the wedge casting, the inoculation treatment and type of inoculating element on the amount of carbides and graphite, and undercooled graphite ratio were the focus of this evaluation. Avoiding both carbides and undercooled graphite morphologies (B, D, E), resulting in the preferred Type A, graphite formation is the most important objective of inoculation in grey cast iron production. Generally, well inoculated grey irons are characterized by Type A graphite nucleation with low eutectic undercooling, usually at more than 25 °C above the metastable (carbide) eutectic equilibrium temperature ( $T_{mst}$ ). As undercooling increases and the start of graphite nucleation is closer to  $T_{mst}$ , the graphite will branch, forming abnormal patterns. These shapes are known as Types B, D and E graphite. A further increase in undercooling will suppress the formation of graphite, resulting in a hard and brittle white iron, carbide structure, with very poor machinability. An inverse relationship exists between the level of free carbides and distance from the apex of the chill wedge, and the wedge width, respectively. The risk of carbides is lower with increasing wedge width, but is dependent on whether the state of the iron is as base iron or inoculated iron.

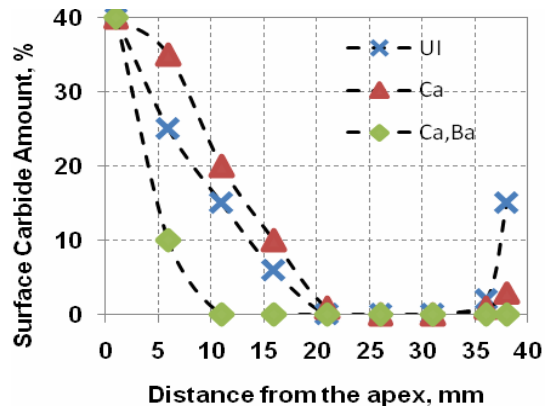
The effect from inoculation was able to eliminate free carbides formation at more than 26 mm distance from the apex (13 mm wall thickness) for Ca-FeSi inoculated iron and at 10 mm distance (5mm section size) for Ca, Ba-FeSi treatments, in the centreline area of the wedge castings. As expected, the surface area of these castings is more likely to see metastable solidification conditions and free carbides formation.

Additionally, the end effect [8] is more visible, especially for un-inoculated iron. Ca-bearing FeSi alloy limited this effect, but only Ca, Ba-FeSi inoculation avoided it. Ca, Ba-bearing FeSi alloy appears to be more effective especially for thin wall castings (less than 5mm section size), despite the critical chemical composition. The conventional inoculant Ca-FeSi does not achieve a clear effect of limiting the carbides at high solidification rates (Figure 4). The amount of graphite formed is related inversely to the variation in amount of carbides, (Fig. 4c and 4d).

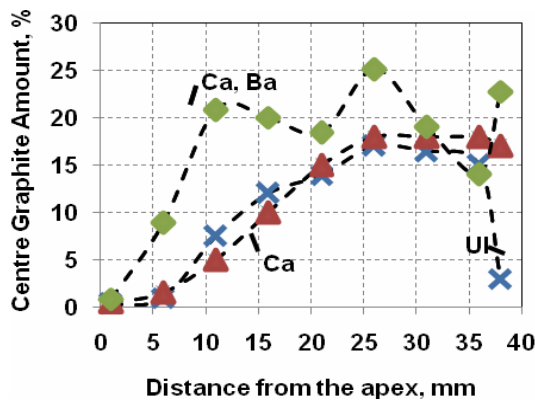
At greater distance from the apex (increased section size = lower solidification rate), normally leads to a higher amount of graphite, but it depends on the state of the iron as well as which inoculating elements are employed.



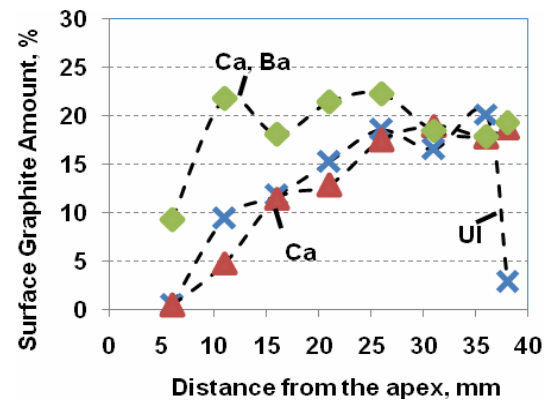
(a)



(b)



(c)



(d)

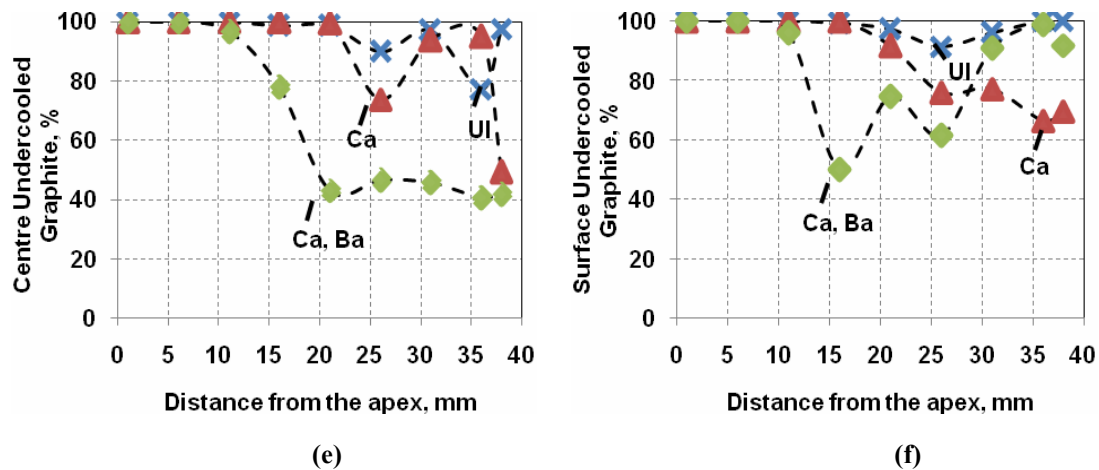


**Fig. 4.** Influence of cooling rate and inoculation on the carbide amount (a,b), graphite amount (c,d) and undercooled graphite ratio (e,f) at different distances from the apex of  $W_3$  – ASTM A387 wedge casting

Ca, Ba-FeSi inoculation led to the highest amount of graphite, reflecting the lowest level of carbides, whereas Ca bearing FeSi alloy inoculation had a limited effect in these experimental conditions.

Undercooled graphite morphologies, including B, D and E type graphite (Fig. 1) are seen to be affected by cooling rate, iron treatment and inoculant type (Figs. 4e and 4f). Un-inoculated iron typically has the highest amount of these inferior graphite morphologies, with 100% presence up to 10mm section size, and more than 90% for the larger wedge casting sections, for both analyzed areas (centreline and surface). Ca-bearing FeSi was only effective above 10mm section size, decreasing the undercooled graphite up to 70%. Ca, Ba-FeSi inoculation had a stronger effect, as the undercooled graphite ratio decreased above 5mm section size by up to 40% in the centre areas and by 60% at the surface area of wedge castings.

Ca is considered the base inoculating element, while Ba is known as a strong promoting element that prolongs the effect of graphite germination. Combination of the two inoculating elements shows a beneficial effect on low sulphur irons [10]. Ca, Ba-FeSi alloy is more efficient in reducing carbides and undercooled graphite both at the centre and the casting surface compared to Ca-FeSi inoculant, which was less able to limit undercooled graphite and carbide formation. Ca and Ba inoculated iron had a uniform distribution of graphite over the whole surface of the sample with relatively small differences between the two central and marginal areas. Despite the relatively high carbon equivalent ( $CE = 4.0\%$ ), the experimental irons develop iron carbides and an undercooled graphite morphology during solidification. As expected, the un-inoculated iron contained a large number of carbides with a small

amount of graphite, most of which was present as undercooled graphite (more than 90% of the sample).

The pearlite / ferrite ratio is determined not only by the solidification rate and later, the cooling rate, but also by the graphite phase characteristics, which influence carbon diffusion during the eutectoid reaction. Normally at higher cooling rate (close to the apex of the wedge casting, equivalent to thinner section), there is a higher pearlite/ferrite ratio. However, undercooled graphite morphologies formed during eutectic solidification, as a result of higher eutectic undercooling, typical of high cooling rates, will also influence the later eutectoid transformation when the iron is 100% solid: increased carbon diffusion is easier because of the shorter distance between graphite particles. This creates a local zone in the matrix with sufficiently lower carbon content to allow ferrite formation, even if free carbides are present (mottled iron structure).

#### 4. Summary

(1) The study confirmed that low-S (0.025%), low-Al (<0.003%) and low-Zr (<0.0005%) electrically melted base iron superheated to 1484 °C, with a  $(\%Mn) \times (\%S) < 0.03$  control factor, is highly prone to free carbides and undercooled graphite formation, even at high carbon equivalent ( $CE=4.0\%$ ), for thin wall castings.

(2) A conventional Ca-bearing FeSi inoculant, added at the lower amount for an in-mould treatment technique (0.16 wt-%) had a limited graphitizing capacity, and only above 10 mm section thickness in the test castings.

(3) Despite adding 40% less in the reaction chamber than Ca-FeSi alloy, Ca,Ba-FeSi alloy was more effective than the Ca-FeSi reducing carbides formation, down to a 5mm section size.



(4) Both inoculant variants showed a limited performance to avoid undercooled graphite formation, with Ca,Ba-FeSi inoculant outperforming Ca-FeSi.

(5) A more effective inoculation treatment is necessary to control both carbides and undercooled graphite formation, especially for castings with less than 5 mm section size.

### Acknowledgement

The work has been funded by the Sectoral Operational Programme Human Resources Development 2007-2013 of the Romanian Ministry of Labour, Family and Social Protection through the Financial Agreement POSDRU/107/1.5/S/76903. The authors would like to recognize and thank Dr. Rod Naro, ASI International Ltd, for partially supplying funding for the experiments and Michael Barstow (Consultant) for reviewing and editing this paper.

### References

- [1]. **D. M. Stefanescu** - *Properties and Selections: Irons, Steels and High-Performance Alloys*, ASM Handbook, Vol.1 (1990), pp. 3-11.
- [2]. **I. Riposan, M. Chisamera, S. Stan, D. White** - *Complex (Mn,X)S compounds—major sites for graphite nucleation in grey cast iron*, China Foundry, 2009, **6** (4), pp. 352-357.
- [3]. **I. Riposan, M. Chisamera, S. Stan, T. Skaland** - *Graphite Nucleants (Microinclusions) Characterization in Ca/Sr Inoculated Grey Irons*, Int. J. Cast Met. Res., 2003, **16** (1-3), pp. 105-111.
- [4]. **I. Riposan, M. Chisamera, S. Stan, C. Hartung, D. White** - *Three-Stage Model for the Nucleation of Graphite in Grey Cast Iron*, Mater. Sci.Techn., 2010, **26** (12), pp. 1439-1447.
- [5]. **M. Chisamera, I. Riposan, S. Stan, C. B. Albu, C. Brezeanu, R. L. Naro** - *Comparison of Oxy-sulfide Alloy Tablets and Ca-bearing FeSi75 for Late Inoculation of Low Sulfur Grey Irons*, AFS Trans., 2007, **115**, pp. 481-493.
- [6]. **S. S. Ojo, I. Riposan** - *Alloy selection for in the mould inoculation to control chill in ductile iron*, Mater. Sci. Techn., 2010, **28** (5), pp. 576-581.
- [7]. **L. M. Harcea, I. Riposan** - *Chill sensitivity in 4.0% carbon equivalent, low-S, inoculated grey iron in thin wall castings*, Metal. Int., 2013, **18** (Special Issue 6), pp. 99-104.
- [8]. **S. Stan, M. Chisamera, I. Riposan, E. Stefan, M. Barstow** - *Solidification Pattern of Un-inoculated and Inoculated Gray Cast Irons In Wedge Test Samples*, AFS Trans., 2010, **118**, pp. 295 – 309.
- [9]. **T. Thielman** - *Zur Wirkung van Spurenelementen in Gusseisen mit Kugelgraphit*, Giessereitechnik, 1970, No.1, pp. 16-24.
- [10]. **M. Chisamera, S. Stan, I. Riposan, G. Grasmio, C. Hartung** - *Structure Characteristics of Ba/Ca/Sr inoculated hypoeutectic grey cast irons*, Int. J. Cast Metal. Res., 2011, **24** (6), pp. 363-369.



## CORROSION BEHAVIOR OF SOME MATERIALS IN 0.5 M AMMONIUM HYDROXIDE SOLUTION

Gina ISTRATE, Florentina POTECAȘU,  
Vasile BAȘLIU

"Dunărea de Jos" University of Galați, 111, Domnească Street, 800201, Galați, Romania  
email: gina.nastase@ugal.ro

### ABSTRACT

*The present work has the purpose of studying metallographic aspects and corrosion resistance of three materials used in ammonia stripping plants. The corrosion process was evaluated by gravimetric tests and potentiodynamic method. Materials tested were Al 1050 (99.5%Al), stainless steel AISI 316Ti and low alloy steel P235TR2. To determine gravimetrically the rate of penetration, samples were immersed in corrosive environment for 294 days and weighed periodically. As test solution 0.5 M ammonium hydroxide (specific for coke industry) was used in a three electrode open cell with material tested as working electrode (WE), a platinum electrode as counter electrode (CE) and an Ag/AgCl electrode as reference electrode (RE).*

KEYWORDS: corrosion, ammonium hydroxide, penetration index

### 1. Introduction

Corrosion process plays an important role in the field of economics and safety. Various types of materials are included in different industries (chemical and electrochemical industries, medical, nuclear, petroleum, power, and food production), and also in daily life.

In the stripping plants were used the following materials: aluminium Al 1050, stainless steel 316Ti and low alloy steel P235TR2.

The high affinity of aluminium for oxygen enables them to develop oxide films at room temperature and these films possess excellent adhesion, continuity and corrosion resistance properties. In atmospheres of low or moderate corrosivity, aluminium behaves as a passive material, but the insignificant corrosion that takes place is sufficient to deteriorate its appearance [1]. The corrosion behavior of commercial aluminium alloys was studied in many aqueous chemical environments [2-11]. Type 316Ti stainless steel has been widely used as sheet and tube materials in the chemical industry and nuclear power industry. Up to now, various environments have been investigated and reported for materials used in the circuit piping system and should be cautiously considered for purposes of safe operations and managements as well as remaining life assessment of different plants, among which corrosion is of great importance [12-

16]. Corrosion behavior of low-alloy steel was investigated in many environments [17-24].

### 2. Experimental procedure

For weight loss measurements, the samples of materials (AISI Al 1050 (99.5%Al), stainless steel AISI 316Ti and low alloy steel P235TR2) were abraded with different emery papers (grade 800, 1000 and 1200), washed with double distilled water, rinsed with ethanol and acetone, and then dried at room temperature. After weighing accurately, the specimens were immersed in beakers containing 250mL of 0.5 M ammonium hydroxide solution, at 25° C. After each immersion time, the specimens were taken out, washed, dried, and weighed accurately. In order to obtain good reproducibility, experiments were carried out in triplicate.

The corrosion rate ( $V_{corr}$ ) and penetration index (P) were calculated from the following relations:

$$V_{corr} = \frac{\Delta m}{S \cdot t} [g \cdot m^{-2} \cdot h^{-1}] \quad (1)$$

where:  $\Delta m$  is the weight loss values, S is the total area in  $m^2$  and t is the immersion time in h, and

$$P = \frac{24 \cdot 365 \cdot V_{corr}}{1000 \cdot \rho} \quad (2)$$

$V_{corr}$ —corrosion rate, [ $g \cdot m^{-2} \cdot h^{-1}$ ];  $\rho$  - density, [ $g \cdot cm^{-3}$ ].

Potentiodynamic polarization measurements were conducted using a VoltaLab-PGP-201.

A conventional cylindrical glass cell of 250mL with three electrodes was used. A platinum sheet of 2cm<sup>2</sup> area and Ag/AgCl electrode ( $E_{Ag/AgCl} = +200$  mV/ENH) were used as auxiliary and reference electrodes, respectively.

The working electrode was embedded with epoxy except for the working surface.

Potentiodynamic polarization curves were obtained by varying the potential automatically from -300 to +300mV against the open circuit potential (OCP) with the scan rate of 2mVs<sup>-1</sup> starting one hour after immersion of the working electrode into the test solution.

### 3. Results and discussion

In Figures 1-3 is shown the weight loss for the studied materials.

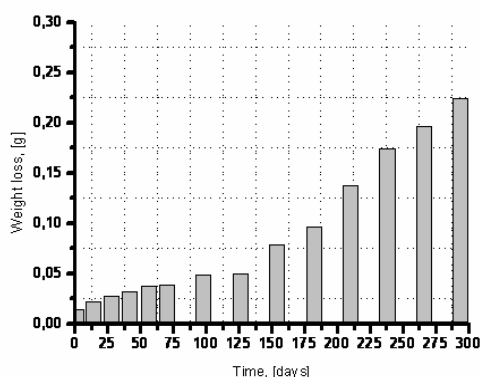


**Fig. 1.** Weight loss vs. exposure time to corrosive environment NH<sub>4</sub>OH 0.5M for Al 1050

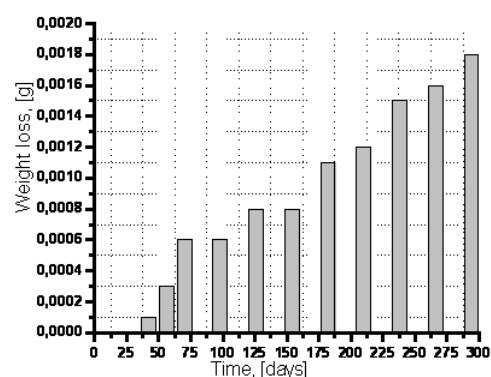


**Fig. 2.** Weight loss vs. exposure time to corrosive environment NH<sub>4</sub>OH 0.5M for 316Ti

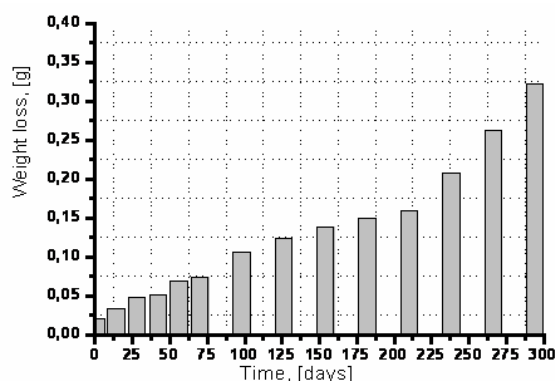


**Fig. 3.** Weight loss vs. exposure time to corrosive environment NH<sub>4</sub>OH 0.5M for P235TR2

The values of the corrosion rate were obtained from weight loss measurements using Eqs. (1) at 25°C and were listed in Table 1.

**Table 1.** Corrosion rate

Sample	Al 1050	316Ti	P235TR2
<b>Time [days]</b>	<b>Corrosion rate</b>		
	$V_{cor} = \Delta m / (S \cdot t) \quad [g/m^2 \cdot h]$		
1	$356.167 \cdot 10^{-3}$	0	$555.555 \cdot 10^{-3}$
14	$39.032 \cdot 10^{-3}$	0	$64.682 \cdot 10^{-3}$
28	$24.307 \cdot 10^{-3}$	0	$46.626 \cdot 10^{-3}$
42	$18.528 \cdot 10^{-3}$	$196 \cdot 10^{-6}$	$33.664 \cdot 10^{-3}$
56	$16.205 \cdot 10^{-3}$	$442 \cdot 10^{-6}$	$33.928 \cdot 10^{-3}$
70	$13.452 \cdot 10^{-3}$	$708 \cdot 10^{-6}$	$29.166 \cdot 10^{-3}$
98	$12.247 \cdot 10^{-3}$	$506 \cdot 10^{-6}$	$29.875 \cdot 10^{-3}$
126	$9.680 \cdot 10^{-3}$	$524 \cdot 10^{-6}$	$27.226 \cdot 10^{-3}$
154	$12.403 \cdot 10^{-3}$	$429 \cdot 10^{-6}$	$24.855 \cdot 10^{-3}$
182	$12.867 \cdot 10^{-3}$	$499 \cdot 10^{-6}$	$22.741 \cdot 10^{-3}$
210	$15.949 \cdot 10^{-3}$	$472 \cdot 10^{-6}$	$21.137 \cdot 10^{-3}$
238	$17.845 \cdot 10^{-3}$	$521 \cdot 10^{-6}$	$24.159 \cdot 10^{-3}$
266	$18.066 \cdot 10^{-3}$	$497 \cdot 10^{-6}$	$27.474 \cdot 10^{-3}$
294	$18.603 \cdot 10^{-3}$	$506 \cdot 10^{-6}$	$30.432 \cdot 10^{-3}$

From the graph shown in Figure 4 it can be seen that samples Al 1050 - 1 day of immersion has a high penetration index of 1155 mm/year thereafter greatly decreases averaging  $50 \cdot 10^{-3}$  mm/year.

In Figures 4-6 are shown the values of penetration index for the studied materials, calculated with relation 2.

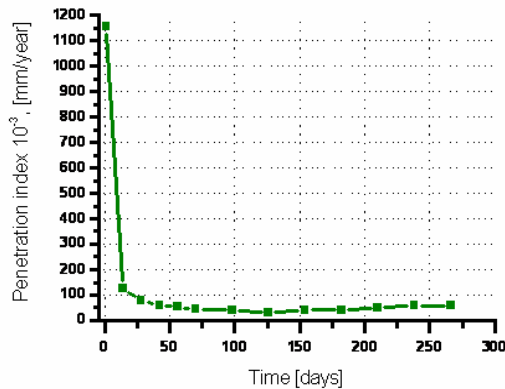


**Fig. 4. Penetration index vs. time for Al 1050**

This shows that the sample surface was covered with a layer of aluminum oxide which greatly reduces the corrosion rate.

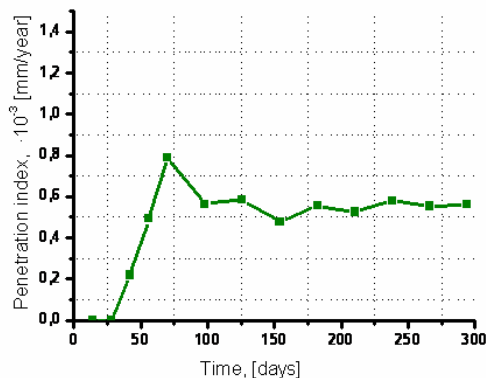


**Fig. 5. Penetration index vs. time for 316Ti**

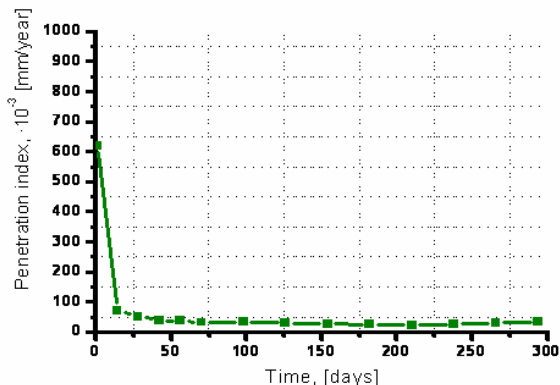


**Fig. 6. Penetration index vs. time for P235TR2**

From the graph shown in Figure 5 we can see that samples from 316Ti present the first weighing, zero mass loss, only at 42 – day, they show a weight loss of  $1 \cdot 10^{-4}$ g, and until the end of the analysis the average penetration index of  $500 \cdot 10^{-6}$  mm/year.

Corrosion of gravity detected in 0.5M  $\text{NH}_4\text{OH}$  was evidenced by metallographic analysis on the surface of the sample subject to corrosion during a period of 294 days. In Figures 7-9 are shown some microstructures of the materials studied, before and after immersion in 0.5M  $\text{NH}_4\text{OH}$  for 294 days. The changes induced by different mechanisms from corrosion, at the interface of Al 1050/ corrosive environment were studied in comparison to control samples of Al 1050 (before the corrosion).

In Figure 7.a. there is a bright appearance of the original sample surface with a less specific roughness and small imperfections (scratches, nicks).

After the immersion period of 294 days, the surface morphology is deeply modified (Figs. 7.b. and 7.c.). Passivated surface is degraded initially, strong and bright appearance disappeared, being replaced by darker large areas. It appears that the mechanisms of degradation of the material due to corrosion are complex, so it appears that in addition to continuous corrosion (the entire metal surface has suffered from aggressive environmental action) shows a local corrosion (due to structural imperfections, nonmetallic inclusions, internal microtensions by second order) as evidenced by:

- corrosion spots - large portions and relatively small depth;
- corrosion plate - relatively small areas but greater depths;
- points of corrosion (Pitting) - concentrated on small and deep areas (with diameters up to 100  $\mu\text{m}$ ).

316Ti stainless steel samples (Fig.8.) show a very high chemical stability. The area has not changed significantly (probably light intercrystalline corrosion phenomena limit small chemical compounds precipitated in the metallic matrix). Microstructures for P235TR2 show the generalized deep corrosion in spots and points of corrosion (pitting). In Fig. 9.a on the polished sample and without metallographic attack it can be seen a steel with small quantity of nonmetallic inclusions (score 1.5-2). The macro-metallographic analysis reveals that in the presence of heterogeneous structures (pearlite) the corrosion process is intensified because grain dispersed phases are in contact and the alloy behaves like two metals which are in contact in the same corrosive environment (fig. 9.b.). The presence of non-metallic inclusions favors accelerated local corrosion. The typical anodic potentiodynamic polarization curves of material tested, measured in  $\text{NH}_4\text{OH}$  0.5 M solutions, are shown in Fig. 9.

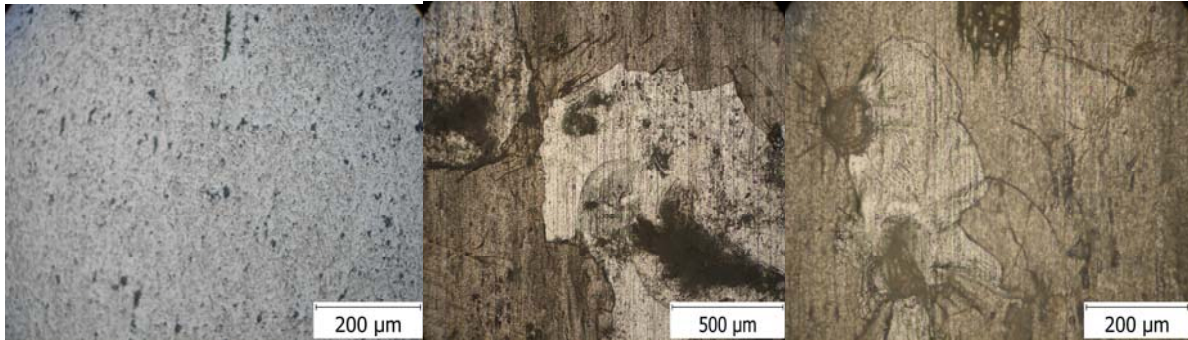


**Fig. 7.** The metallographic aspect of Al 1050 samples before (a) and after immersion for 294 days in  $NH_4OH$  0.5 M

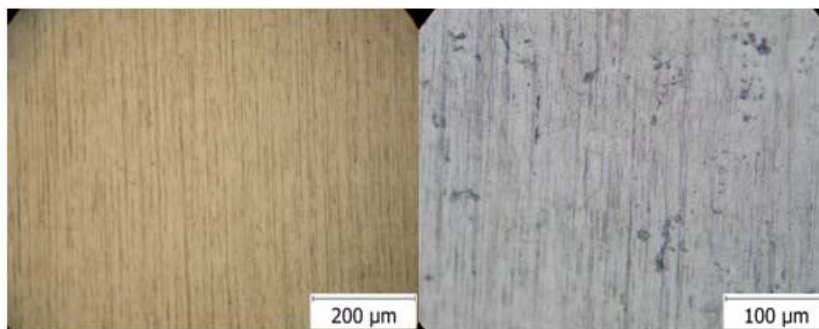


**Fig. 8.** The metallographic aspect of 316Ti samples before and after immersion For 294 days in  $NH_4OH$  0.5 M

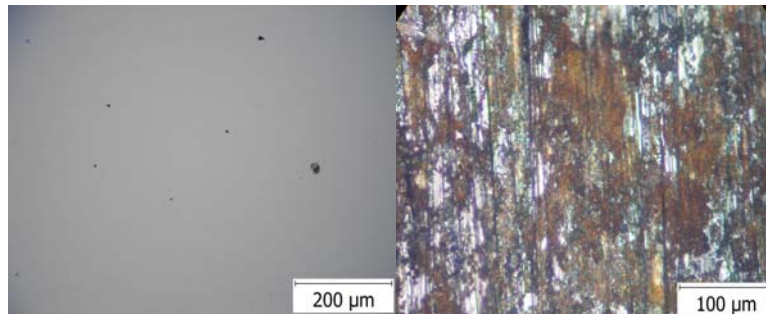


**Fig. 9.** The metallographic aspect of P235TR2 samples before and after immersion For 294 days in  $NH_4OH$  0.5 M

Corrosion rates of the coatings were derived from the Stern–Geary equation:

$$i_{corr} = \frac{1}{2.303R_p} \left( \frac{\beta_a \cdot \beta_c}{\beta_a + \beta_c} \right) \quad (3)$$

- $i_{corr}$  is the corrosion current density in Amps/cm<sup>2</sup>;
- $R_p$  is the corrosion resistance in ohms cm<sup>2</sup>;
- $\beta_a$  is the anodic Tafel slope in Volts/decade or mV/decade of current density;
- $\beta_c$  is the cathodic Tafel slope in Volts/decade or mV/decade of current density;
- the quantity,  $(\beta_a \cdot \beta_c) / (\beta_a + \beta_c)$ , is referred to as the Tafel constant.

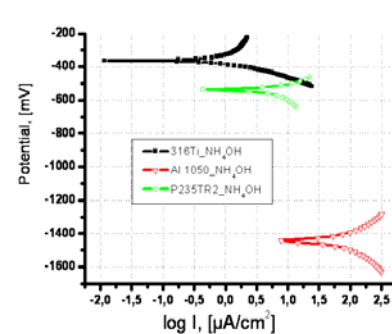


**Fig. 9.** Comparative polarization potentiodynamic curves for tested materials in 0.5M  $NH_4OH$  solution obtained after 60 minutes of immersion time



The polarization resistance,  $R_p$ , was determined from the slopes of the potential-current plots measured by the linear polarization curve (LSV) at a scanning rate of 2 mV/s.

The corrosion potential ( $E_{\text{corr}}$ ), corrosion current density ( $i_{\text{corr}}$ ) and polarisation resistance ( $R_p$ ), which

were obtained from the potentiodynamic polarisation curves are summarized in Table 2.

From potentiodynamic polarization curves the polarization resistance for Al 1050 was  $0.74 \text{ k}\Omega \cdot \text{cm}^2$ . For 316Ti stainless steel samples the polarization resistance was  $29.26 \text{ k}\Omega \cdot \text{cm}^2$ .

**Table 2.** Results from the potentiodynamic polarisation curves for the tested materials

No.	Tested material	Ecor, mV Ag/AgCl	$\beta_a$	$\beta_c$	icor [ $\mu\text{A}/\text{cm}^2$ ]	Rp [ $\text{k}\Omega \cdot \text{cm}^2$ ]	Vcor [ $\mu\text{m}/\text{an}$ ]
			[mV/dec]				
1.	Al 1050	-1443.5	322.3	380.0	102.32	0.74	1115
2.	316Ti	-360.0	478.0	125.0	1.47	29.26	17.21
3.	P235TR2	-585.4	311.1	409.9	8.90	8.62	103.14

## 4. Conclusions

The results obtained from weight loss and electrochemical studies were in reasonable agreement for low alloy steel P235TR2. Microstructures for P235TR2 present profound generalized corrosion, spots and points of corrosion (pitting).

The samples of 316Ti stainless steel show a very high chemical stability.

After the immersion of 294 days, the surface morphology of Al 1050 is profoundly altered. Passivated surface is degraded, strong and bright appearance initially disappeared, being replaced by darker large areas.

From the electrochemical results, it can be seen that the corrosion potential of Al 1050 tends to more negative values, hence it is deduced that the polarization resistance value is the smallest (of the order of  $\Omega$ ) in comparison to other materials whose polarization resistance is of the order  $\text{k}\Omega$ . The corrosion rate calculated has the highest value for Al 1050 ( $1.115 \text{ mm}/\text{year}$ ) and the lowest for 316Ti ( $17.21 \mu\text{m}/\text{year}$ ).

## References

- [1]. M.J. Bartolomé, J.F. del Río, E. Escudero, S. Feliu Jr., V. López, E. Otero, J.A. González - Behaviour of different bare and anodised aluminium alloys in the atmosphere, Surface & Coatings Technology 202 (2008) 2783–2793.
- [2]. Monica Trueba, Stefano P. Trasatti - Study of Al alloy corrosion in neutral NaCl by the pitting scan technique, Materials Chemistry and Physics 121, 2010, 523-533.
- [3]. A. García-Romero, A. Delgado, A. Urresti, K. Martín, J.M. Sala - Corrosion behaviour of several aluminium alloys in contact with a thermal storage phase change material based on Glauber's salt, Corrosion Science 51 (2009) 1263–1272.
- [4]. Serpil Şafak, Berrin Duran, Aysel Yurt, Gülşen Türkoğlu - Schiff bases as corrosion inhibitor for aluminium in HCl solution, Corrosion Science, Volume 54, January 2012, Pages 251–259.
- [5]. Zhenhua Dan, Izumi Muto, Nobuyoshi Hara, Effects of environmental factors on atmospheric corrosion of aluminium and its alloys under constant dew point conditions, Corrosion Science, Volume 57, April 2012, Pages 22–29.
- [6]. S.M. Abd El Haleem, S. Abd El Wanees, E.E. Abd El Aal, A. Farouk - Factors affecting the corrosion behaviour of aluminium in acid solutions. I. Nitrogen and/or sulphur-containing

organic compounds as corrosion inhibitors for Al in HCl solutions, Corrosion Science, Volume 68, March 2013, Pages 1–13.

[7]. E.E. Abd El Aal, S. Abd El Wanees, A. Farouk, S.M. Abd El Haleem - Factors affecting the corrosion behaviour of aluminium in acid solutions. II. Inorganic additives as corrosion inhibitors for Al in HCl solutions, Corrosion Science, Volume 68, March 2013, Pages 14–24.

[8]. X. Zhou, C. Luo, T. Hashimoto, A.E. Hughes, G.E. Thompson - Study of localized corrosion in AA2024 aluminium alloy using electron tomography, Corrosion Science, Volume 58, May 2012, Pages 299–306.

[9]. R. Arrabal, B. Mingo, A. Pardo, M. Mohedano, E. Matykina, I. Rodriguez - Pitting corrosion of rheocast A356 aluminium alloy in 3.5wt.% NaCl solution, Corrosion Science, Volume 73, August 2013, Pages 342–355.

[10]. N. Murer, R.G. Buchheit - Stochastic modeling of pitting corrosion in aluminum alloys, Corrosion Science, Volume 69, April 2013, Pages 139–148.

[11]. WANG Zhen-yao, MATeng, HAN Wei, W Guo-cai - Corrosion behavior on aluminum alloy LY 12 in simulated atmospheric corrosion process, Trans. Nonferrous Met. SOC. China 17 (2007) 326-333.

[12]. A. Pardo, M.C. Merino, A.E. Coy, F. Viejo, R. Arrabal, E. Matykina - Pitting corrosion behaviour of austenitic stainless steels – combining effects of Mn and Mo additions, Corrosion Science 50 (2008) 1796–1806.

[13]. J. M.A. Van der Horst - Corrosion of stainless steel by aqua ammonia, Corrosion Science, 1972, Vol. 12, pp. 761 to 765. Pergamon Press, Printed in Great Britain.

[14]. A. Pardo, M.C. Merino, M. Carboneras, F. Viejo, R. Arrabal, J. Muñoz - Influence of Cu and Sn content in the corrosion of AISI 304 and 316 stainless steels in  $\text{H}_2\text{SO}_4$ , Corrosion Science 48 (2006) 1075–1092.

[15]. A. Pardo, M.C. Merino, A.E. Coy, F. Viejo, M. Carboneras, R. Arrabal - Influence of Ti, C and N concentration on the intergranular corrosion behaviour of AISI 316Ti and 321 stainless steel, Acta Materialia 55 (2007) 2239–2251.

[16]. A. Pardo, M.C. Merino, A.E. Coy, F. Viejo, R. Arrabal, E. Matykina - Effect of Mo and Mn additions on the corrosion behaviour of AISI 304 and 316 stainless steels in  $\text{H}_2\text{SO}_4$ , Corrosion Science 50 (2008) 780–794.

[17]. J.H. Hong, S.H. Lee, J.G. Kim, J.B. Yoon - Corrosion behaviour of copper containing low alloy steels in sulphuric acid, Corrosion Science, Volume 54, January 2012, Pages 174–182.

[18]. Keon Ha Kim, Seung Hwan Lee, Nguyen Dang Nam, Jung Gu Kim - Effect of cobalt on the corrosion resistance of low alloy steel in sulfuric acid solution, Corrosion Science, Volume 53, Issue 11, November 2011, Pages 3576–3587.

[19]. Lining Xu, Shaoqiang Guo, Wei Chang, Taihui Chen, Lihua Hu, Minxu Lu - Corrosion of Cr bearing low alloy pipeline steel in  $\text{CO}_2$  environment at static and flowing conditions, Applied Surface Science, Volume 270, 1 April 2013, Pages 395–404.



[20]. **Mohammed A. Amin, Gaber A.M. Mersal, Q. Mohsen** - *Monitoring corrosion and corrosion control of low alloy ASTM A213 grade T22 boiler steel in HCl solutions*, Arabian Journal of Chemistry, Volume 4, Issue 2, April 2011, Pages 223–229

[21]. **J.B. Sun, G.A. Zhang, W. Liu, M.X. Lu** - *The formation mechanism of corrosion scale and electrochemical characteristic of low alloy steel in carbon dioxide-saturated solution*, Corrosion Science, Volume 57, April 2012, Pages 131–138.

[22]. **Nabel A. Negm, Nadia G. Kandile, Emad A. Badr, Mohammed A. Mohammed** - *Gravimetric and electrochemical evaluation of environmentally friendly nonionic corrosion inhibitors for carbon steel in 1 M HCl*, Corrosion Science, Volume 65, December 2012, Pages 94–103.

[23]. **A. Contreras, S.L. Hernández, R. Orozco-Cruz, R. Galvan-Martínez** - *Mechanical and environmental effects on stress corrosion cracking of low carbon pipeline steel in a soil solution*, Materials & Design, Volume 35, March 2012, Pages 281–289.

[24]. **Octavian Potecașu, Florentina Potecașu, Marian Bordei, Petrică Alexandru, Florin Marin** - *The corrosion behavior of steel for transportation of petroleum products in marine environment*, International Multidisciplinary Scientific GeoConference, SGEM2013, Conference Proceedings, ISBN 978-954-91818-8-3 / ISSN 1314-2704, June 16-22, 2013, Vol. 2, 981 - 988 pp.



## THE MANAGEMENT OF WORK RISK FOR A PLATE ROLLING MILL MACHINE

**Marian BORDEI, Stefan DRAGOMIR, Viorel DRAGAN**

"Dunărea de Jos" University of Galați, 111, Domnească Street, 800201, Galați, Romania  
email: vdragan@ugal.ro

### ABSTRACT

*Arcelor Mittal is the leader on important iron and steel global markets. This company has a performant system for research, for iron and steel plate production and has a top network for distribution, too.*

*The company has production units in 20 countries on 4 continents, in all key markets of iron and steel industry. Arcelor Mittal has committed to operating in its units in a responsible manner and has taken care of the health, safety and welfare of its employees. At the same time, it is committed to acting with respect to sustainable development.*

KEYWORDS: work risk, safety at work places, risk management

### 1. Introduction

Arcelor Mittal Galati is one of the most powerful companies in the south-east of Europe. Analysis of such work will be carried out in laths thick plate nr 2. Thick plate steel rolling mill machine no. 2 (L.T.G. 2) is included in the factory of flat laminates, which are located in the northern part of the mill. The main objective of activity is to obtain finished products like thick plates. Rolling mill machine no. 2 has the purpose to products thick plate with the thickness of 6-120 mm and the width between 1600-4200 mm.

Like every grate unit, the workers take contact daily with risk factors that can affect their integrity and health.

#### ***Risk factors that can exist in the rolling mill process:***

The most important risk factors that appear in rolling mill process are:

1. mechanical chain, coupling, unprotected rolls with specialized cage;
2. bruising caused by diverse transport systems inside the factory;
3. self starting of scissors, crane and rolls of plates transport;
4. sliding or rolling of parts that are stored in not allowed places;
5. tipping over parts, assemblies, materials, stored without ensuring their stability;
6. free drop of parts, equipment, tools that can injure the workers;

7. disposal of iron or steel particles, parts of transmission elements from the rollers without fenders;

8. deviation from normal trajectory of the plates during processing;

9. splash of oil at an accidental crack of hydraulic circuits;

10. separate stings and cuts caused by dangerous surfaces or contours;

11. working in the neighborhood of pressure vessels;

12. low temperature of metallic surface (in cold weather) that workers get contact with;

13. flames that appear because of electrical panel.

### 2. Research targeting factors that may jeopardize job security

After the investigations at the thick steel plate rolling mill machine, Heavy Plate Rolling Mill no. 2 (LTG-2) made by the authors between 15.06 2012 - 15.12.2012, the following causes that can injure workers on mill were revealed:

- electrocution by direct touch, because there have been found uninsured and noninsulated ways of electric power, noninsulated switchboards, improvised electrical connections etc.

- electrocution by indirect touch because there have been found earthing connection systems of the damaged equipment;

- electrocution at voltage appearance because there are electrically operated equipment working in wet environment without protection;
- working with toxic substances - mineral oils, paraffin waxes etc.;
- working with caustic substances - water + phosphates mixture in coolers;
- working with flammable substances - oils, greases etc.;
- high air temperature ( $> 40^{\circ}$  C) in the vicinity of the furnace, on the crossing bridges of the rolling path etc;
- low air temperature during winter - when running repairs (when stationary);
- airflow - leak site, open doors, etc.;
- low lighting level – suspended particles in the air, missing lighting lamps etc.;
- high contrast between the light emitted by incandescent material and general background

- lighting of the enclosure, which can lead to overuse of vision;
- infrared radiation from incandescent material;
- high work rate - due to the functioning mill;
- the execution of contingency operations in work load or differently than it is stipulated in the technical work;
- setting work parameters beyond the prescribed areas of technology work;
- trouble with other performers - working mill is an action team;
- turning on machinery without permission from the checkpoint;
- disruption of the cooling circuit;
- fall on the same level by imbalance, slipping, tripping – walking on slippery surfaces loaded with dust, leaking, etc.
- falls from height: by stepping into the void, by imbalance, by sliding - septic technology without railings, without warning indication.



*Fig. 1. View of L.T.G.-2[1]*

### 3. Measurement and prioritizing risk factors at LTG-2

Research targeting main factors in terms of job security in Heavy Plate Mill No. 2 allowed measurement both in terms of unsafety level and priority.

We named factors starting with F1 to F15 and built the diagram in Figure 2 based on these risk factors, namely:

F1 - lack of protection for some gear wheels, couplings and cinematic chains (gear box, coupling and unprotected cinematic chain;

F2 - click Start-spot inspection of fly scissors, crane or rollers of plates transport;

F3 - design particle - skims, transmission elements from rolls (without device), quick couplers balance and so on;

F4 - normal trajectory deviation of the blank (band) during rolling;

F5 - electrical shock because of unprotected electrical current cable, uninsured electrical panels, improvised electrical connections etc.;

F6 - high air temperature ( $> 40^{\circ}$  C)] in the vicinity of the furnace, on the bridges crossing the rolling path etc.;

F7 - high noise level;

F8 -infrared radiation from incandescent material;

F9 - pneumoniconiosis powders present in workplace air;

F10 - making difficult decisions in a very short period of time, when dealing with situations of "incident" or "fault" type;

F11 - fall on the same level by imbalance, slipping, tripping - slippery caused by walking on surfaces loaded with dust, leaks etc.;

F12 - contact with dangerous surfaces or contours (pungent, sharp, slippery, abrasive, adhesive);

F13 - free fall of parts, materials, tools at higher rates;

F14 - walking, stops in dangerous areas on access roads, car or rail, stand rolling mill, roller path on walkways etc.;

F15 - failure of using labor protection equipment and installations and other means of protection granted by the employer.

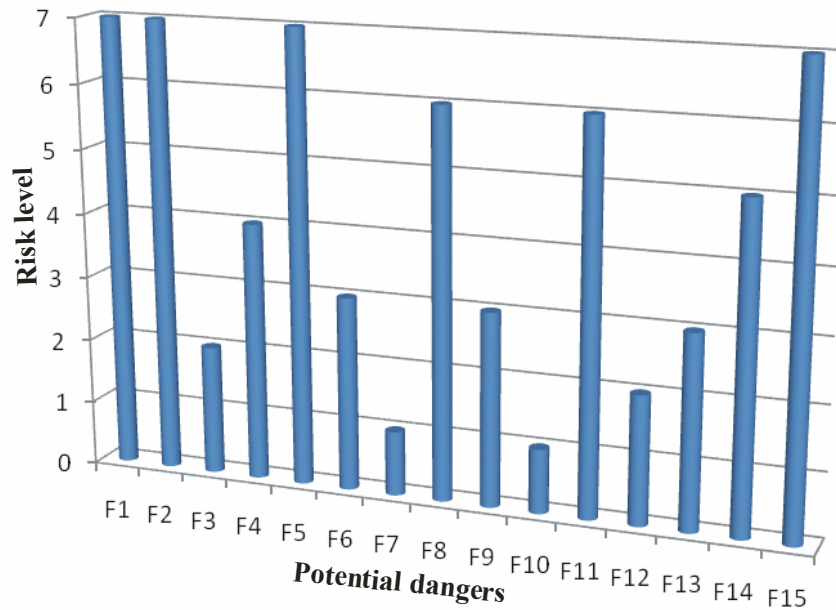


Fig. 2. Variation of potential dangers in connection with risk level [3].

It is noticed that the maximum potential danger is at positions F1 (gear box, coupling and unprotected cinematic chain), F2 (click Start-spot inspection of fly scissors, crane or rollers of plates transport), F5 (Electrical Shock, because of unprotected electrical current cable, unensured electrical panels, improvised electrical connections and F15. The minimum for potential danger is at position F7 (high noise level) and F10 (Making difficult decisions in a very short period of time, when dealing with situations of "incident" or "fault" type).

### 3.1. Calculus and measurement of risk level

$$N_r = \frac{\sum_{i=1}^n r_i \cdot R_i}{\sum_{i=1}^n r_i} \quad (1)$$

which:

$N_r$  - level of global risk at work place;

$r_i$  - risk factor "i";

$R_i$  - the risk level for a risk factor "i";

$n$  - number of risk factors that were identified at each work level.

$$N_r = (7+7+2+4+7+3+1+6+3+1+6+2+3+5+7)/15 = 64/15 = 4.26$$

This value of 4.26 resulted from the calculation made by formula (1) shows that "laminator" work falls into the category of jobs with partial risk level.

In Figure 3 we show the share of risk factors identified by the partial values of the levels of risk.

It is noticed that the risk factors with the greatest share while working is over 74%. Another risk class (secondary) has the value over 12% and the third is about 5.5%.

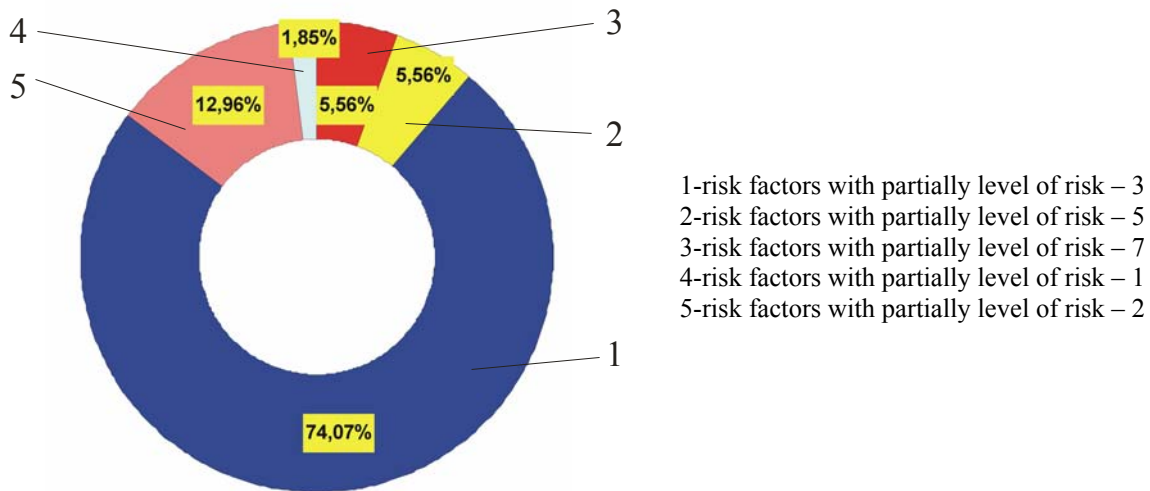


**Fig. 3.** The share of risk factors identified by the partial values levels of the risk.[3]

#### 4. Conclusions

According to the research performed on job security in the thick steel plate Rolling Mill machine no. 2 (LTG 2) we conclude that the main measures to be taken to secure these jobs are:

- using personal protective equipment and means of collective labor protection equipment;
- attending daily and quarterly briefings on security or safety line in section mills;
- conducting periodic medical examination in due time;
- not initiating work if restricted marks and registers do not exist at the control station and immediately announcing the supervisor;
- using of stopping restriction trademarks, repairing and restarting the mill machinery;
- maintaining protective railings, guards and protective cases from moving car bodies and protective railings on stairwells and walkways;
- using special cables and chains, metrologically checked and endowed with panels with the maximum charge allowed for the evacuation of bucket drops;
- failure of interventions to under pressure plants, lifting and transport if there are no appropriate qualifications;
- failure of loads bidding activities at and from lifting hook, unless the worker is trained and authorized as slinger or the worker;
- non-use of unapproved binding elements and devices, improvised and/or unregistered in registers at work;
- non-use of tools, devices and controllers not approved, worn out and/or improvised;
- the issue of access ladders, working platforms and traffic routes with materials, parts, waste, and so on;

- carrying out operational activities of technical machinery in mills based on working instructions and safety;
- non-interference in the mill machinery if it is not stopped and secured against accidental starting;
- performing installation work – remove of stand rolling mill, of support and working cylinders only when the rolling mill does not function.
- taking measures to exclude fall of slag drop or other objects while performing cleaning activities of scale channels;
- unsteady at a distance of less than 5 meters from the machines of the mill, under running (way roller degrosor train, train wheel, rulors, transercars, chain conveyor, tandem, furnaces, etc.) excepting operators in the area;
- non-intervention with bare hands on semifinished or reddening table elements (hot elements);
- non-intervention in rolls strapping machine while tied wrap roll band;
- immediate shutdown of equipment where there is imminent risk of injury;
- use of access routes and movement marked, well lit and suitably delimited slippery, while walking from one work station to another;
- do not going over moving conveyor chains;
- non-interference in electrical systems for remedying faults;
- waste and drop deposit (waste of scissors cutting laminates) in spaces designated for that purpose;
- conducting activities so as to prevent injury or occupational illness to yourself or other employees of the business;
- performing only activities that are authorized according to legal requirements.



If these measures are respected by the workers of Heavy Plate Mill No. 2, the risk of the job will greatly decrease and thus the personal safety for these jobs will increase.

### References

[1]. \*\*\* - Instrucțiunea de lucru la laminatul de Tabla Groasa nr.2 "I.L – 007/2012, rev. 0";

[2]. \*\*\* - Instrucțiunea de lucru la paturile de racire "I.L. –L - 107/2007, rev.0";

[3]. \*\*\* - Instrucțiunea tehnică de lucru privind exploatarea și întreținerea sistemelor de protecție și siguranță la laminor „I.L.-L – 015/2007, rev. 1”;

[4]. \*\*\* - Instrucțiunea tehnică de lucru privind efectuarea activității de curățenie a slmurilor si tunderului „I.L. – L – 086/2007, rev. 2”.

[5]. \*\*\* - Cartea lucratorului laminatorist- Ed. Interna. Rev. 2012.



## THERMOMECHANICAL PROCESS SIMULATION TO PREDICT PROCESSING OF MECHANICAL PROPERTIES OF ALLOYS Al-Zn-Mg-Cu

Marian-Iulian NEACSU, Elisabeta VASILESCU,  
Doru HANGANU  
email: uscaeni@yahoo.com

### ABSTRACT

*This paper presents how to perform simulation (prediction) mechanical properties of aluminum alloys of the system Al-Zn-Mg-Cu. Graphical interface that can predict the mechanical properties studied was performed using MATLAB software version 6.5 based on mathematical equations mathematical models obtained by the mathematical modeling of thermomechanical treatment process studied. This GUI can be established before the thermomechanical treatment parameters to achieve a favorable complex mechanical properties.*

KEYWORDS: GUI, aluminum alloy thermomechanical treatment, mathematical modeling

### 1. Introduction

Due to special properties such as high strength, low specific gravity, chemical stability, good thermal conductivity, good to very good resistance to corrosion, etc. aluminum alloys find their application in almost all branches of modern industry and aviation implicitly. Close cooperation between aircraft manufacturers and metallurgical engineers led to obtaining material characteristics. Since the inception of building aircraft manufacturers have been clear that the materials were to be used for aircraft must be at the same time, strong and lightweight. In aeronautical engineering has had a rapid development that makes metallurgy strive to ensure performance materials to meet the requirements of the aviation industry. Alloy Al-Zn-Mg-Cu are part of deformable aluminum alloys and

hardened by applying heat treatment and (or) Thermo.

Some of them have mechanical properties comparable to alloy with copper base with some steel grades, but have the advantage of much lower density. In this paper we present research conducted by the authors on thermomechanical processing of these alloys that leads to optimal complex materials properties such.

### 2. Experimental conditions

Tensile strength alloys Al-Zn-Mg-Cu is even greater as the precipitate formed, which is phase hardening precipitates, after aging, natural or artificial, are more numerous, finer and more dispersed in the solution table core (solid solution). Experiments were performed on samples from alloy chemical composition given in Table 1.

*Table 1. Chemical composition of alloys subjected to research*

Element	Zn	Mg	Cu	Si	Fe	Pb	Cr	Mn	Al
Alloy									
1(AlZn2,6Mg2)	2.67	2.06	1.22	0.31	0.29	0.0025	0.06	0.47	rest
2(AlZn4,5Mg1)	4.5	1.4	0.2	0.35	0.4	-	0.35	0.5	rest
3(AlZn5,7MgCu)	5.76	2.61	1.55	0.15	0.19	0.021	0.19	0.10	rest

Alloys have been investigated alloys are the principal alloying element is zinc. As shown in Al-Zn equilibrium diagram in Figure 1., Zn content of the

three alloys investigated were of 2.67, 4.5 and 5.76% Zn alloys are part of wrought alloys and hardened by treatment heat.

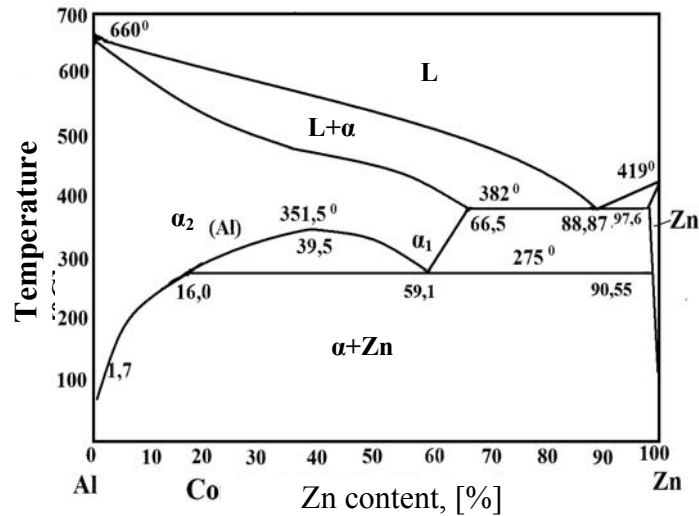


Fig.1. Al-Zn equilibrium diagram [16]

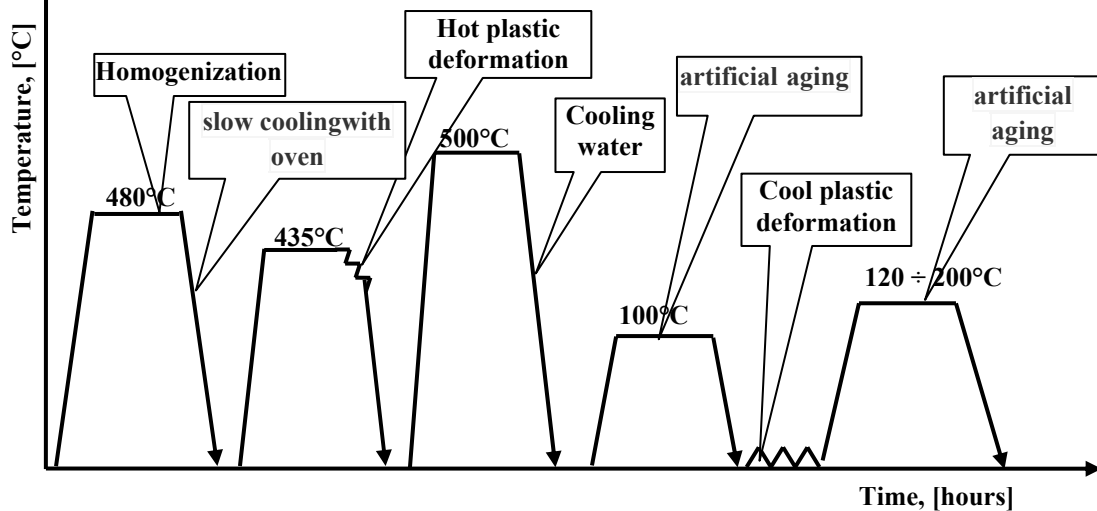


Fig. 2. Schematic representation of thermal and thermomechanical processing

Sequence of operations that have undergone three samples of three is shown in Figure 2.

As illustrated in Figure 2 samples of the three alloys considered were subjected to thermomechanical treatment with cold plastic deformation between two artificial aging. After implementing the solution hardening is performed at a temperature of 100°C aging for 1 hour to stabilize structural material. Further, the samples are subjected to cold plastic deformation, with three degrees of deformation,  $\epsilon_1 = 10\%$ ,  $\epsilon_2 = \epsilon_3 = 20\%$  and  $30\%$ , to achieve set size.

Subsequently these distortions is achieved by artificial aging heat treatment at temperatures  $T_1 = 120^\circ\text{C}$ ,  $T_2 = 140^\circ\text{C}$ ,  $T_3 = 160^\circ\text{C}$ ,  $T_4 = T_5 = 180^\circ\text{C}$  and  $200^\circ\text{C}$  and time-keeping:  $\tau_1 = 4\text{hours}$ ,  $\tau_2 = 8\text{hours}$ ,  $\tau_3 = 12\text{hours}$ ,  $\tau_4 = 16\text{hours}$ ,  $\tau_5 = 20\text{hours}$ .

Among the aluminum alloys studied alloy (3) AlZn5.7Mg2.6 gathered the best physical and mechanical properties of resistance. Based on this consideration, in order to optimize the use of this alloy properties, we proceeded to develop mathematical model typical thermomechanical treatment process, based on the optimization process.

We considered that the main influencing factors (independent variables) thermomechanical treatment following technological parameters:

- 1 - artificial aging temperature -  $t$  [ $^\circ\text{C}$ ];
- 2 - while maintaining the temperature of artificial aging -  $\tau$  [h];
- 3 - degree of plastic deformation -  $\epsilon$  [%].

Optimized parameters are considered as the set of physical and mechanical properties:  $R_m$ ,  $R_{p0.2}$ ,  $A_5$ , HB.

Given studies and experimental results obtained by some authors [141], [155], [156] on alloys with high strength aluminum base, we established experimental conditions as follows:

- aging temperature:
  - basic level:  $U_{01} = 160^{\circ}\text{C}$ ;
  - the range:  $\Delta u_1 = 40$ ;
- the duration of aging:
  - basic level:  $U_{02} = 12$  hours;
  - the range:  $\Delta u_2 = 8:00$
- the degree of deformation:
  - basic level:  $U_{03} = 20\%$ ;
  - the range:  $\Delta u_3 = 10\%$

We used samples of the same thickness, and the total degree of strain variation was cold by maintaining a constant final thickness.

Coded to represent the experiment, we used the following notations and symbols:

Independent variables:

- $x_1$  - artificial aging temperature,  $t$ ,  $^{\circ}\text{C}$ ;

$$Y_1(t, \tau, \varepsilon) = 592,1339 - 1,0766 \cdot t + 7,6406 \cdot \tau + 3,6063 \cdot \varepsilon - 0,0293 \cdot t \cdot \tau - 0,0059 \cdot t \cdot \varepsilon - 0,0016 \cdot \tau \cdot \varepsilon$$

$$Y_2(t, \tau, \varepsilon) = 536,621 - 0,8375 \cdot t + 7,0625 \cdot \tau + 4,5375 \cdot \varepsilon - 0,0328 \cdot t \cdot \tau - 0,0213 \cdot t \cdot \varepsilon + 0,0594 \cdot \tau \cdot \varepsilon$$

$$Y_3(t, \tau, \varepsilon) = 8,125 + 0,0219 \cdot t - 0,1063 \cdot \tau - 0,0438 \cdot \varepsilon + 0,0003 \cdot t \cdot \tau - 0,0004 \cdot t \cdot \varepsilon + 0,0003 \cdot \tau \cdot \varepsilon$$

$$Y_4(t, \tau, \varepsilon) = 137,5357 - 0,1906 \cdot t + 4,5625 \cdot \tau + 1,6 \cdot \varepsilon - 0,0195 \cdot t \cdot \tau - 0,005 \cdot t \cdot \varepsilon + 0,0063 \cdot \tau \cdot \varepsilon$$

After verifying the adequacy of mathematical models based on Fisher criterion shows that all models are consistent with experimental data and can be used to optimize the thermomechanical processing.

With MATLAB software version 6.5 and based on the mathematical model obtained was made a prediction program (simulation) values of mechanical properties investigated.

- $x_2$  - retention time,  $\tau$  [h];
- $x_3$  - degree strain,  $\varepsilon$  [%];

Dependent variables (parameters optimized)

- Y1 - tensile strength,  $R_m$  [MPa];
- Y2 - yield,  $R_{p02}$  [MPa];
- Y3 - Specific elongation at break,  $A_5$  [%];
- Y4 - hardness, HB;

Between natural and coded values of the factors are the following relations  $x_i$  link:

$$x_1 = \frac{t - t_0}{\Delta t}; \quad x_2 = \frac{\tau - \tau_0}{\Delta \tau}; \quad x_3 = \frac{\varepsilon - \varepsilon_0}{\Delta \varepsilon};$$

$Y_i$  values are expressed in natural units. As we study the influence of three factors on process performance (Y) has conducted a full factorial experiment type 23. Complete factorial experiment based matrix coefficients are calculated regression equation (mathematical model).

The specific calculations to obtain the final form of mathematical models, corresponding to the four properties studied:

### 3. Results and discussion

The simulation values of mechanical properties studied is shown with graphical interfaces and usable parameter values within experimental thermomechanical treatment.

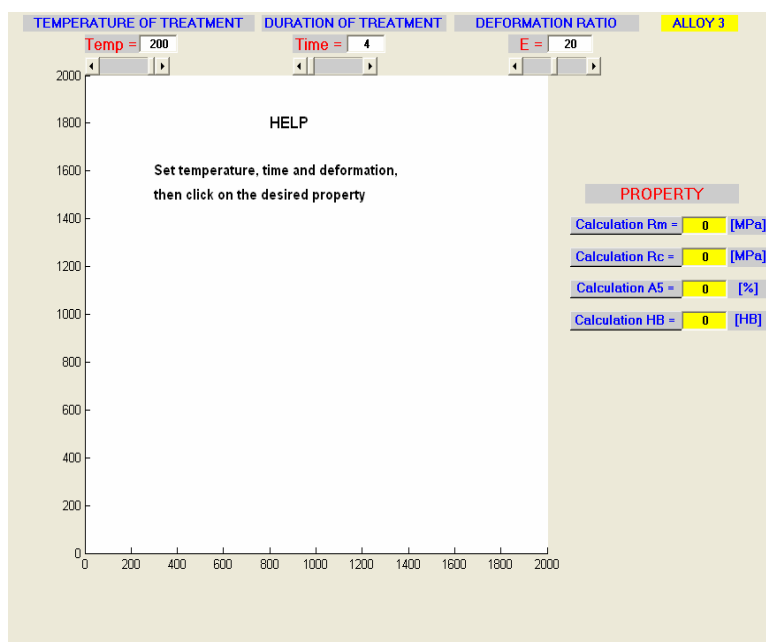


*Fig. 3. The picture began to run simulation program based on the property values of parameters thermomechanical treatment*

The input parameters (thermomechanical treatment parameters) Remove the period studied, based on which the range of values were obtained mathematical equations, the simulation accuracy is lower. Figure 3 presents the picture began to run simulation program based on the values of properties in thermomechanical treatment parameters.

Figure 4 shows the simulation of the mechanical strength of the alloy value (3) that was subjected to thermomechanical treatment which consisted of cold plastic deformation with a degree of deformation of 25% followed by artificial aging at 170°C with a time of maintenance 5 hours.

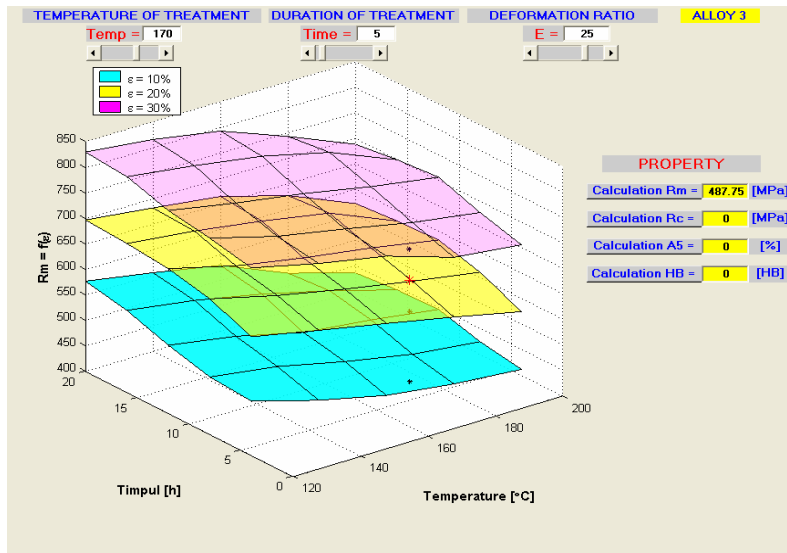


**Fig. 4.** Prediction value of  $R_m$  for alloy 3 to artificial aging temperature of 170°C for 5 hours and cold deformation degree  $\varepsilon=25\%$

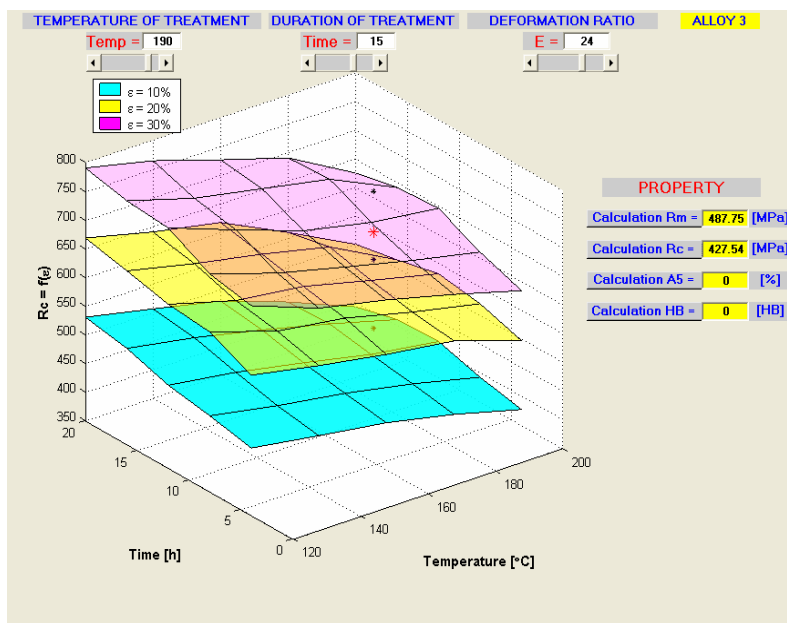


**Fig. 5.** Prediction for Alloy 3 of the value of  $R_{p0.2}$  artificial aging temperature of 190°C for 15 hours and the degree of plastic deformation  $\varepsilon = 24\%$

## Conclusions

Proceed similarly to find any of the 4 studied mechanical properties ( $R_m$ ,  $R_{p0.2}$ , HB, A5) to any value within the thermomechanical processing parameters studied, temperature: 120°C to 200°C for retention time  $\tau = 4 \div 20$  hours and the degree of deformation  $\varepsilon = 10 \div 30\%$ .

Mathematical modeling of thermomechanical treatment processes performed, led to mathematical models that express the connection / correlation between the overall mechanical properties of strength and plasticity and main influence factors, ie the main parameters of thermomechanical treatment.



Equations of the mathematical model allowed and highlighting technological parameters with the greatest influence on the mechanical properties, but also the order in which parameters influence these properties. A GUI was made based on mathematical models and equations using MATLAB program. This interface can predict mechanical properties so you can know in advance what values should have thermomechanical treatment parameters to achieve a complex anuomoit property of a certain value to them.

### References

- [1]. **Alexandru I.** – *Știința materialelor metalice*, Editura Didactică și Pedagogică, București, (1996)
- [2]. **Aloman A.** – *Fazele și compoziția chimică a materialelor*, Editura Bren București, (2001)
- [3]. **Aloman A.** – *Structura materialelor*, Editura AGIR București, (2000)
- [4]. **Banabic D., Dorr I. R.** – *Modelarea proceselor de deformare plastică a tablelor metalice*, Editura Transilvania Press, Cluj-Napoca, (1995)
- [5]. **Askeland D. R.** – *The Science & Engineering of Metals*, 3-rd edition, (1994)
- [6]. \*\*\* – *ASTM Handbok vol. I–X*, (1999)
- [7]. **Bunea D., Șaban R., Vasile T., Gheorghe D., Brânzei M.** – *Alegerea și tratamentele termice ale materialelor metalice*, Editura Didactică și Pedagogică. București, (1996)
- [8]. **Bunea D., ș. a.** – *Studiul materialelor*, Editura Universității Politehnica București, (1993)
- [9]. **Cazimirovici E.** – *Bazele teoretice ale deformării plastice*, Editura Bren București, (1999)
- [10]. **Cănănau N., Tănase D.** – *Tehnologia deformării plastice*, Galați University Press, (2010)
- [11]. **Ciucă I. Dumitriu S.** – *Modelarea și optimizarea proceselor metalurgice de deformare plastică și tratamente termice*, Editura Didactică și Pedagogică, București, (1998)
- [12]. **Taloi D.** – *Optimizarea proceselor tehnologice – aplicații în metalurgie*, Editura Academiei, București, (1987)
- [13]. **Neașu M., Hanganu D., Vasilescu E.** - *Mathematical modeling of thermomechanical treatment process applied to aluminum base alloys for aeronautics*, Analele Universitatii „Dunarea de Jos” din Galati, Fascicula IX Metalurgie și Știința Materialelor, nr.4/2011, pag. 70 – 76
- [14]. **Neașu M.** – *Influența compoziției chimice a tratamentelor termice și termomecanice asupra proprietăților mecanice ale aliajelor Al-Zn utilizate în aeronautică*-Teza de doctorat, Galați (2012)
- [15]. **Popescu D; Ionescu F, Dobrescu R. Ștefanioiu D.** - *Modelare în ingineria proceselor industriale*, Editura AGIR, Bucuresti (2011)
- [11]. **Ienciu, M. ș.a.** - *Elaborarea și turnarea aliajelor neferoase speciale*. Editura Didactică și Pedagogică, București (1985).



## EFFECT OF MEAN DIAMETER SIZE OF DISPERSE PHASE ON MORPHOLOGY AND CORROSION RESISTANCE OF PHENOL – FORMALDEHYDE RESIN/Zn COATINGS

\*Alina CIUBOTARIU<sup>1</sup>, Lidia BENE<sup>1</sup>, Pierre PONTIAUX<sup>2</sup>

<sup>1</sup>"Dunarea de Jos" University of Galati,

Faculty of Environmental and Materials Engineering, Competences Center Interfaces – Tribocorrosion and Electrochemical Systems, 47, Domneasca Street, 80008, GALATI, Romania

<sup>2</sup>Ecole Centrale Paris, Laboratoire Genie de Procédés Matériaux Grand Voie des Vignes, 92290, Chatenay Malabry, France

\*Corresponding author

email: Alina.Ciubotariu@ugal.ro

### ABSTRACT

*The present work has the purpose of obtaining composite coatings using phenol – formaldehyde (PF) resin electrodeposited with zinc. The phenol – formaldehyde resin/Zn coatings were electrodeposited from a suspension of PF resin particles with two dimensions for mean diameter size of particles (0.1 – 5.0  $\mu\text{m}$  and 6 – 10  $\mu\text{m}$ ) in aqueous zinc sulphate electrolyte. Suspension was prepared by adding 10 g/L PF resin particles into solution. The thickness and morphology of the coatings were investigated by SEM method. By adding PF resin in zinc electrolyte for electrodepositing we obtained a very good distribution of PF resin particles on zinc surface. The electrochemical behavior of the layers in the corrosive solution was investigated by electrochemical methods. As electrochemical test solution 0.5M sodium chloride was used in a three electrode open cell. It was observed that by adding PF resin particles in zinc electrolyte for electrodeposition were obtained composite layers more resistant to corrosive attack of 0.5M NaCl than pure zinc obtained from electrodeposition at the same parameters for electrodeposition. Corrosion rate for pure zinc coatings was 72.05  $\mu\text{m}/\text{year}$  versus 15.34  $\mu\text{m}/\text{year}$  for coatings with mean diameter size of particles 0.1 – 5.0  $\mu\text{m}$ , respectively 10.11  $\mu\text{m}/\text{year}$  for coatings with mean diameter size of particles 6 – 10  $\mu\text{m}$ . Values of polarization resistance obtained with both electrochemical methods (potentiodynamic polarization and electrochemical impedance spectroscopy) were in a very good agreement.*

KEYWORDS: phenol - formaldehyde resin particles, electrodeposition, coatings, coatings morphology, polarisation resistance

### 1. Introduction

The deterioration of metal and steel structures due to the atmospheric corrosion is one of the most serious problems in modern world, which leads to a loss of hundreds of billions of dollars each year [1]. Hence, it has become the main objective of material researchers to protect metal and steel against corrosion. In the latest years, composite coatings are regarded as one of the most effective materials to protect metal and steel against atmospheric corrosion.

Composite materials are material systems that consist of a discrete constituent (the reinforcement)

distributed in a continuous phase (the matrix) and that derive their distinguishing characteristics from the properties and behaviour of their constituents, from the geometry and arrangement of the constituents, and from the properties of the boundaries (interfaces) between the constituents.

Composites are classified either on the basis of the nature of the continuous (matrix) phase (polymer – matrix, metal – matrix, ceramic – matrix and intermetallic – matrix composites) or on the basis of the nature of the reinforcing phase (particle reinforced, fibre reinforced, dispersion strengthened, laminated etc.). The properties of the composite can

be tailored and new combinations of properties can be achieved [2].

Relevant work refers to some particles such as B<sub>4</sub>C, CeO<sub>2</sub>, graphite, TiO<sub>2</sub>, ZrO<sub>2</sub>, Al<sub>2</sub>O<sub>3</sub>, V<sub>2</sub>O<sub>5</sub>, SiO<sub>2</sub> – zinc reinforced system [3 – 10] while investigations regarding polymeric particles as disperse phase are relatively limited. To improve adherence and anti-corrosion behaviour of zinc, the existing few reports refer to composite zinc-coated steel, containing polymethylmethacrylate (PMMA), polystyrene (PS) or stabilized polymeric micelle (SPM; core-shell structures consisting of block co-polymers of polyethers) particles [11 – 13]. Recently it was reported that ultrahigh molecular weight polyethylene (UHMWPE) could be deposited in cobalt matrix [14].

Electrochemical deposition is a good method to obtain coatings with the advantage of low synthesis temperature, low costs and high purity in the product. This method also enables rigid control of film thickness, uniformity and deposition rate. Zinc electrodeposition is an industrial process and is widely used to coat on steel for enhancing its service life. The reason for the pre-eminence of zinc in the world of electrodeposition can be attributed to its relative readiness to deposition and better corrosion resistance [15 – 18].

The present work focuses on electrodeposition of PF resin particles (Novolac) with zinc from zinc sulphate plating bath. The thickness and surface morphology of the coatings were analyzed by SEM method. The corrosion resistance of composites coatings was estimated and compared to conventional zinc coating which used potentiodynamic polarization and impedance techniques.

## 2. Experimental part

Pure zinc and PF resin/Zn coatings were obtained on DC04 steel support from the bath solutions with the following composition: 310 g/L ZnSO<sub>4</sub> · 7H<sub>2</sub>O; 75 g/L Na<sub>2</sub>SO<sub>4</sub> · 10H<sub>2</sub>O; 30 g/L Al<sub>2</sub>(SO<sub>4</sub>)<sub>3</sub> · 18H<sub>2</sub>O. Zinc sulphate electrolyte has cathodic polarization bigger than zinc chloride electrolyte so that we used sulphate electrolyte for electrodeposition. Sodium sulphate increased the conductivity and ability for disperse and aluminium sulphate was used like buffering agent which stabilized the acidity of electrolyte. Concomitantly we obtain more shining layers.

The pH of the solution was 3.8. Deposition was carried out at current density of 3.0 A/dm<sup>2</sup>, deposition time of 60 minutes and stirring rate of 800 rpm. Electrodeposition experiments were performed at room temperature.

The zinc metal plate with high purity and steel plates were employed as anode, respectively cathode. Before electrodeposition, steel plates were

mechanically polished, degreased with alkaline solution and washed with distilled water.

The PF resin/Zn coatings were electrodeposited from a suspension of PF resin particles type Novolac with commercial name Resital 6358/1 synthesized by Hüttenes - Albertus Germany in aqueous zinc sulphate electrolyte by adding 10 g/L PF resin particles with mean diameter size of 0.1 – 5.0 µm and 6.0 – 10.0 µm into bath solution.

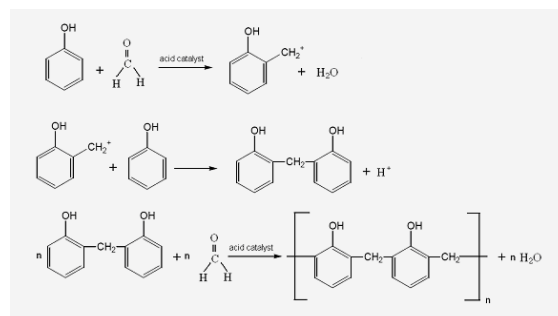


**Fig. 1.** Schematic illustrating the formation of the PF resin type structures

Phenol – formaldehyde resin is a thermo reactive polymer which become plastic with increased the temperature and lose his plasticity and become insoluble. PF resins type Novolac can be obtained from phenol and formaldehyde in acid medium (Figure 1).

Properties of phenol - formaldehyde resin used as disperse phase for electrodeposition are presented in Table 1.

**Table 1.** Properties of PF resin Resital 6358/1

Properties	Values
Molecular weight	3392 – 3816 g/mol
Melting point	70 – 80 °C
Viscosity at 120 °C	35 – 45Pa.s
Free phenol	< 1%
Water content	< 0.5 %
Not esterified	

The thickness and the morphology of deposits were examined by scanning electron microscopy (SEM) used a microscope type JEOL, JSM-T220 A.

For potentiodynamic polarization measurements it was used a three-electrode open cell with platinum electrode as counter, a mercury – mercurous sulphate electrode Hg/Hg<sub>2</sub>SO<sub>4</sub>/saturated K<sub>2</sub>SO<sub>4</sub> as reference electrode (E = + 658 mV/NHE) and coatings as working electrode. Initial potential (I.P.) was -1.9V (Hg/Hg<sub>2</sub>SO<sub>4</sub>), final potential (F.P.) was - 1.2V (Hg/Hg<sub>2</sub>SO<sub>4</sub>) and a scan rate of 1.66mV/s.

Electrochemical Impedance Spectroscopy (EIS) measurements were performed in the frequency range between 65 kHz – 0.1 Hz, with an AC sine wave amplitude of 10 mV, frequency per decade: 10 Hz and delay before integration 1s. The electrochemical corrosion tests were recorded after 30 min of immersion in corrosive medium 0.5M NaCl.

### 3. Results and discussions

#### 3.1. SEM analysis

The thicknesses of pure zinc and PF resin/Zn coatings determined with scanning electron microscope are presented in Figure 2.

It could be observed that higher thickness is for pure zinc coatings and, by increasing the mean diameter size of resin particles the layers thickness increased. This can be explained, probably, because by adding disperse phase the morphology and uniformity of composite coating increase. A higher thickness for coatings with bigger mean diameter size of particles is possible because these particles do not uniform and compact coatings as much as resin with smaller mean diameter size.

Figures 3 - 5 compare morphological aspects of pure zinc coatings and PF resin/Zn coatings obtained with different mean diameter size of disperse phase under SEM method.

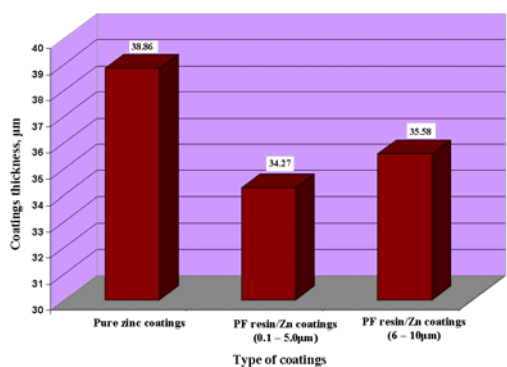


**Fig. 2.** Comparative thickness of coatings

As it can be seen from the micrographs there is an obvious and well distinguishable grain refinement in the presence of the polymer particles. So that the addition of PF resin particles in electrolyte bath significantly changes the morphology of the zinc deposits as compared to those obtained from solutions without disperse phase. The zinc coatings are made up of regular crystals. The polymer particles codeposit disorder the regular crystal structure of zinc coatings and zinc crystals becomes finely crystalline.

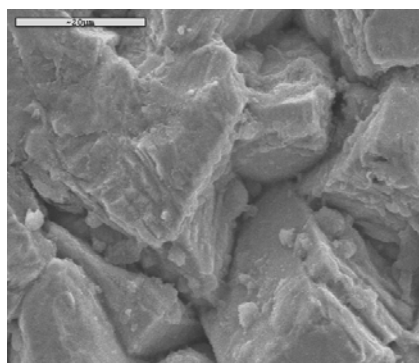


**Fig. 3.** SEM surface morphology of pure zinc coatings (x 2000)

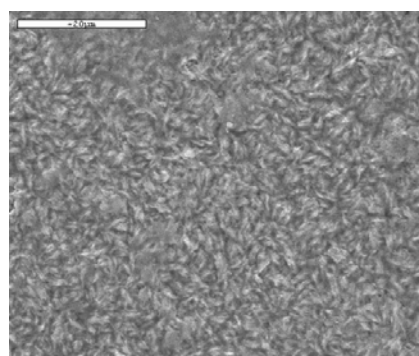


**Fig. 4.** SEM surface morphology of PF resin/Zn coatings with mean diameter size of PF resin 0.1 – 5.0  $\mu\text{m}$ , (x 2000)

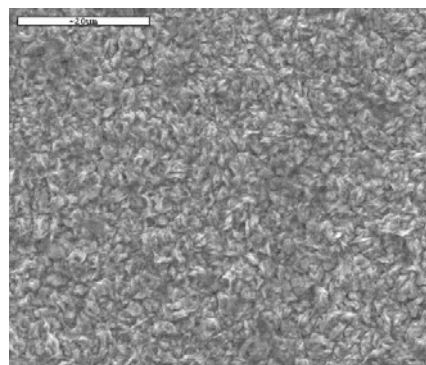


**Fig. 5.** SEM surface morphology of PF resin/Zn coatings with mean diameter size of PF resin 6 – 10  $\mu\text{m}$  (x 2000)

The pure zinc coatings have a rather regular surface, whereas the composite coating surfaces have finer grains structure with particles of disperse phase uniformly distributed on the surfaces.

The polymer particles could be an inhibition effect of growing crystallite size of zinc.

### 3.1. Electrochemical measurements

The electrochemical investigation of each sample began with monitoring of the open circuit potential change immediately after the immersion into the testing solution till reaching a relatively stable stationary value (Figure 6).

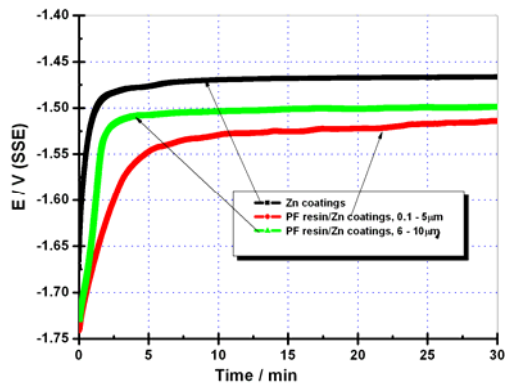


**Fig. 6.** Variation of the coatings potential function of time in 0.5M NaCl

From the dependence of potential function time it can be concluded that the tested samples are stable after 10 - 15 minutes from immersion in test solution.

The polarisation curves for coatings in 0.5M NaCl after 30 minutes from immersion are presented in Figure 7.

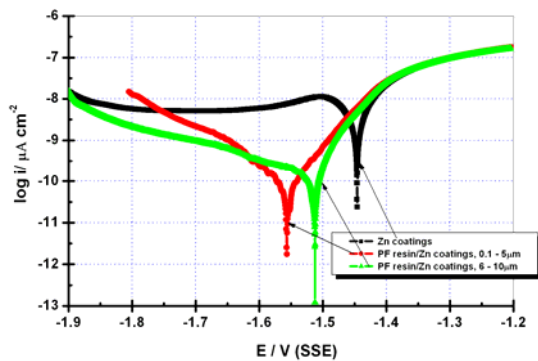


**Fig. 7.** Potentiodynamic polarisation data for coatings immersed in 0.5 M NaCl solution obtained after 30 minutes from immersion time (log scale)

Quantitative information on corrosion currents density and polarisation resistance can be extracted from the slope of the curves, using the Stern-Geary equation [19].

$$i_{corr} = \frac{1}{2.303R_p} \left( \frac{\beta_a \cdot \beta_c}{\beta_a + \beta_c} \right) \quad (1)$$

Tafel parameters derived from Figure 7 using Tafel extrapolations are presented in Table 2.

Corrosion rates (CR) were calculated by equation (2):

$$CR(\mu\text{m}/\text{year}) = \frac{0.051 \cdot i_{corr} \cdot (E_q \cdot \text{wt.})}{d} \quad (2)$$

where:  $i_{corr}$  – corrosion current density calculated from Stern – Geary equation;  $(E_q \cdot \text{wt.})$  is the equivalent weight and  $d$  is the density of the zinc metal in  $\text{g}/\text{cm}^3$ .

The corrosion potential is shifted to more negative values for PF resin/Zn coatings than corrosion potential for pure zinc coatings.

From experimental data it was observed that polarisation resistance has a small value for pure zinc coatings ( $34.54 \Omega \cdot \text{cm}^2$ ), a bigger value for PF resin/Zn composite coatings with mean diameter size of particles  $0.1 - 5 \mu\text{m}$  ( $238.75 \Omega \cdot \text{cm}^2$ ) and the biggest value for PF resin/Zn composite coatings with mean diameter size of particles  $6 - 10 \mu\text{m}$  ( $336.32 \Omega \cdot \text{cm}^2$ ). The values of corrosion rate calculated with formula (2) were: for pure zinc coatings  $72.05 \mu\text{m}/\text{year}$  and for composite coatings  $15.34 \mu\text{m}/\text{year}$ , respectively  $10.11 \mu\text{m}/\text{year}$ .

Those parameters presented before indicated a good corrosion resistance of PF resin/Zn coatings in 0.5 M NaCl.

Figure 8 shows the Nyquist plots of zinc and PF resin/Zn composite coatings measured in 0.5M NaCl solution after 30 min from immersion in corrosive environment.

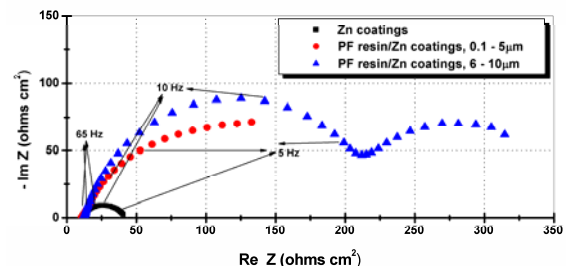


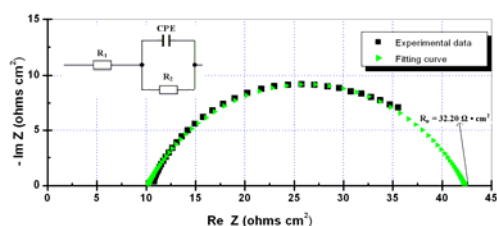
**Fig. 8.** Nyquist plots for pure zinc and PF resin/Zn coatings in 0.5M NaCl after 30 min from immersion

The fitting data of Nyquist plots for coatings are presented in Figure 9 (a - c).

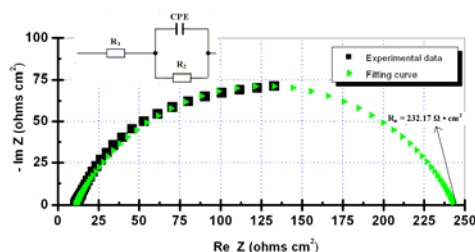
**Table 2.** Tafel parameters of pure zinc and composite coatings calculated from polarization potentiodynamic curves obtained after 30 min from immersion in solutions

Type of coatings	$E_{\text{corr}}$ , V; vs SSE	$i_{\text{corr}}$ , $\mu\text{ A/cm}^2$	$\beta_a$ , mV/dec	$\beta_c$ , mV/dec	$R_p$ , $\Omega\cdot\text{cm}^2$	CR, $\mu\text{m/year}$
Zinc	- 1.45	152.75	28.76	21.04	34.54	72.05
PF resin/Zn coatings (mean diameter size of particles 0.1 – 5 $\mu\text{m}$ )	- 1.53	32.52	38.02	33.77	238.75	15.34
PF resin/Zn coatings (mean diameter size of particles 6 – 10 $\mu\text{m}$ )	- 1.51	21.44	20.98	79.60	336.32	10.11

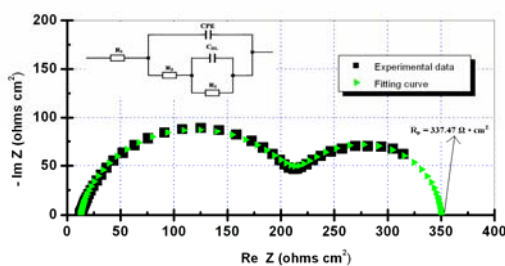
Two equivalent electrical circuits were proposed to account for the experimental impedance spectra. Those circuits allow obtaining an excellent agreement between experimental and simulated impedance plots.



( a )



( b )



( c )

**Fig. 9.** Nyquist plot of impedance spectrum of experimental data and fitting curve for: (a) pure zinc coatings; (b) Zn/PF resin coatings (0.1 – 5.0  $\mu\text{m}$ ); (c) Zn/PF resin coatings (6 – 10  $\mu\text{m}$ ) in 0.5M NaCl solution after 30 min of immersion

The fitting values confirmed that the incorporation of polymer particles enhances the corrosion resistance of composite coating samples. The polarization resistance obtained from fitting curve indicates a small value for pure zinc coating ( $32.20 \Omega\cdot\text{cm}^2$ ) versus polarization resistance of composite coatings ( $232.17 \Omega\cdot\text{cm}^2$ , respectively  $337.47 \Omega\cdot\text{cm}^2$ ).

It was observed that a good polarization resistance has PF resin/Zn composite coatings with mean diameter size of polymer particles 6 – 10  $\mu\text{m}$ ; the value of polarization resistance for this type of coatings is about ten times bigger than the polarization resistance of pure zinc coatings.

Electrochemical measurements concluded that by adding PF resin particles in zinc electrolyte solution from electrodeposition it was obtained PF resin/Zn coatings more resistant to corrosive attack in 0.5M NaCl solution than pure zinc obtained by electrodeposition using the same parameters.

## 4. Conclusions

PF resin/Zn coatings was successfully deposited from solution containing 10 g/L PF resin particles with mean diameter size of particles 0.1 – 5.0  $\mu\text{m}$  and 6.0 – 10.0  $\mu\text{m}$ .

The coatings thickness for composite coatings is less than the thickness of pure zinc coatings because the resin particles increase the uniformity of the layers and decrease the grain size of zinc crystals.

PF resin particles affect the electrodepositing process of zinc coatings by changing the morphology of the surfaces of composite coatings versus pure zinc obtained at the same electrodeposition parameters.

From electrochemical measurements it was observed that by adding PF resin particles in zinc electrolyte it was obtained PF resin/Zn coatings more resistant to corrosive attack in 0.5M NaCl solution than pure zinc coatings.



The results confirm that the disperse phase introduced in electrolyte bath has an obvious corrosion inhibition effect on the resulted composite surfaces.

## References

- [1]. H.Y. Li, J.Y. Duan, D.D. We - *Comparison on corrosion behaviour of arc sprayed and zinc-rich coatings*, Surface & Coatings Technology, 235, (2013), pp. 259 – 266.
- [2]. R. Asthana, A. Kumar, N. B. Dahotre, Materials Processing and Manufacturing Science, Edited by Butterworth-Heinemann, London, (2006).
- [3]. C. M. Praveen Kumar, T. V. Venkatesha, K.G. Chandrappa - *Effect of surfactants on co-deposition of B<sub>4</sub>C nanoparticles in Zn matrix by electrodeposition and its corrosion behavior*, Surface and Coatings Technology, 206, (2012), pp. 2249–2257.
- [4]. S. Ranganatha, T.V. Venkatesha, K. Vathsala, M.K. Punith Kumar - *Electrochemical studies on Zn/nano-CeO<sub>2</sub> electrodeposited composite coatings*, Surface and Coatings Technology, 208, (2012), pp. 64–72.
- [5]. H. B. Muralidhara, Y. Arthoba Nayaka, J. Balasubramanyam, K. Yogesh Kumar, H. Hanumanthappa, M.S. Veena - *Electrodeposition of Zn-Graphite nanoparticles composite and their characterization*, Journal of Chemical and Pharmaceutical Research, 4, (2012), pp. 440–449.
- [6]. T. Frade, V. Bouzon, A. Gomes, M. I. da Silva Pereira - *Pulsed-reverse current electrodeposition of Zn and Zn-TiO<sub>2</sub> nanocomposite films*, Surface and Coatings Technology, 204, (2010), pp. 3592–3598.
- [7]. B. M. Praveen, T. V. Venkatesha - *Electrodeposition and properties of Zn-nanosized TiO<sub>2</sub> composite coatings*, Applied Surface Science, 254, (2008), pp. 2418–2424.
- [8]. K. Vathsala, T. V. Venkatesha - *Zn-ZrO<sub>2</sub> nanocomposite coatings: Electrodeposition and evaluation of corrosion resistance*, Applied Surface Science, 257, (2011), pp. 8929–8936.
- [9]. O. Sancakoglu, O. Culha, M. Toparli, B. Agaday, E. Celik - *Co-deposited Zn-submicron sized Al<sub>2</sub>O<sub>3</sub> composite coatings: production, characterization and micromechanical properties*, Materials And Design, 32, (2011), pp. 4054–4061.
- [10]. S. Bindiya, S. Basavanna, Y. Arthoba Naik - *Electrodeposition and corrosion properties of Zn-V<sub>2</sub>O<sub>5</sub> composite coatings*, Journal of Materials Engineering and Performance, 21, (2012), pp. 1879–1884.
- [11]. M. Azizi, W. Schneider, W. Plieth - *Electrolytic co-deposition of silicate and mica particles with zinc*, Journal Solid State Electrochemistry, 9, (2005), pp. 429–437.
- [12]. D. Vasilakopoulos, M. Bouroushian - *Electrochemical codeposition of PMMA particles with zinc*, Surface and Coatings Technology, 205, (2010), pp. 110–117.
- [13]. O. Kammona, K. Kotti, C. Kiparissides, J. P. Celis - *Synthesis of polymeric and hybrid nanoparticles for electroplating applications*, Journal Electrochimica Acta, 54, (2009), pp. 2450–2457.
- [14]. D. Koleva, N. Boshkov, G. Raichevski, L. Veleva - *Electrochemical corrosion behaviour and surface morphology of electrodeposited zinc, zinc-cobalt and their composite coatings*, Transactions of the Institute of Metal Finishing, 83, (2005), pp. 188–193.
- [15]. L. Benea, M. Mardare-Prlea - *Electrodeposition of UHMWPE particles with cobalt for biomedical applications*, Digest Journal of Nanomaterials and Biostructures, 6, (2011), pp. 1025 – 1034.
- [16]. J. Morales, L. Sanchez, S. Bijani, L. Martinez, M. Gabas, J. R. Ramos-Barrado - *Electrodeposition of Cu<sub>2</sub>O: An excellent method for obtaining films of controlled morphology and good performance in Li-ion batteries*, Electrochemical and Solid State Letters, 8, (2005), pp. A159 – A162.
- [17]. V. Georgieva, M. Ristov - *Electrodeposited cuprous oxide on indium tin oxide for solar applications*, Solar Energy Materials and Solar Cells, 73, (2002), pp. 67–73.
- [18]. Z. Quan, S. Ohguchi, M. Kawase, H. Tanimura, N. Sonoyama - *Preparation of nanocrystalline LiMn<sub>2</sub>O thin film by electrodeposition method and its electrochemical performance for lithium battery*, Journal of Power Sources, 244, (2013), pp. 375–381.
- [19]. J. Xue, Q. Shen, W. Liang, X. Liu, L. Bian, B. Xu - *Preparation and formation mechanism of smooth and uniform Cu<sub>2</sub>O thin films by electrodeposition method*, Surface and Coatings Technology, 216, (2013), pp. 166–171.
- [20]. M. Stern, A. Geary - *Electrochemical polarization I. A theoretical analysis of the shape of polarization curves*, Journal Electrochemical Society, 104, (1957), pp. 56–63.



## MEASURES TO OPTIMIZE JOB SECURITY "CRANE MACHINISTS WHO TRANSPORT LIQUID STEEL"

**Viorel DRAGAN, Stefan DRAGOMIR, Marian BORDEI**

"Dunărea de Jos" University of Galați, 111, Domnească Street, 800201, Galați, Romania  
email: vdragan@ugal.ro

### ABSTRACT

*The starting point in optimizing the prevention of occupational accidents and occupational diseases for a crane machinist for the transport of liquid steel is the risk assessment of the system. Risk assessment involves the identification of all risk factors in the analyzed system and quantifies their size based on the combination of two parameters: the maximum possible consequence severity and frequency on the human body. These are partial risk levels for each risk factor respectively overall levels of risk for the entire analyzed system (job).*

*According to the European standard, in Romania, "the factors taken into consideration for the risk assessment" are: a) the probability of an injury or damage to health; b) the maximum expected severity of the lesion.*

KEYWORD: global risk level, risk factors, crane machinist

### 1. Introduction

The job risk for a crane machinist carrying liquid steel is represented by possible injuries and occupational diseases. Therefore, elements by means of which risk can be characterized can be determined by the probability that the action of a risk factor can lead to the consequence of the accident and severity of risk factors on the victim.

The crane machinist who transports liquid steel consist of provides power converters with hot metal and filler materials.

The equipment related to the analyzed job are [2]:

- crane 250/80 tf with electric drive;
- iron pots, slag;
- lime-containers (containers);
- cleaning pots anchor;
- mouth cleaner converter;
- spears desulphurisation plant;
- hot iron (temp. ~ 1300<sup>o</sup>C);
- slag (temp ~ 1100 - 1200<sup>o</sup>C).

The crane machinist works in the crane cab within the OLD 1 department.

We believe it is necessary to mention that there are exceedings o the allowed values for the following pollutants: total dust, CO, dust, noise.

The lighting level is reduced in some workstations and very high in the content viewing converter.

There are also noted: the presence of infrared radiation, the presence of air currents, toxic gases.

The cabin temperature is high because the air conditioning is partially effective.

### 2. Types of risks for the liquid steel crane machinist trade

The main risks [3] for the liquid steel crane machinist trade, established by the team of researchers can be found in the tasks performed by the worker as follows:

- he weighs and decides upon the empty and full pots weight performing all operations according to briefing;
- he swings pots coming unswung from Continuous Casting Slag sector in slag valves;
- he makes the transshipments of the steel filled pot from a transfercar to another in order to take the charge to the continuous casting section;
- he moves the full pot from the connverter to the secondary plant of the steel making;
- he provides moving pots to be demolished or demolished;



- he provides moving parts of machinery or subassembly when it is necessary their replacement by maintenance workers;

- he provides moving iron pots to demolish masonry, tipping and their transportation to the warehouse building pots;

- he provides transporting ladles and empty pots already mounted from the tipper to the hydraulic bench, then deposits them on the transfercar;

- he ensures unloading of materials needed in the production process;

- he swings filled pots from one another or to cast iron pot for recovery.

## **2.1. Research regarding the identification of risk factors specific to crane machinist trade**

### **2.1.1. Mechanical risk factors:**

The main mechanical risk factors are:

- flow of material in liquid form;
- auto transport and trucks hitting while moving inside the plant site;

- automatic clamping of pots mechanisms;

- slip of pieces, materials, stored without stability;

- roll of pieces, materials stored without stability;

- surprised by charge machine;

- flip of pieces, parts, materials stored without stability;

- free fall of pieces, tools, materials at higher rates;

- leak-free liquid material to accidental crack pot;

- accidental discharge of liquid in places other than those provided by technology;

- sparking of particles – sparks, incandescent slag particles etc.;

- deviation from the normal trajectory ladles;

- erratic ladle balance;

- jet, rash - incandescent material at piercing or cause of water, or some impurities;

- contact with dangerous surfaces or contours (pungent, sharp, slippery);

- work in the vicinity of pressure vessels - oxygen cylinders, plumbing, process steam plants;

- vibration of the cabin because of the tread.

### **2.1.2. Heat risk factors:**

The main heat risk factors are:

- high temperature of objects or surfaces: liquid metal, liquid slag, overheated railings;

- accidental outbreaks, fire at the top of the pots and converters.

### **2.1.3. Electrical risk factors [4]:**

The main electrical risk factors are:

- electrocution by direct contact- electrical panels unensured in cabin, improvisations;

- electrocution by indirect contact - the accidental destruction of electrical protections;

- electrocution at step voltage - while walking inside (some leakage).

### **2.1.4. Chemical risk factors:**

The main chemical risk factors are:

- flammable substances - windows secured with wooden slats, flammable upholstery;

- explosives - explosives come accidentally in the convert as input material, alloying;

- gas fumes (determined as in attached bulletins) – CO;

- particles in the air - the phenomenon of dissociation.

### **2.1.5. Physical risk factors:**

The main physical risk factors are:

- high air temperature (above 40<sup>o</sup>C);

- low air temperature in cold weather to move out;

- airflow – natural draught or favoured by the hood operation;

- noise level higher than allowed;

- brightness - contrast between and melten metal in the furnace or pot and natural background;

- infrared radiation from incandescent material;

- natural disasters: earthquake;

- pneumoniconiosis dust present in workplace air.

### **2.1.6. Mental risk factors:**

The main mental risk factors are:

- intense work pace imposed by technology;

- difficult decisions to be made in short time - to solve situations of "incident" or "failure" type;

- repetitive operations of short cycle - repetitive cycles of about 15 minutes.

### **2.1.7. Risk factors due to wrongful workers:**

The main risk factors due to wrongful workers are:

- execution of contingency operations not stipulated in the norms or in other way than technical work stipulations;

- erroneous maneuver execution - driving in another direction, shifting another place, failure to avoid the projections of the path of travel of the pot etc.;

- wrong positioning of pots in relation to inverters, berths filling or discharge technological alternative to the inverter tipping etc before starting development;
- setting pots on hooks without proper engagement tilting mechanisms;
- trouble with the operator of the mixer, of the converter, etc. or when working in tandem;
- turning on machinery without confirming safety functions;
- moving and standing in dangerous areas - the car doorways and/or CF;
- fall on the same level by imbalance, slipping, tripping;
- falls from height by stepping into the void, imbalance, slip.

### 3. Analysis, measurement and representation of risk factors

Following research on targeting risks factors, we have drawn a diagram in Figure 1, in which, 53 risk factors are represented on Ox-axis (F1 to F53) and on Y-axis the partial risk levels for each risk factor are mentioned, as follows:

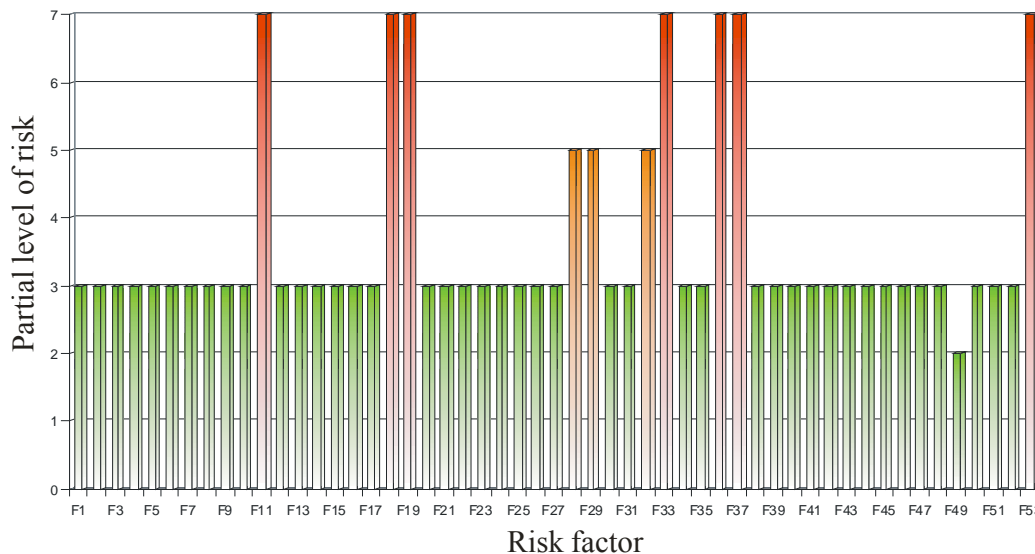


**Fig. 1.** Representation of risk factors [2]

- F1-A liquid material flow.
- F2-Flick of the auto transport and / or car to move through the site batch plant and machinery, forklifts.
- F3-Automatic clamping mechanisms pots.
- F4-Sliding parts, materials, stored without stability.
- F5-Roll of the pieces of stored materials without stability.
- F6-Rolling on wheels: surprise by its charge.
- F7-Flip pieces, parts, materials stored without stability.
- F8-Free Fall parts, tools, materials at higher rates.

#### **Maximum risk factors are:**

- F11 (design of particles - sparks, shrapnel, etc. incandescent slag particles);
- F18 (high temperature of objects or surfaces: liquid metal, liquid slag, oderheated railings);
- F19 (outbreaks of accidental fire at the top of the pots and converters)
- F33 (gases, vapors of CO);
- F36 (technologic process which does not provide a working environment in accordance with the applicable law);
- F37 (exceeding the permissible nominal mass of tasks - 260tf to 250tf admitted);
- F53 (failure to use protective equipment and other work protectors provided by the employer).

#### **In the category of high risk factors we include:**

- F28 (exceeded noise level);
- F29 (brightness - contrast between the melten metal in the furnace or pot and natural background);
- F32 (pneumoniconiosis powder present in workplace air) and others falling within the category of medium environmental risk factors.

- F9-Free drain pan accidentally cracking into the crane cab.
- F10-Accidental discharge of liquid in places other than those provided by technology.
- F11-Design of particles - sparks, shrapnel, etc. incandescent slag particles.
- F12-Deviation from the normal trajectory ladles.
- F13-Uncontrolled balance the load (the ladle).
- F14-Jet eruption - incandescent material or cause puncture water, or some impurities.



F15-Contact surfaces or contours dangerous (stinging, sharp, slippery).  
F16-Working in the vicinity of pressure vessels - oxygen cylinders, plumbing, process steam plants.  
F17-Vibration of the cabin because of the tread.  
F18-The high temperature of objects or surfaces: liquid metal, liquid slag, overheated railings.  
F19-Outbreaks of accidental fire at the top of the pots and converters.  
F20-Electrocution by direct - electrical panels with unensured cabin improvisations.  
F21-Shock by indirect contact - the accidental destruction of electrical protections.  
F22-The emergence of electric voltage step - the displacement site (some leakage).  
F23-Flammable - windows secured with wooden slats, flammable upholstery.  
F24-Explosives - enough explosives accidentally convert the input material, alloying.  
F25-High temperature (over 40<sup>o</sup>C).  
F26-Low temperature in cold weather to move out.  
F27-Airflow - chimney hoods or favored by the operation.  
F28-Noise level measurements according to the ballot attached.  
F29-Brightness - contrast between the furnace and the molten metal pot and natural background.  
F30-Infrared radiation from incandescent material.  
F31-Natural disasters: earthquake.  
F32-Pneumoniconiosis dust present in workplace air (according to the attached ballot determinations).  
F33-Gas fumes (according to the attached determinations bulletins) - CO.  
F34-Carcinogens present in workplace air (according to the ballot determinations attached)  
F35-Particulate matter in the air - the phenomenon of dissociation.  
F36-Technological process which provides a working environment in accordance with the applicable law.  
F37-Exceeding the permissible nominal mass of tasks 260tf to 250tf admitted.  
F38-Static effort - mostly sitting working position.  
F39-High rate of work imposed by technology.  
F40-Difficult decisions in a short time - to address situations of "incident" or "failure".  
F41-Short cycle repetitive operations - repetitive cycles of approx. 15 minutes.  
F42-Execution of contingency operations in work load or in other way than technical provisions work.  
F43-Erroneous execution maneuver - driving in another sense, shifting to another place, failure to avoid the projections of the path of travel of the pot etc.  
F44-Wrong positioning of pots in relation to inverters, berths filling or discharge technological alternative to the inverter tipping etc before starting development.

F45-Setting pots on hooks without proper engagement tilting mechanisms.  
F46-Trouble with the operator of the mixer, of the converter, etc. or when working in tandem.  
F47-Turning machinery without confirming safety functions.  
F48-Travel, station in hazardous areas - the car doorways and / or CF.  
F49-Fall on the same level by imbalance, slipping, tripping.  
F50-Fall from height by stepping into the void, imbalance, slip.  
F51-Communication accidentogene - signaling non-procedural language - no radio station.  
F52-The omission of its own security operations.  
F53-Failure to use protective equipment and work and other protectors provided by the employer.

#### 4. Calculating the overall risk of the trade crane machinist trade LS

With the scale of assigning risk levels, risk levels are determined for each risk factor separately. This yields a hierarchy of risks in the workplace dimension, which enables the prioritization of prevention and protection methods, depending on the risk factor with the highest level of risk.

Overall risk level (Nr) on the job is calculated as a average of the risk levels established for the identified risk factors.

For the result to reflect the reality as accurately as possible, it is used as a weighting element the rank of the risk factor, which is equal to the level of risk.

In this way, the factor with the highest level of risk will have the highest rank, too.

This eliminates the possibility that the effect of compensation between extremes, for is involved by any statistics average to mask the presence of the factor with the highest level of risk.

The formula for calculating the overall risk level is:

$$Nr = \frac{\sum_{i=1}^n r_i \cdot R_i}{\sum_{i=1}^n r_i} \quad (1)$$

where:

$r_i$  = rank risk factor "i";

$R_i$  = the level of risk for the risk factor "i";

$n$  = number of risk factors identified in the workplace.

Overall risk level calculated for *crane machinist LS* is equal to 4.17, a value that falls into the category of jobs with unacceptable level of risk.

This result is supported by the corresponding assessment *sheet diagram* of Figure 1, from which it



appears that of the total of 53 risk factors identified, only 10 exceed the critical value calculated.

## 5. Conclusions

To reduce or eliminate the 10 risk factors presented in section 3, in order to optimize job security for "crane machinists who transport liquid steel", the following measures are necessary:

### *Technical measures:*

- warning flags to mark all areas with contact danger with high temperature surfaces;
- restriction on possible areas where there is a possibility of contact with surfaces that have high temperature;
- design and development of optical systems and audible warning for the presence of toxic gases;
- placement of gas detectors in areas likely to accumulate toxic gases or toxic fumes;
- providing the performer with all the equipment required to report toxic gases and vapors;
- measures to combat noise at source - this can be achieved through designing changes to the technical equipment, if possible, or by adopting special attenuating devices;
- measures to combat noise at receiver - consisting in isolating the staff working in a noisy setting work area, taking into account the possibility of accidental, flames in the vicinity or at the point of intervention;
- marking the hazardous flame occurring area;
- strict compliance with the technical stipulations relating to the how to behave and to the moments of interventions license;
- making clear procedures on how to act in case of toxic gases and vapors issue alert;
- introduction in the job sheet of working band leaders of the provision of immediate withdrawal from work for employees not wearing full protective

equipment, suitable for risk area and activity;

- regular exercise enforcement action in case of gas danger;
  - inventory and withdrawal from the use of not approved equipment;
  - workplaces where the daily personal exposure to noise above 85 dB (A) or where the maximum value of the unweighted instantaneous sound pressure exceeds 200P must be marked accordingly.
- ### *Organisational measures:*
- training on the risk of contact, even accidental, with high temperature surfaces;
  - use of fire protection equipment resistant to high temperatures;
  - training workers about the risks of travel, stationary cabin near the inverter, holding furnace, etc. 260tf to 250tf admitted
  - training employees on the consequences of failing to obey security restrictions - not using or incomplete use of means of protection etc. 260tf to 250tf admitted
  - permanent check up by the leading head or/and at random by the superiors if the standards regarding labour security techniques are respected in the considered area.

## References

- [1]. \*\*\* - Instrucțiunea de lucru la oțelărie "I.P.R. – U.O.R. – O-004/2006, rev. 0";
- [2]. \*\*\* - Instrucțiunea de lucru cu podul rulant de la oțelarie "I.P.R. – UOR -104/2009, rev.1";
- [3]. \*\*\* - Instrucțiunea tehnică de lucru privind exploatarea și întreținerea sistemelor de protecție și siguranță ale podurilor rulante „I.P.R. – U.O.R. – 014/2009, rev. 1”;
- [4]. \*\*\* - Instrucțiunea tehnică de lucru privind efectuarea activității de curatenie la oțelărie „I.O.R.– 083/2009, rev. 2”.
- [5]. \*\*\* - Cartea lucratorului la oțelarie - Ed. Interna .U.O.R. Rev. 2012.
- [6]. \*\*\* - Colectia de standarde EN292-1/1991, EN 1050/96, SR EN292/1-1996.

MANUSCRISELE, CĂRȚILE ȘI REVISTELE PENTRU SCHIMB, PRECUM ȘI ORICE  
CORESPONDENȚE SE VOR TRIMITE PE ADRESA:

MANUSCRIPTS, REVIEWS AND BOOKS FOR EXCHANGE COOPERATION, AS WELL  
AS ANY CORRESPONDANCE WILL BE MAILED TO:

LES MANUSCRIPTS, LES REVUES ET LES LIVRES POUR L'ECHANGE, TOUT AUSSI  
QUE LA CORRESPONDANCE SERONT ENVOYES A L'ADRESSE:

MANUSKRIPTEN, ZIETSCHRIFTEN UND BUCHER FUR AUSTAUCH SOWIE DIE  
KORRESPONDENZ SIND AN FOLGENDE ANSCHRIFT ZU SEDEN:

After the latest evaluation of the journals achieved by National Center for the Science and  
Scientometry Politics (CENAPOSS), as recognition of its quality and impact at national level,  
the journal is included in B<sup>+</sup> category, 215 code ([http://www.cncsis.ro/2006\\_evaluare\\_rev.php](http://www.cncsis.ro/2006_evaluare_rev.php)).

The journal is indexed in:

CSA: [http://www.csa.com/ids70/serials\\_source\\_list.php?db=mehctrans-set-c](http://www.csa.com/ids70/serials_source_list.php?db=mehctrans-set-c)

EBSCO: <http://www.ebscohost.com/titleLists/a9h-journals.pdf>

Copernicus: <http://journals.indexcopernicus.com/karta.php>

The papers published in this journal can be visualized on the "Dunarea de Jos" University  
of Galati site, the Faculty of Materials and Environmental Engineering, page: [www.fimm.ugal.ro](http://www.fimm.ugal.ro).

**Publisher's Name and Address:**

Contact person: Antoaneta CĂPRARU  
Galati University Press - GUP  
47 Domneasca St., 800008 - Galati, Romania  
Phone:+40 336 130139, Fax: +40 236 461353  
Email: [gup@ugal.ro](mailto:gup@ugal.ro)

**Editor's Name and Address:**

Prof. Dr. Eng. Marian BORDEI  
Dunarea de Jos University of Galati, Faculty of Materials and Environmental Engineering  
111 Domneasca St., 800201 - Galati, Romania  
Phone: +40 336 130223, Phone/Fax: +40 236 460750  
Email: [mbordei@ugal.ro](mailto:mbordei@ugal.ro)

***AFFILIATED WITH:***

- ***ROMANIAN SOCIETY FOR METALLURGY***
- ***ROMANIAN SOCIETY FOR CHEMISTRY***
- ***ROMANIAN SOCIETY FOR BIOMATERIALS***
- ***ROMANIAN TECHNICAL FOUNDRY SOCIETY***
- ***THE MATERIALS INFORMATION SOCIETY***  
***(ASM INTERNATIONAL)***

**Annual subscription (4 issues per year)**

**Edited under the care of  
Faculty of  
MATERIALS AND ENVIRONMENTAL  
ENGINEERING**

Edited date: 30.09.2013

Issues number: 200

Printed by

Galati University Press

accredited CNCSIS

47, Domnească Street, 800036

Galati, Romania